Theoretical Analysis and Modeling of Molecular Spectroscopy on Oxygen Molecule and One-Dimensional Lanthanide-Cyclooctatetraene Clusters

---

2004

Ryuta TAKEGAMI

ACKNOWLEDGEMENT

The present thesis is a collection of the author's studies in the Professor Yabushita group, School of Fundamental Science and Technology, Graduate School of Science and Technology, Keio University.

The author would like to express his best gratitude to Prof. Satoshi Yabushita for his kind guidance, and continuing support during the research activities.

The author wishes to express his sincere acknowledgement to Prof. Atsushi Nakajima, Associate Prof. Naoki Yoshioka, Associate Prof. Hideto Kanamori, Dr. Michihiko Sugawara, Mr. Kaito Takahashi, Mr. Jun-ichi Suzumura and Mr. Natsuki Hosoya for their useful discussions and suggestions.

The author is also obliged to the members of the Yabushita Laboratory and the Nakajima Laboratory for their kindness and cooperation.

The studies described in Chapters 3 and 4 are the result of daily co-operation with the Nakajima Laboratory. The author would like to thank Prof. Nakajima, Mr. Suzumura, and Mr. Hosoya again. Lastly, the author expresses his gratitude to family and friends for hearty encouragement.

Ryuta TAKEGAMI

Keio University, Yokohama

February 14, 2005

CONTENTS

Chapter 1.

General Introduction

1.1. What is 'Theoretical Chemistry' ?

P. A. M. Dirac, one of the persons who developed the quantum mechanics, said in 1929 that 'The underlying physical laws necessary for the mathematical theory of a large part of physics and the whole of chemistry are thus completely known, and the difficulty is only that the exact application of these laws leads to equations much too complicated to be soluble. It therefore becomes desirable that approximate practical methods of applying quantum mechanics should be developed, which can lead to an explanation of the main features of complex atomic systems, without too much computation.' [1.1] Following one century of selfless efforts by many theoreticians and dramatic progress of computers, we have developed the versatile computation system, which allows us the ubiquitous application of 'theoretical chemistry' to various fields of science. [1.2-4]

Undoubtedly, present high performance computers can give calculation results easily and fastly, which contribute largely to theoretical chemistry, however the aim of theoretical chemistry is not limited to produce the numerical data. If theoreticians do not reply to questions such as 'What happened?' or 'How should we understand the origin or

mechanism?', they have no future as fundamental scientists. The most advantage of theoretical chemistry is that it is able to give the direct answer to the above questions, because theoreticians have the wave functions themselves which can describe all of the chemical and physical properties from the first principle. Thus, we have to present proper interpretations and precise predictions for chemical phenomena.

In such a situation, theoreticians must pay a careful attention to 'technical terms' in explanations. Present scientific realm includes a wide range of specialized fields, and the exchanges of opinions among the various fields are becoming increasingly difficult due to complicated technical terms of each specialized field. Part of these complications is essentially inevitable, because various aspect of nature cannot be explained by only one specialized term. However, some of them are senseless problems which result from lack of the communication among the different fields. We should be ashamed of our poor communication skills, because the fundamental scientists should have public accountability. Especially, theoretical chemistry must retain the accountability as mentioned above. In addition, present science field tends to emphasize immediate application to be more important, so that if theoreticians ignore the accountability, we will lose the raison d'etre in science. Therefore, we ought to provide interdisciplinary explanations which eliminate barriers between experimentalists and theoreticians, or among the specialized fields in molecular science.

In this thesis, the author will give theoretical approach to molecular spectroscopy which plays an important role in physical chemistry. In doing so, the author takes a special care of the above mentioned problems and aims to provide necessary and sufficient explanations and models for experimental spectroscopy. Before describing concrete subjects of this thesis, the author will introduce basic theories in Section 1.2 to explain the objects and results of the research.

1.2. Basic Theory of Spectroscopy

One of the viewpoints for understanding molecular chemistry is to focus attention on the motion of electrons in molecules. In principle, the motion of electrons can be described by the wave functions derived from Schrödinger or Dirac equation, and the basic idea supports 'electronic structure theory' which plays one important part in modern theoretical chemistry. [1.5-8] On the other hand, molecular spectroscopy observes some kind of projections of the motion of electrons by absorption or emission of light by molecules. [1.9]

Applying Fermi's golden rule to the interaction between a molecule and light, we can write down the absorption or emission intensity from the state *a* to *b* as the following simple equation. [1.8]

$$I_{ab} \propto \delta\left(E_a - E_b \pm \hbar\omega\right)\left|\left\langle \Psi_a \left| \boldsymbol{\mu} \right| \Psi_b \right\rangle\right|^2, \qquad (1\text{-}1)$$

where E_a and E_b are the energy levels of the states *a* and *b*, and $\left|\Psi_a\right\rangle$ and $\left|\Psi_b\right\rangle$ are the total wave functions of the states *a* and *b*, $\boldsymbol{\mu}$ is electric-dipole moment operator. $\left\langle \Psi_a \left| \boldsymbol{\mu} \right| \Psi_b \right\rangle$ is called as the transition dipole moment vector. The above equation represents that only transitions which obey the energy conservation, $\left|E_a - E_b\right| = \hbar\omega$, can occur and the probability is proportional to the square of the transition dipole moment vector. Therefore, one way of theoretical approaches to the molecular spectroscopy is to focus on the energy difference $E_a - E_b$ and the transition dipole moment vector $\left\langle \Psi_a \left| \boldsymbol{\mu} \right| \Psi_b \right\rangle$ between the initial and final state.

For the concrete subject of the theoretical studies on the molecular spectroscopy, the author had chosen electron spectra for the Herzberg I band of oxygen molecule and photoelectron spectra of one-dimensional lanthanide-cyclooctatetraene clusters. In the former theme, the

author analyzed the absorption intensities, particularly the transition dipole moment which is the second term in Eq. (1-1). In the latter theme, he has calculated the electron detachment energies and ionization energies of clusters, for which the first term in Eq. (1-1) becomes important. In the following section, he will give simple reviews for the first and second terms of Eq. (1-1) from the theoretical viewpoint.

1.2.1. Transition Dipole Moment

If we fix an electric field irradiated to molecules in the *Z* direction of the laboratory-fixed coordinate, we can consider only the *Z* component of the transition dipole moment vector. Absorption or emission rate of plane polarized light with the electric vector of the light in the *Z* direction is proportional to the squared value of the *Z* component of the transition dipole moment as follows. [1.8,10,11]

$$M(a,b) = \left\langle \Psi_a \middle| \mu_Z \middle| \Psi_b \right\rangle . \qquad (1\text{-}2)$$

If $M(a,b) \neq 0$, we call the transition between the state *a* to *b* as 'allowed', otherwise, we call the transition as 'forbidden'.

One of the most important approximations made in the electronic structure theory is the separation of the total wave function into independent electronic and nuclear factors. [1.8,10] Furthermore, the nuclear term can usually be approximated by a product of rotational and vibrational wave functions. [1.8,10] Thus, the total wave function is represented by

$$\left| \Psi_i \right\rangle = \left| e_i \right\rangle \left| v_i \right\rangle \left| r_i \right\rangle . \qquad (1\text{-}3)$$

Here, *e*, *v* and *r* express the electronic, vibrational, and rotational states, respectively. In Eq. (1-3), each wave function is naturally defined in the molecular coordinate system (*x*, *y*, *z*). Therefore, to evaluate the transition dipole moment of Eq. (1-2), μ_Z must also be rewritten in

the molecular coordinate system. From classical mechanics, we know that μ_Z in the laboratory fixed system can be transformed to $\mu_{x,y,z}$ in the molecular fixed coordinate by the following direction cosine matrix $\phi(\phi,\theta,\gamma)$ relating unit vectors in the two systems in terms of the Euler angles ϕ,θ, and γ. [1.12]

$$\mu_Z = \sum_{n=x,y,z} \phi_{Zn}(\phi,\theta,\gamma)\mu_n \ . \qquad (1\text{-}4)$$

Using the above relation for Eq. (1-2), the transition dipole moment can be written as follows.

$$M(a,b) = \sum_{n=x,y,z} \langle e_a | \langle v_a | \langle r_a | \phi_{Zn}(\phi,\theta,\gamma)\mu_n | e_b \rangle | v_b \rangle | r_b \rangle . \qquad (1\text{-}5)$$

The operator ϕ_{Zn} only operates on the rotational wave function, and μ_n operates only on the electronic and vibrational wave functions. Thus, Eq. (1-5) is reduced as follows.

$$M(a,b) = \sum_{n=x,y,z} \langle e_a | \langle v_a | \mu_n | e_b \rangle | v_b \rangle \langle r_a | \phi_{Zn}(\phi,\theta,\gamma) | r_b \rangle . \qquad (1\text{-}6)$$

The matrix elements of the rotational wave function are tabulated conveniently in general text book. [1.12] Now, we come to the matrix elements of the electronic and vibrational wave functions.

If the matrix element of the dipole moment operator with the electronic wave function is not significantly affected by changes in the internuclear separation during vibration, the matrix elements of the electronic and vibrational wave functions can be rewritten (Condon approximation) as follows. [1.8,10]

$$\langle e_a | \langle v_a | \mu_n | e_b \rangle | v_b \rangle = \langle v_a | v_b \rangle \langle e_a | \mu_n | e_b \rangle_{\mathbf{R}_e} , \qquad (1\text{-}7)$$

where $\langle v_a | v_b \rangle$ and $\langle e_a | \mu_n | e_b \rangle_{\mathbf{R}_e}$ are called as the Franck-Condon factor and *n* component of the electronic transition moment vector at the equilibrium nuclear coordinate $\mathbf{R}_e$, and depend only on the vibrational and electronic wave functions, respectively.

The Franck-Condon factor $\langle v_a | v_b \rangle$ expresses the overlap integral between the two

vibrational states in their respective electronic states. The transition dipole moment is therefore largest between vibrational states that have the greatest overlap. Unless the two molecular potential curves are perfect replications of one another, any vibrational state has a nonzero value of $\langle v_a | v_b \rangle$. Indeed, it is generally the case that several vibrational states have similar values of $\langle v_a | v_b \rangle$, and so transitions occur to all of them. Thus, a progression of transitions is stimulated and a series of lines are observed in the electronic spectrum. [1.8]

Next, we consider the second factor $\langle e_a | \mu_n | e_b \rangle_{\mathbf{R}_e}$ in Eq. (1-7). Since the electric-dipole moment operator is a one-electron operator, to the first approximation, one electron transitions from the initial wave function $|e_a\rangle$ to the final wave function $|e_b\rangle$ is only allowed.

In evaluating $\langle e_a | \mu_n | e_b \rangle_{\mathbf{R}_e}$ for molecules, the group theory plays an important role. [1.8] In the theory, firstly, we classify electronic states of the molecule by the irreducible representation of the point group to which the molecule belongs, and derive the 'selection rule' for the electronic transition moment. Hereafter, the author summarizes the selection rule for the electronic transition moment of homonuclear diatomic molecules. [1.8-10]

Generally, the electronic and rotational wave functions of diatomic molecules are expressed by basis functions characterized by Hund's coupling schemes. [1.8-10] We firstly discuss the selection rules that hold quite generally, independent of the coupling scheme to which the electronic state under consideration belongs, then discuss selection rules for Hund's case (a).

General selection rules [1.8-10]

The selection rule for the quantum number *J* of the total angular momentum is

$$\Delta J = 0, \pm 1, \quad \text{with the restriction} \quad J = 0 \not\rightarrow J = 0 . \tag{1-8}$$

Moreover, the selection rules about the + and − symmetry of the total wave function and the *s*

and *a* symmetry of identical nuclei hold quite generally as follows.

$$\begin{array}{l} + \leftrightarrow -, + \not\leftrightarrow +, - \not\leftrightarrow - \\ s \leftrightarrow s, a \leftrightarrow a, s \not\leftrightarrow a \end{array} . \qquad (1\text{-}9)$$

Finally, we have the selection rule for the *g* and *u* symmetry of electronic states as follows.

$$g \leftrightarrow u, g \not\leftrightarrow g, u \not\leftrightarrow u . \qquad (1\text{-}10)$$

These rules always hold rigorously for electric dipole transition of homonuclear diatomic molecules.

Selection rules holding for Hund's case (a) [1.8-10]

The basis function of Hund's case (a) is characterized by the total angular momentum (J), the total spin angular momentum of electrons (S), the z component of the total orbital angular momentum of electrons (Λ), the z component of S (Σ), and the z component of the total angular momentum (Ω), which is related by $\Omega=\Lambda+\Sigma$. Apart from the preceding general selection rules, there are some selection rules which hold in Hund's case (a).

$$\begin{array}{ll} \Delta\Lambda = 0, \pm 1 & \Delta\Omega = 0, \pm 1 \\ \Delta S = 0, & \Delta\Sigma = 0 \end{array} . \qquad (1\text{-}8)$$

Furthermore, the selection rule for the symmetry of the $\Lambda=0$ (Σ) state is written as follows.

$$\Sigma^{\pm} \leftrightarrow \Sigma^{\pm}, \Sigma^{\pm} \not\leftrightarrow \Sigma^{\mp} . \qquad (1\text{-}9)$$

All these rules are established by a detailed consideration of the symmetry properties of the transition dipole moment with the Hund's case (a) basis function. [1.9,10] As mentioned above, these selection rules hold only between the Hund'case (a) bases. In fact, owing to some perturbations, these selection rules break down, and we can observe 'forbidden transition'. [1.8,9]

For example, considering the **spin-orbit** or **L-uncoupling** interaction (as described in the following section), we can observe the $\Sigma^{+} \leftrightarrow \Sigma^{-}$ electronic transition which is forbidden in

the Hund's case (a) bases. In Section 1.3.1 and Chapter 2, the author will discuss theoretically this $\Sigma^+ \leftrightarrow \Sigma^-$ transition of oxygen molecule.

1.2.2. Perturbations of Diatomic Molecules

In the following section, the author summarizes the spin-orbit (SO) and L-uncoupling (RO) interactions as examples of perturbations of diatomic molecules.

Spin-Orbit Interaction [1.8,10,13]

We now turn to the interaction energy between an internal magnetic field and a magnetic moment of an electron. The classical calculation of the interaction energy runs as follows. An electron moving at a velocity **v** in an electric field **E** experiences a magnetic field,

$$\mathbf{B} = \frac{\mathbf{E} \times \mathbf{v}}{c^2}. \qquad (1\text{-}10)$$

where c is the speed of light. The electric field due to an isotropic electric potential ϕ is

$$\mathbf{E} = -\frac{\mathbf{r}}{r}\frac{d\phi}{dr}. \qquad (1\text{-}11)$$

It follows that

$$\mathbf{B} = -\frac{1}{rc^2}\frac{d\phi}{dr}\mathbf{r} \times \mathbf{v}. \qquad (1\text{-}12)$$

The orbital angular momentum of the electron is $\mathbf{l} = \mathbf{r} \times \mathbf{p} = m_e \mathbf{r} \times \mathbf{v}$, and so

$$\mathbf{B} = -\frac{1}{m_e rc^2}\frac{d\phi}{dr}\mathbf{l}. \qquad (1\text{-}13)$$

An electron has a magnetic moment $\boldsymbol{\mu}$ due to the spin angular momentum,

$$\boldsymbol{\mu} = -\frac{g_e e}{2m_e}\mathbf{s} \qquad (g_e = 2.002319314). \qquad (1\text{-}14)$$

The interaction energy between a field **B** and a magnetic moment $\boldsymbol{\mu}$ is $-\boldsymbol{\mu} \cdot \mathbf{B}$, so we can

anticipate that the spin-orbit interaction hamilitonian should be

$$H_{so} = -\boldsymbol{\mu}\cdot\mathbf{B} = \frac{1}{m_e r c^2}\frac{d\phi}{dr}\boldsymbol{\mu}\cdot\mathbf{l} = -\frac{g_e e}{2m_e{}^2 c^2 r}\frac{d\phi}{dr}\mathbf{s}\cdot\mathbf{l} \cong -\frac{e}{m_e{}^2 c^2 r}\frac{d\phi}{dr}\mathbf{l}\cdot\mathbf{s}. \qquad (1\text{-}15)$$

It turns out that this is exactly twice the result obtained by solving the Dirac equation. The error comes from the implicit assumption that one can step from the stationary nucleus to the moving electron without treating the change of viewpoint relativistically. The correct calculation gives as follows,

$$H_{so} = -\frac{e}{2m_e{}^2 c^2 r}\frac{d\phi}{dr}\mathbf{l}\cdot\mathbf{s} = \xi(r)\mathbf{l}\cdot\mathbf{s}. \qquad (1\text{-}16)$$

In this thesis, the author expresses the SO interaction for diatomic molecules as the following one-electron operator.

$$\begin{aligned} H_{so} &= \sum_i a_i \mathbf{l}(i)\cdot\mathbf{s}(i) \\ a_i\mathbf{l}(i) &= \sum_K \frac{\alpha^2}{2}\frac{Z_{\mathrm{eff},K}}{r_{iK}{}^3}\mathbf{l}_{iK} \end{aligned} \qquad (1\text{-}17)$$

where α is the fine-structure constant, $\alpha = e^2/\hbar c$, $\hat{\mathbf{l}}_{iK}$ is the orbital angular momentum of electron *i* about nucleus *K*, $Z_{\mathrm{eff},K}$ is the effective charge of the *K* th nucleus.

The selection rules for matrix elements of H_{so} are summarized as follows. [1.10]

$$\begin{aligned} &\Delta J = 0 \quad \Delta\Omega = 0 \quad g \not\leftrightarrow u \quad \Sigma^+ \not\leftrightarrow \Sigma^- \\ &\Delta S = 0 \quad \text{or} \quad \Delta S = \pm 1 \\ &\Delta\Lambda = \Delta\Sigma = 0 \quad \text{or} \quad \Delta\Lambda = -\Delta\Sigma = \pm 1 \end{aligned} \qquad (1\text{-}18)$$

In the single-configuration limit, if the two interacting states belong to the same configuration, then $\Delta\Lambda=\Delta\Sigma=0$ or, if the two states differ by at most one spin-orbital, then $\Delta\Lambda=-\Delta\Sigma=\pm 1$.

L-uncoupling [1.10-12]

Due to the large mass ratio, the motion of nuclei is much slower than that of electron. This allows us to say that the nuclei are nearly fixed with respect to electron motion. However, in

fact, two motions weekly couple each other. Especially, coupling between the nuclear rotation and the electron motion is called as rotation perturbations. Rotation perturbation is essentially identical to the Coriolis force, which is a fictitious force owing to the transformation between the space-fixed and the molecular-fixed coordinate.

An energy expression for the nuclear rotation is written as,

$$H_{ROT} = \frac{1}{2\mu R^2}\mathbf{R}^2 = \frac{1}{2\mu R^2}\left(\mathbf{R}_x^2 + \mathbf{R}_y^2\right), \qquad (1\text{-}19)$$

where **R** is the nuclear rotation angular momentum operator. The nuclear motion is necessarily in a plane that contains the internuclear axis: thus $\mathbf{R}_z$=0.

The total angular momentum (exclusive nuclear spin angular momentum), **J**, is defined also by the total electronic orbital and spin angular momentum, $\vec{\mathbf{L}}$ and $\vec{\mathbf{S}}$,

$$\vec{\mathbf{J}} \equiv \vec{\mathbf{R}} + \vec{\mathbf{L}} + \vec{\mathbf{S}} \qquad (1\text{-}20)$$

and this definition can be used to reexpress H_{ROT} in a convenient form,

$$\begin{aligned} H_{ROT} &= \frac{1}{2\mu R^2}\left[\left(\mathbf{J}_x - \mathbf{L}_x - \mathbf{S}_x\right)^2 + \left(\mathbf{J}_y - \mathbf{L}_y - \mathbf{S}_y\right)^2\right] \\ &= \frac{1}{2\mu R^2}\left[\left(\mathbf{J}^2 - \mathbf{J}_z^2\right) + \left(\mathbf{L}^2 - \mathbf{L}_z^2\right) + \left(\mathbf{S}^2 - \mathbf{S}_z^2\right)\right. \\ &\quad \left. + \left(\mathbf{L}^+\mathbf{S}^- + \mathbf{L}^-\mathbf{S}^+\right) - \left(\mathbf{J}^+\mathbf{L}^- + \mathbf{J}^-\mathbf{L}^+\right) - \left(\mathbf{J}^+\mathbf{S}^- + \mathbf{J}^-\mathbf{S}^+\right)\right] \end{aligned}, \qquad (1\text{-}21)$$

where

$$\begin{aligned} \mathbf{J}^{\pm} &= \mathbf{J}_x \pm i\mathbf{J}_y \\ \mathbf{L}^{\pm} &= \mathbf{L}_x \pm i\mathbf{L}_y \\ \mathbf{S}^{\pm} &= \mathbf{S}_x \pm i\mathbf{S}_y \end{aligned}. \qquad (1\text{-}22)$$

The first three terms of H_{ROT} have diagonal matrix elements exclusively. This diagonal part of H_{ROT} is the rotational energy of the Hund's case (a) basis function. The final three terms of H_{ROT}, which couple the orbital, spin and total angular momenta, are responsible for

perturbations between different electronic states. The first term in the final three terms is called as spin-electronic perturbation, the second is L-uncoupling, and the last is S-uncoupling. In the following chapter, the author especially focuses on L-uncoupling.

The selection rule for the L-uncoupling operator is as follows. [1.10]

$$\begin{array}{ll} \Delta J = 0 & \Delta\Omega = \pm 1 \quad g \nleftrightarrow u \\ \Delta S = \Delta\Sigma = 0 & \Delta\Lambda = \pm 1 \end{array} . \qquad (1\text{-}23)$$

Note that the $\mathbf{J}^-$ operator in the molecular-fixed coordinate behaves as follows.

$$\mathbf{J}^- \left| J\Omega \right\rangle = \sqrt{J(J+1) - \Omega(\Omega+1)} \left| J\Omega + 1 \right\rangle . \qquad (1\text{-}24)$$

Therefore, $\mathbf{J}^-\mathbf{L}^+$ steps both Ω and Λ by ± 1, which gives the above anomalous selection rules.

1.2.3. Electron Detachment and Ionization Energy

Photoelectron spectroscopy observes kinetic energy of an ejected electron by Einstein's photoelectric effect. The difference between the photon energy, which is known, and the electron kinetic energy, which is measured, is equal to the energy holding the electron in a molecule. Usually, we call the energy holding the electron in anion molecules as electron detachment energy, and that in neutral molecules as ionization energy.

In electronic structure theory, we equate negative of the Hartree-Fock (HF) orbital energy with the electron detachment or ionization energy from that orbital. [1.5,6] This simple identification is the content of Koopmans' theorem. The HF orbital energy ε_a is written as follows,

$$\varepsilon_a = \left\langle \varphi_a \left| h + \sum_j \left(J_j - K_j \right) \right| \varphi_a \right\rangle . \qquad (1\text{-}25)$$

where $\left|\varphi_a\right\rangle$ is a spin orbital, J_j is the coulomb operator, and K_j is the exchange operator due to spin-orbital φ_j. Then, we divide Eq. (1-25) into the kinetic and potential energy parts as

follows.

$$\begin{aligned}\varepsilon_a &= \left\langle \varphi_a \middle| h + \sum_j (J_j - K_j) \middle| \varphi_a \right\rangle \\ &= \left\langle \varphi_a \middle| -\frac{1}{2}\Delta \middle| \varphi_a \right\rangle + \left\langle \varphi_a \middle| \sum_j (J_j - K_j) - \sum_\alpha \frac{Z_\alpha}{|\mathbf{r} - \mathbf{R}_\alpha|} \middle| \varphi_a \right\rangle \\ &= \langle T \rangle + \langle V \rangle\end{aligned} \tag{1-26}$$

The magnitude of each energy component depends on the molecular size, substituent, and solvent effects. If the kinetic energy part $\langle T \rangle$ does not depend on these effects, we can pay attention only to the potential energy part $\langle V \rangle$.

Ionic clusters may have strong intracluster electric field which depends on their size, structure and constituent atoms, so that the electric field would give characteristic influence on their $\langle V \rangle$ part. Particularly, if the ionic molecules have anisotropic geometric structures, their intracluster electric field shows strong anisotropy and affects their $\langle V \rangle$ part significantly.

As an example of such clusters, the author has noticed lanthanide-cyclooctatetraene sandwich clusters with characteristic one-dimensional structure and strong ionic bonding. In Chapters 3 and 4, the author will perform theoretical studies for their electronic properties which reflect their one-dimensional strong ionic bonding.

1.3. Concrete Subjects of This Thesis

1.3.1. Photoabsorption in the Herzberg I Band of O_2 Molecule

Molecular oxygen dominates atmospheric chemistry completely because of its great

abundance, reactivity, and photosensitivity in the atmosphere. Molecular nitrogen, in comparison, is more abundant but chemically inert and essentially transparent to solar radiation. [1.14]

The Herzberg I band system $\left(A^3\Sigma_u^+ \leftarrow X^3\Sigma_g^-\right)$ of O_2 can be seen in the 240-285 nm region as the major part of the Herzberg band system. [1.14] The absorption band is utilized for the measurement of oxygen concentration in the air and its absorption intensity is of crucial importance in the ozone formation in the stratosphere. However, electronic transitions in the Herzberg band system are forbidden by the electronic symmetry selection rule $+ \nleftrightarrow -$ in the Hund's case (a) representation, so that accurate measurement of its intensity had not been conducted until recent years and few theoretical attempts have been made at the absorption mechanism.

As mentioned above, the $+ \nleftrightarrow -$ selection rule is a particular rule that depends on the validity of the basis functions for electronic wave functions. In most cases, electronic wave function can be described by one electronic configuration. However, if some perturbations break down this approximation, it is necessary to represent one electronic state with some electronic configurations. For example, the wave functions of the *X* and *A* states can be written as follows. [1.10]

$$\begin{aligned} \left|X\,^3\Sigma_g^-\right\rangle &= \left|\,^3\Sigma_g^-\right\rangle + C_X\left|\,^3\Pi_g\right\rangle + \cdots \\ \left|A^3\Sigma_u^+\right\rangle &= \left|\,^3\Sigma_u^+\right\rangle + C_A\left|\,^3\Sigma_u^-\right\rangle + \cdots \end{aligned}, \qquad \text{(1-27)}$$

where C_X and C_A are expansion coefficients. Note that the left term of the upper equation expresses the electronic wave function of the *X* state, and the right terms denote the electronic configurations with the $^3\Sigma_g^-$ and $^3\Pi_g$ symmetries. Using the above electronic wave functions, we can obtain non-zero electric transition moment between the *X* and *A* states

which borrows the ${}^3\Sigma_g^- \leftrightarrow {}^3\Sigma_u^-$ and ${}^3\Sigma_u^+ \leftrightarrow {}^3\Pi_g$ transition moments through the ${}^3\Sigma_u^+ \Leftrightarrow {}^3\Sigma_u^-$ and ${}^3\Sigma_g^- \Leftrightarrow {}^3\Pi_g$ perturbations. This concept is usually called as 'intensity borrowing'.

England et al. employed simple intensity borrowing model which considered the spin-orbit interaction (SO) and L-uncoupling (RO) as perturbations. [1.15]

$$A^3\Sigma_u^+ \overset{\text{SO}}{\Leftrightarrow} B^3\Sigma_u^- \xleftrightarrow{\mu_{//}} X\,{}^3\Sigma_g^-$$
$$A^3\Sigma_u^+ \xleftrightarrow{\mu_{\perp}} 1^3\Pi_g \overset{\text{SO}}{\Leftrightarrow} X\,{}^3\Sigma_g^-$$
$$A^3\Sigma_u^+ \xleftrightarrow{\mu_{\perp}} 1^3\Pi_g \overset{\text{RO}}{\Leftrightarrow} X\,{}^3\Sigma_g^-$$

Some experimental groups have used this simple model for the analysis of the absorption intensity of the I band system, [1.16-19] however, the author has one question for this model, namely, 'Are there no other important electronic states which couple with the *X* and *A* states? '

Thus, in Chapter 2, the author will develop two other theoretical models for the absorption mechanism, and discuss their validity for calculating the vibrational and rotational line strength of the I band system. In the chapter, we will see that the above simple model easily leads to erroneous results for weak forbidden band systems.

1.3.2. Geometric and Electronic Structure of One-Dimensional Lanthanide-Cyclooctatetraene Sandwich Cluster

Firstly, the author summarizes the basic character of the Eu atom and COT molecule.

Eu atom [1.20,21]

Atomic Number: 63

Ground state Electron Configuration (Ionization Energy): $[Xe]4f^7 6s^2$ (5.67eV)

Oxidation Ground States (Ionization Energy, Ionic Radius):

Eu^{+}/ $[Xe]4f^{7}6s^{1}$ (11.24 eV, 1.4~1.6 Å), Eu^{2+}/ $[Xe]4f^{7}$ (24.92 eV, 1.31 Å)

Eu^{3+}/ $[Xe]4f^{6}$ (42.70 eV, 1.09 Å)

COT molecule [1.22-25]

Geometric Structure

Neutral Ground State:D_{2d} ($^1A_1$)

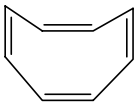

D_{2d}

Neutral Excited State: D_{4h} ($^1A_{1g}$), D_{8h} ($^3A_{2g}$), C_{2h} (^1A_g), D_4 ($^1A_1$)

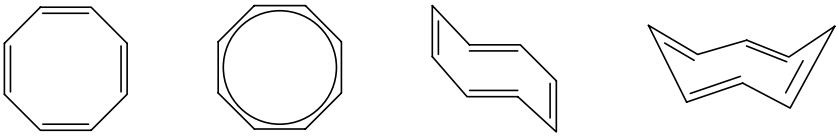

D_{4h} D_{8h} C_{2h} D_4

Anion Ground State: D_{4h} ($^2B_{2g}$) (same C-C-C bond angles, two C-C bond distances)

Anion Excited State: D_{4h} ($^2B_{1g}$) (same C-C bond distances, two C-C-C bond angles), D_{8h} ($^2E_{2u}$)

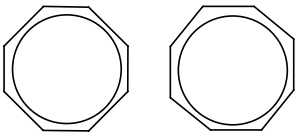

D_{4h} (bond) D_{4h} (angle)

Dianion Ground State: D_{8h} ($^1A_{1g}$) (Not isolated in gas phase. Its life time is calculated as 6.0 fs [1.23])

Relative Energies (eV) for Various Geometries

Neutral

D_{2d}	D_{4h}	D_{8h}	C_{2h}	D_4
0	0.74	0.84	2.45	7.41

Note. experimental electron affinity of neutral COT is 0.55 (eV)

Anion

D_{4h} (bond)	D_{4h} (angle)	D_{8h}
0	0.74	0.84

Note. All data are abstracted from *ab initio* calculation data Ref. [1.24,25].

The lanthanide (Ln) and 1,3,5,7-cyclooctatetraene (COT) sandwich clusters were originally

synthesized in the gas phase using a combination of laser vaporization techniques and molecular beam methods by Nakajima and co-workers. [1.26-28] Recently, Hosoya et al. have succeeded in synthesizing large europium (Eu) - COT sandwich clusters, named as sandwich nanowires, in the gas phase. [1.29] Interestingly, the Eu-COT sandwich nanowires were formed with up to one-dimensional 27 layers (about 10 nm overall length), thus such clusters have been the most probable candidates for quasi one-dimensional nanomaterials with many special electric and magnetic properties.

As shown in Fig. 1-1, the valence electronic configuration of the neutral COT has two holes, while that of the ground state of Eu has two outer valence electrons, so that the bonding scheme of $Eu_1(COT)_1$ cluster is easily considered as the ionic bond between the Eu^{2+} cation and COT^{2-} anion due to the charge transfer from Eu to COT.

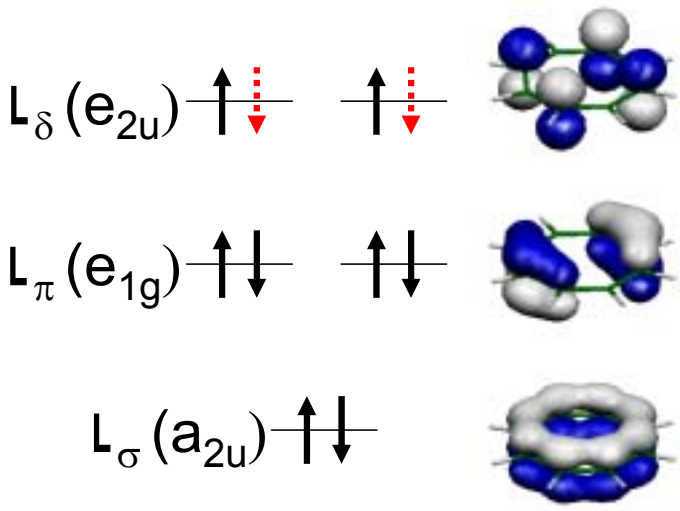

Fig. 1-1 Valence π molecular orbitals. Neutral COT has 8 π electrons (Black arrows), and two holes. (Red arrows.)

As discussed in Chapters 3 and 4, the electron affinity (EA) and ionization energy (E_i) of $Eu_1(COT)_1$ are about 0.8 and 6.0 (eV), respectively, and the electronic structure of the anion and cation clusters are Eu^+COT^{2-} and $Eu^{2+}COT^-$. These values are much smaller and larger than EA of the bare Eu^{2+} atom (5.67 (eV)) and E_i of the bare COT^{2-} molecule (negative E_i),

because EA of Eu^{2+} decreases due to the repulsive interaction with COT^{2-}, on the other hand, E_i of COT^{2-} increases owing to the attractive interaction with Eu^{2+}.

These phenomena are generally found in most lanthanide (Ln) compounds, because they have and oxidation state of Ln^{3+} and strong ionic bonding. [1.30,31] Especially, since the Ln-COT sandwich clusters have one-dimensional strong ionic structures, their anisotropic electrostatic field is assumed to affect their electronic properties significantly. Therefore, the author was interested in the theoretical investigations for the electronic properties of Ln-COT.

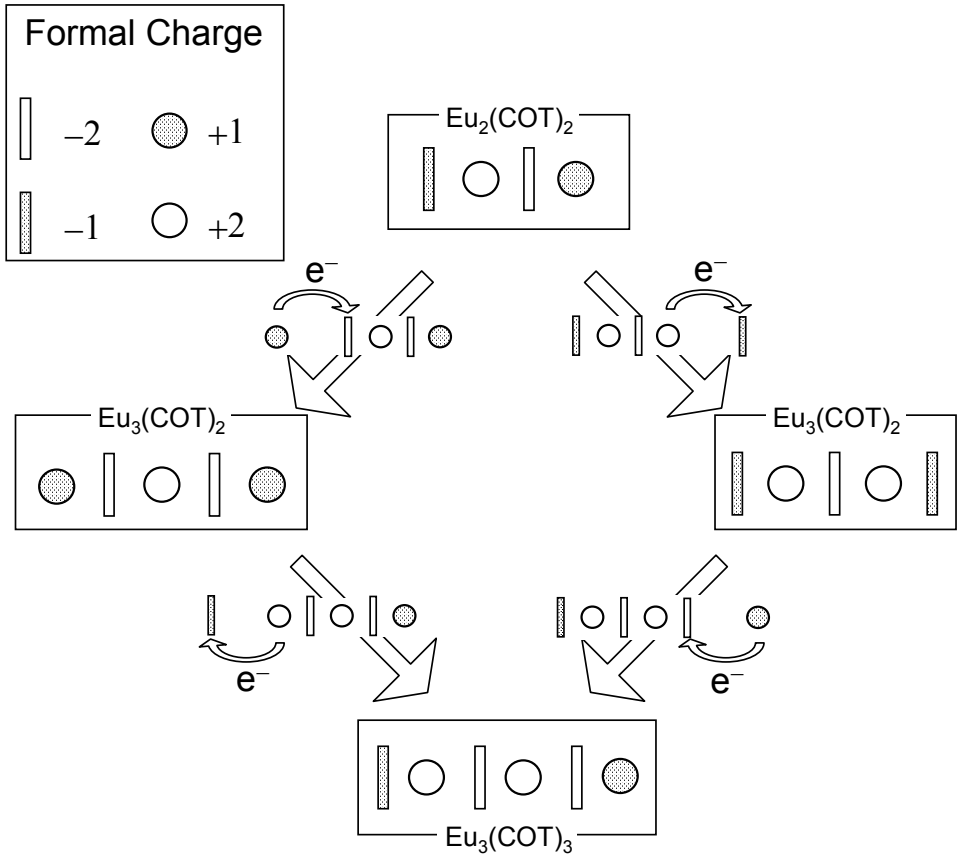

Fig. 1-2 Sequential harpoon mechanism for growth of Eu-COT. The dotted and white circles denote +1 and +2 charged metals, and dotted and white plates denote −1 and − 2 charged COT ligands, respectively.

In addition, Hosoya et al. also considered the sequential harpoon mechanism for growth processes extending the length of Eu-COT nanowires in which efficient charge transfer occurs

at the terminal reaction sites as shown Fig. 1-2. [1.29] In this mechanism, one-end open sandwich clusters $Eu_n(COT)_n$ are key intermediates, so that accurate determination of their geometric and electronic structure is of curial importance. In addition, the photoelectron and photoionization spectra of $Eu_n(COT)_n$ show characteristic behaviors which depend strongly on the cluster size.

Thus, the author has performed the theoretical investigations for one-end open sandwich clusters $Eu_n(COT)_n$. In Chapter 3, he will give the theoretical analysis for the geometric and electronic structure of their anion $Eu_n(COT)_n^-$, and assign their photoelectron spectra. He will also develop simple 'point charge models' to clarify the characteristic behavior of the photoelectron spectra. In Chapter 4, he will also investigate the ionization energy and electron distribution of the neutral $Eu_n(COT)_n$ which behave uniquely as their cluster size and electronic state change.

Reference

[1.1] P.A.M. Dirac, Proc. Roy. Soc. A 123 (1929) 714.

[1.2] Program system Gaussian 98, M.J. Frisch et al., Gaussian Inc., Pittsburgh, PA, 1998.

[1.3] Program system GAMESS, M.W. Schmidt et al., J. Comput. Chem. 14 (1993) 1347.

[1.4] Program system COLUMBUS, R. Shepard et al., Intern. J. Quantum. Chem. Symp. 22 (1988) 149.

[1.5] S. Huzinaga, Molecular Orbital Method. Iwanami (1980) in Japanese.

[1.6] A. Szabo, N.S. Ostlund, Modern Quantum Chemistry: Introduction to Advanced Electronic Structure Theory. Macmillan, New York. (1982)

[1.7] D.R. Yarkony (ed.), Modern Electronic Structure Theory. World Scientific, London. (1995)

[1.8] P.W. Atkins, R.S. Friedman, Molecular Quantum Mechanics. Oxford University Press, New York. (1997)

[1.9] G. Herzberg, Spectra of Diatomic Molecules. Van Nostrand-Reinhold, Princeton, New Jersey. (1950)

[1.10] H. Lefebvre-Brion, R.W. Field, Perturbations in the Spectra of Diatomic Molecules. Academic Press, Orlando. (1986)

[1.11] J.H. van Vleck, Rev. Mod. Phys. 23, (1951) 213.

[1.12] R.N. Zare, Angular Momentum. Wiley-Interscience Publication, New York. 1988.

[1.13] K. Balasubramanian, Relativistic Effects in Chemistry, John Wiley & Sons, New York, (1997)

[1.14] D.H. Parker, Acc. Chem. Res. 33 (2000) 563.

[1.15] J.P. England, B.R. Lewis, S.T. Gibson, Can. J. Phys. 74 (1996) 185.

[1.16] R. Klotz, S.D. Peyerimhoff, Mol. Phys. 57 (1986) 573.

[1.17] K. Tonokura, N. Shafer, Y. Matsumi, M. Kawasaki, J. Chem. Phys. 95 (1991) 3394.

[1.18] B. Buijsse, W.J. van der Zande, A.T.J.B. Eppink, D.H. Parker, B.R. Lewis, S.T. Gibson, J. Chem. Phys. 108 (1998) 7229.

[1.19] M.-F. Mérienne, A. Jenouvrier, B. Coquart, M. Carleer, S. Fally, R. Colin, A.C. Vandaele, C. Hermans, J. Mol. Spectrosc. 202 (2000) 171.

[1.20] L. Brewer, in: S.P. Sinha, (Ed.), NATO ASI Systematics and the Properties of the Lanthanides, Reidel, Dordrecht, 1983.

[1.21] W.C. Martin, R. Zalubas, L. Hagan, Atomic Energy Levels – The Rare-Earth Elements, NSRDS-NBS 60, 1978.

[1.22] P.G. Wenthold, D.A. Hrovat, W.T. Borden, W.C. Lineberger, Science. 272 (1996) 1456.

[1.23] T. Sommerfeld, J. Am. Chem. Soc. 124 (1992) 1119.

[1.24] J.H. Hammons, D.A. Hrovat, W.T. Borden, J. Am. Chem. Soc. 113 (1991) 4500.

[1.25] J.L. Andrés, O. Castaño, A. Morreale, R. Palmeiro, R. Gomperts, J. Chem. Phys. 108 (1998) 203.

[1.26] T. Kurikawa, Y. Negishi, F. Hayakawa, S. Nagao, K. Miyajima, A. Nakajima, K. Kaya, J. Am. Chem. Soc. 120 (1998) 11766.

[1.27] K. Miyajima, T. Kurikawa, M. Hashimoto, A. Nakajima, K. Kaya, Chem. Phys. Lett. 306 (1999) 256.

[1.28] A. Nakajima, K. Kaya, J. Phys. Chem. A. 104 (2000) 176.

[1.29] N. Hosoya, R. Takegami, J. Suzumura, K. Yada, K. Koyasu, K. Miyajima, M. Mitsui, M.B. Knickelbein, S. Yabushita, A. Nakajima, J. Phys. Chem. A. 109 (2005) 9.

[1.30] R.W. Field, Ber. Bunsenges. Phys. Chem. 86 (1982) 771.

[1.31] I. Gotkis, J. Phys. Chem. 95 (1991) 6086.

Chapter 2.

Photoabsorption in

the Herzberg I Band of O_2 Molecule

Abstract

The Herzberg I band system of the oxygen molecule is electric-dipole forbidden and its absorption strength has been explained by intensity borrowing models which include the spin-orbit(SO) and L-uncoupling(RO) interactions as perturbations. The author employed three different levels of theoretical models to evaluate these two interactions, and obtained the rotational and vibronic absorption strengths using the *ab initio* method. The first model calculates the transition moments induced by the SO interaction variationally with the SO configuration interaction method (SOCI), and uses the first-order perturbation theory for the RO interaction, and is called SOCI. The second is based on the first-order perturbation theory for both the SO and RO interactions, and is called Pert(Full). The last is a limited version of Pert(Full), in that the first-order perturbation wave function for the initial and final state is represented by only one dominant basis, namely the $1^3\Pi_g$ and $B^3\Sigma_u^-$ state respectively, as originally used by England et al. [J.P. England, B.R. Lewis, and S.T. Gibson, Can. J. Phys. 74 (1996) 185-193], and is called Pert(England). The vibronic oscillator strengths calculated by

these three models were in good agreement with the experimental values. As for the integrated rotational line strengths, the SOCI and Pert(Full) models reproduced the experimental results very well, however the Pert(England) model did not give satisfactory results. Since the Pert(England) model takes only the $1^3\Pi_g$ and $B^3\Sigma_u^-$ states into consideration, it cannot contain the complicated configuration interactions with highly excited states induced by the SO and RO interaction, which plays an important role for calculating the delicate integrated rotational line strength. This result suggests that the configuration interaction with highly excited states due to some perturbations cannot be neglected in the case of very weak absorption band systems.

2.1. Introduction

The oxygen molecule plays an important role in the atmospheric chemistry on the earth, so there has been a considerable interest in this molecule. [2.1] Its importance comes from the great abundance, reactivity and photosensitivity in the atmosphere, and detailed spectroscopic information is available. However, due to the complex electronic structures, all of its fundamental properties have not been clear till now. In recent years, several experimental and theoretical groups have re-investigated this molecule. [2.1-2.9]

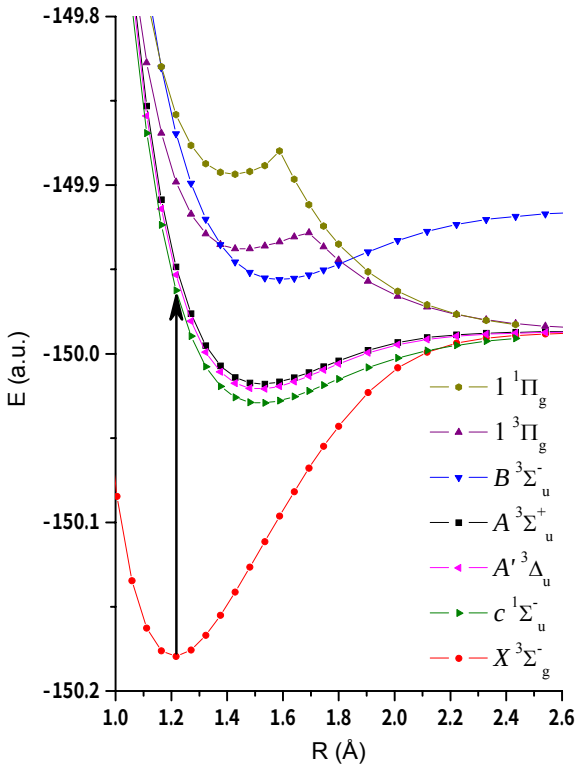

Fig. 2-1 Calculated potential energy curves in the low-lying energy region. The arrow shows the Herzberg band excitations.

The absorption of the Herzberg band systems is a key step of the ozone formation in the stratosphere, and has been utilized for the measurement of the oxygen concentration. The

absorption in the spectral region under investigation consists of three band systems (I, II and III), each of which is made of several vibrational bands.

$$\text{I band system: } A^3\Sigma_u^+ \leftarrow X^3\Sigma_g^-, \qquad (2\text{-}1)$$

$$\text{II band system: } c^1\Sigma_u^- \leftarrow X^3\Sigma_g^-, \qquad (2\text{-}2)$$

$$\text{III band system: } A'^3\Delta_u \leftarrow X^3\Sigma_g^-, \qquad (2\text{-}3)$$

and is represented by the arrow in Fig. 2-1. All of the sub-bands are electric dipole-forbidden by symmetry selection rules. Therefore, laboratory measurements of the band systems are difficult because of their small cross sections.

The I band system can be seen in the 240-285nm region as the major part of the Herzberg band system. [2.1,3,7,8] Based on the Hund's case (a) representation, $\Sigma^+ - \Sigma^-$ transitions are forbidden by the $+ \nleftrightarrow -$ symmetry selection rule. [2.10] In fact, they can borrow the intensity from allowed transitions through some perturbations. Each vibrational band consists of 13 rotational branches. [2.11] The relative intensities of these branches vary by orders of magnitude and depend strongly on the relative strengths of the electronic interactions.

Yoshino et al. measured the integrated absorption cross sections of this band system for individual rotational lines of 10 branches for the (4,0)-(11,0) bands and estimated vibronic oscillator strengths. [2.2,3] Recently, Jenouvrier and co-workers measured more detailed absorption cross sections for individual rotational lines of the three band systems, and determined the vibronic oscillator strength. [2.7,8]

Theoretical formulae on the rotational line strengths of the ${}^3\Sigma_u^+ - {}^3\Sigma_g^-$ transitions were obtained previously, and particular attention was devoted to the $A^3\Sigma_u^+ - X^3\Sigma_g^-$ transition. [2.12-2.15] Lewis et al. derived the formulae of the line strength and calculated the relative strengths of the 13 branches in this transition. [2.12] They employed an intensity-borrowing

model which considered the spin-orbit (SO) interactions of $^3\Sigma^{\pm} - ^3\Sigma^{\mp}$ and $^3\Pi - ^3\Sigma^{\pm}$ as perturbations. More general formulae including the SO and L-uncoupling (RO) were derived by Bellary et al. [2.13] Huestis et al. noted that the ^QQ rotational branches were strongly affected by RO interaction. [2.14] Hence, the rotational perturbation terms can be essential to explain the rotational line strengths. England et al. [2.16] used the formulae derived by Bellary et al. and estimated some electronic transition moment parameters to fit the integrated absorption cross sections for rotational lines measured by Yoshino et al. They found that a good fit was obtained with only three independent parameters. Mérienne et al. [2.8] also determined new values of these parameters in the same procedure as England et al. Although there have been several studies on the absorption process of this band system as stated above, no concrete consensus has been made concerning the degree of theoretical sophistication necessary for the perturbations.

As for *ab initio* studies on electronic transitions in the low-lying states, Klotz et al. calculated the electronic transition moments and vibronic oscillator strengths of the three Herzberg band systems. [2.17] However, their values are not in good agreement with the recent experimental data, moreover they did not include the rotational perturbations. Minaev computed the electric-dipole, electric-quadrupole, and magnetic-dipole transition moments from metastable states in the 190-300nm region. [2.18] Minaev et al. also studied about 20 singlet and 20 triplet valence states and calculated the electric-dipole allowed transition moments among these states. [2.19] However, there has been no *ab initio* study that calculated the rotational line strengths of the Herzberg band systems including the rotational perturbations, and it can be an attractive challenge for theoreticians.

Vroonhoven et al. performed theoretical studies on the photodissociation process from the Herzberg band excitations, and obtained the physical insight for the potential energy curves in

the dissociation region. [2.20,21] For example, they calculated the anisotropy parameters by using their theoretical potential curves and the experimental values [2.6] for the parallel and perpendicular branching ratios of the Herzberg transitions. If we have accurate transition moments for the initial excited state populations, we can obtain genuine theoretical anisotropy parameters and remove the ambiguity discussed in Ref [2.21]. Another interest to study the anisotropy parameter is the relatively large difference in the existing experimental values. The author hopes that additional *ab initio* calculations of the transition moments may help to resolve the remaining difficulties.

As we have seen, in spite of various works on the Herzberg band systems, some questions still remain to be answered. Such problems might be solved with direct theoretical analyses. Moreover, to the best of my knowledge, there has been no study that attempted to simulate the rotational line strengths of the electric-forbidden band using the transition moments obtained by the *ab initio* calculation. Such a study is essential to examine the accuracy of the *ab initio* transition moments. In this chapter, the author calculates the transition moment parameters, and estimates the integrated rotational line strengths and vibronic oscillator strengths, employing three different levels of theoretical models to include the SO and RO interactions. The theoretical values obtained by these models are compared with the experimental ones. The anisotropy parameter for the photodissociation products is also calculated to compare with the experimental ones. This study provides a special insight in the SO and RO interactions and configuration interactions in this molecule, and offers a key role to an analysis of electric-dipole forbidden bands of other important molecules in atmospheric chemistry.

2.2. Theory

2.2.1. Summary of Basic Theory

General methods for the calculation of rotational line strength are well known; a particularly clear review was given by Whiting and Nicholls. [2.22] The rotational line strength $S_{v'J'vJ}$ of an electric-dipole transition is proportional to the squared value of the transition moment $M(a,b)$.

$$M(a,b) = \left\langle a \middle| \boldsymbol{\mu}_{eff} \middle| b \right\rangle, \qquad (2\text{-}4)$$

with

$$\boldsymbol{\mu}_{eff} = \frac{1}{2}\left(\phi_{Zx} + i\phi_{Zy}\right)\left(\boldsymbol{\mu}_x - i\boldsymbol{\mu}_y\right) + \frac{1}{2}\left(\phi_{Zx} - i\phi_{Zy}\right)\left(\boldsymbol{\mu}_x + i\boldsymbol{\mu}_y\right) + \phi_{Zz}\boldsymbol{\mu}_z, \qquad (2\text{-}5)$$

$$\left|a\right\rangle = \left|e_a\right\rangle\left|v_a\right\rangle\left|r_a\right\rangle, \qquad (2\text{-}6)$$

Here $\boldsymbol{\mu}_\alpha$ is the α th molecule-fixed component of the electric-dipole moment operator and ϕ_{Ij} is the direction cosine operator which relates the j th molecule-fixed axis to the I th space-fixed axis. The ket $\left|a\right\rangle$ is the total wave function which is approximated by the product of the electronic, vibrational, and rotational wave functions, and is usually called Born-Oppenheimer wave function. The operator ϕ_{Ij} only operates on the rotational wave function, and $\boldsymbol{\mu}_\alpha$ operates on the electronic and vibrational wave functions. Therefore, the $M(a,b)$ is reduced as follows.

$$\begin{aligned} M(a,b) = &\left\langle v_a \middle| \left\langle e_a \middle| \boldsymbol{\mu}_- \middle| e_b \right\rangle \middle| v_b \right\rangle \left\langle r_a \middle| \phi_+ \middle| r_b \right\rangle + \left\langle v_a \middle| \left\langle e_a \middle| \boldsymbol{\mu}_+ \middle| e_b \right\rangle \middle| v_b \right\rangle \left\langle r_a \middle| \phi_- \middle| r_b \right\rangle \\ &+ \left\langle v_a \middle| \left\langle e_a \middle| \boldsymbol{\mu}_z \middle| e_b \right\rangle \middle| v_b \right\rangle \left\langle r_a \middle| \phi_{Zz} \middle| r_b \right\rangle \end{aligned}, \qquad (2\text{-}7)$$

$$\boldsymbol{\mu}_{\pm} = \frac{1}{\sqrt{2}}\left(\boldsymbol{\mu}_x \pm i\boldsymbol{\mu}_y\right), \qquad (2\text{-}8)$$

$$\phi_{\pm} = \frac{1}{\sqrt{2}}\left(\phi_{Zx} \pm i\phi_{Zy}\right), \qquad (2\text{-}9)$$

The matrix elements of the rotational wave function are tabulated conveniently in general text book. [2.10]

Now, we come to the matrix elements of the electronic and vibrational wave functions. Actual values of these matrix elements depend on approximation methods used in the electronic wave functions. Without any electronic perturbations, the $^3\Sigma^+ - ^3\Sigma^-$ transition is not allowed. Both Lewis et al. and Klotz et al. considered only the SO interaction for perturbation. [2.12,17] Later, Bellary et al. and England et al. included also the RO interaction. [2.13,16] Thus, it is interesting to know the relative importance of these perturbations.

The actual computational method for these interactions is also an essential point. Most of the previous workers have calculated the electronic wave functions perturbed by the SO and RO interactions using the first-order perturbation theory within the small subspace of selected bases in the sum-over-states representation. However, for more accurate calculation, it is desired to use the perturbation or the variational theory without basis set selection.

2.2.2. Methods for the Electronic Transition Moments

The author employs the formulae of Bellary et al. [2.13] with the three models to calculate the electronic transition moments of the Herzberg I band system, called the SOCI, Pert(Full), and Pert(England) models. It has been believed that the SO interaction is the primary source of the absorption strength in the Herzberg I band system, and the RO interaction makes a secondary contribution to the rotational line strength. Therefore, the SOCI model employs the

variational CI method for the SO interaction and the first-order perturbation theory for the RO interaction. The Pert(Full) model is based on the first-order perturbation theory for these two interactions. The last one follows the work of England et al. in which each of the initial and final wave functions is expanded with only two spin-free electronic wave functions, one dominant and the other perturbing, employing the first-order perturbation theory. The author shall describe some details of the three models in the following sub-sections.

SOCI Model

The SOCI method employs the following total electronic Hamiltonian *H* including the SO part approximated in the one-electron operator form, and variationally calculates the electronic eigenfunctions corresponding to the Hund's case (c) base.

$$H = H_{el} + H_{SO}, \qquad (2\text{-}10)$$

$$H_{SO} = \sum_i \hat{a}_i \hat{\mathbf{l}}_i \cdot \hat{\mathbf{s}}_i \qquad with \quad \hat{a}_i \hat{\mathbf{l}}_i = \sum_K \frac{\alpha^2}{2} \frac{Z_{\mathrm{eff},K}}{r_{iK}^3} \hat{\mathbf{l}}_{iK}, \qquad (2\text{-}11)$$

where α is the fine-structure constant, $\alpha = e^2/\hbar c$, $\hat{\mathbf{l}}_{iK}$ is the orbital angular momentum of electron *i* about nucleus *K*, $Z_{\mathrm{eff},K}$ is the effective charge of the *K* th nucleus. Of the three models described before, this SOCI method provides the most accurate electronic wave functions perturbed by the SO interaction.

The author treats the SOCI wave function as the zero-th order base for the Herzberg I band system, and evaluate the RO interaction with the first-order perturbation theory. The RO interaction is written as follows.

$$H_{RO} = -B_v \left(\mathbf{J}^+ \mathbf{L}^- + \mathbf{J}^- \mathbf{L}^+ \right). \qquad (2\text{-}12)$$

Here, $\mathbf{J}^{\pm}$ is the molecule-fixed raising and lowering operators of the total angular momentum, $\mathbf{L}^{\mp}$ is the raising and lowering operators of the total electronic orbital angular

momentum, and

$$B_v = \left\langle v \left| \frac{\hbar^2}{2\mu R^2} \right| v \right\rangle . \qquad (2\text{-}13)$$

Then, the initial and final wave functions are constructed following the procedure of the Bellary et al. [2.13] For example, $\Omega = 1$ and *e* symmetry components of the initial and final total wave functions are as follows,

$$\begin{aligned} \left| A^3\Sigma_{1u}^+, J', e \right\rangle = & \left| A^3\Sigma_{1u}^+, J', - \right\rangle \\ & + \left[(J'-1)(J'+2) \right]^{1/2} \sum_{n_{2u}} b'(n_{2u}) \left| n_{2u}, J', - \right\rangle , \\ & - \left[J'(J'+1) \right]^{1/2} \sum_{n_{0u}} b'(n_{0u}) \left| n_{0u}, J', - \right\rangle \end{aligned} \qquad (2\text{-}14)$$

$$\begin{aligned} \left| X^3\Sigma_{1g}^-, J, e \right\rangle = & \left| X^3\Sigma_{1g}^-, J, + \right\rangle \\ & + \left[(J-1)(J+2) \right]^{1/2} \sum_{m_{2g}} b(m_{2g}) \left| m_{2g}, J, - \right\rangle , \\ & - \left[J(J+1) \right]^{1/2} \sum_{m_{0g}} b(m_{0g}) \left| m_{0g}, J, - \right\rangle \end{aligned} \qquad (2\text{-}15)$$

where $\left| n_\Omega, J, \pm \right\rangle$ is the symmetrized wave function,

$$\left| {}^{2S+1}\Lambda_\Omega, J, \pm \right\rangle = 2^{-1/2} \left[\left| {}^{2S+1}\Lambda_\Omega, \Omega, J, M \right\rangle \pm \left| {}^{2S+1}\Lambda_{-\Omega}, -\Omega, J, M \right\rangle \right]. \qquad (2\text{-}16)$$

and n_Ω and m_Ω denote ${}^{2S+1}\Lambda_\Omega$, the electronic eigenfunctions of Eq. (2-10). Therefore, the good quantum number of these electronic wave functions is Ω. [2.10] The symbol ' represents quantities of the final electronic state, and $b(m_\Omega)$ and $b'(n_\Omega)$ are the expansion coefficients for the initial and final electronic state, respectively. In Eqs. (2-14) and (2-15), $b'(n_\Omega)$ and $b(m_{0g})$, for example, are given by the perturbation method as follows.

$$b'(n_{0u}) = -B_v \frac{\left\langle n_{0u} \left| \mathbf{L}^- \right| A^3\Sigma_{1u}^+ \right\rangle}{E\left(A^3\Sigma_{1u}^+\right) - E(n_{0u})}, \qquad (2\text{-}17)$$

$$b(m_{0g}) = -B_v \frac{\langle m_{0g} | \mathbf{L}^- | X\,^3\Sigma_{1g}^- \rangle}{E(X\,^3\Sigma_{1g}^-) - E(m_{0g})}, \qquad (2\text{-}18)$$

In the actual calculation, all the n_Ω and m_Ω states were chosen within the CI space, which can couple with the initial and final states through the RO interaction.

Next, the symmetry selection rules, $\Delta J = 0 (e \leftrightarrow f)$ and $\Delta J = 1 (e \leftrightarrow e, f \leftrightarrow f)$ are considered, and 13 electronic transition moments are obtained. In the procedure of Bellay et al., these electronic transition moments can be simply re-expressed by 13 independent parameters. They noted that, in the limit of small perturbation of the SO and RO interactions, these parameters can be further reduced to only three by the symmetry properties of the electronic wave functions and by omitting small second-order parameters. Accuracy of such approximation will be examined later.

Then, these three electronic transition moment parameters are defined as follows.

$$Z = \sqrt{2} \langle X\,^3\Sigma_{1g}^- | \boldsymbol{\mu}_z | A^3\Sigma_{1u}^+ \rangle, \qquad (2\text{-}19)$$

$$X = \sqrt{2} \langle X\,^3\Sigma_{1g}^- | \boldsymbol{\mu}_+ | A^3\Sigma_{0^-u}^+ \rangle, \qquad (2\text{-}20)$$

$$\begin{aligned} M &= M_g + M_u \\ &= \sum_m b(m_{0g}) \langle m_{0g} | \boldsymbol{\mu}_- | A^3\Sigma_{0^-u}^+ \rangle + \sum_n b'(n_{0u}) \langle X\,^3\Sigma_{1g}^- | \boldsymbol{\mu}_+ | n_{0u} \rangle. \end{aligned} \qquad (2\text{-}21)$$

Pert(Full) and Pert(England) Models

Next, the perturbation theory is used for both the SO and RO interactions, and H_{el} in Eq. (2-10) is chosen as the zero-th order Hamiltonian for the electronic wave functions, and therefore the eigenfunctions correspond to the Hund's case (a) base.

If the initial and final electronic wave functions are constructed by the first-order perturbation theory with the complete Hund's case (a) base, the 13 parameters for the 13 electronic transition moments can be defined. Due to the symmetry properties of the

electronic wave functions and omitting second-order parameters, these transition moment parameters can be reduced to only three as in the previous sub-section. This model is called Pert(Full), and the three transition parameters are defined as follows.

$$\begin{aligned} Z &= Z_g + Z_u \\ &= \sqrt{2}\left\{ \sum_m \alpha(m) \left\langle m \middle| \boldsymbol{\mu}_z \middle| A^3\Sigma_u^+ \right\rangle + \sum_n \alpha'(n) \left\langle X^3\Sigma_g^- \middle| \boldsymbol{\mu}_z \middle| n \right\rangle \right\}, \end{aligned} \tag{2-22}$$

$$\begin{aligned} X &= X_g + X_u \\ &= \sum_m a(m) \left\langle m \middle| \boldsymbol{\mu}_+ \middle| A^3\Sigma_u^+ \right\rangle + \sum_n a'(n) \left\langle X^3\Sigma_g^- \middle| \boldsymbol{\mu}_- \middle| n \right\rangle, \end{aligned} \tag{2-23}$$

$$\begin{aligned} M &= M_g + M_u \\ &= \sum_m b(m) \left\langle m \middle| \boldsymbol{\mu}_- \middle| A^3\Sigma_u^+ \right\rangle + \sum_n b'(n) \left\langle X^3\Sigma_g^- \middle| \boldsymbol{\mu}_+ \middle| n \right\rangle. \end{aligned} \tag{2-24}$$

Here, *m* and *n* are the Hund's case (a) base and their good quantum numbers are Λ, S, and Σ.[2.10] For example, $\alpha(m)$ and $a(m)$ are the expansion coefficients for the initial state considering SO interaction as perturbation, and $a(m)$ is the coefficient for the $\Lambda = 0(\Sigma)$ component, and $a(m)$ and $b(m)$ for the $\Lambda = 1(\Pi)$ component. For instance, $\alpha(m)$, $a(m)$ and $b(m)$ are expressed as follows.

$$\alpha(m) = \frac{\left\langle X^3\Sigma_g^- \middle| H_{SO} \middle| m(\Sigma) \right\rangle}{E(m(\Sigma)) - E\left(X^3\Sigma_g^-\right)}, \tag{2-25}$$

$$a(m) = \frac{\left\langle X^3\Sigma_g^- \middle| H_{SO} \middle| m(\Pi) \right\rangle}{E(m(\Pi)) - E\left(X^3\Sigma_g^-\right)}, \tag{2-26}$$

$$b(m) = -B_v \frac{\left\langle X^3\Sigma_g^- \middle| \mathbf{L}^- \middle| m(\Pi) \right\rangle}{E(m(\Pi)) - E\left(X^3\Sigma_g^-\right)}. \tag{2-27}$$

Next, more approximately, the first-order perturbation theory is used within the subspace of the selected Hund's case (a) base in the sum-over-states representation. England et al. considered the model in which the initial $X^3\Sigma_g^-$ state was only perturbed by the first $^3\Pi_g$

state through SO and RO interactions, and the final $A^3\Sigma_u^+$ state was only perturbed by the $^3\Pi_g$ state. If these basis states are selected as England et al., the three reduced parameters can be defined as follows.

$$Z = \sqrt{2}\alpha'\left(B^3\Sigma_u^-\right)\left\langle X^3\Sigma_g^- \middle| \boldsymbol{\mu}_z \middle| B^3\Sigma_u^- \right\rangle, \tag{2-28}$$

$$X = a\left(1^3\Pi_g\right)\left\langle 1^3\Pi_g \middle| \boldsymbol{\mu}_+ \middle| A^3\Sigma_u^+ \right\rangle, \tag{2-29}$$

$$M = b\left(1^3\Pi_g\right)\left\langle 1^3\Pi_g \middle| \boldsymbol{\mu}_+ \middle| A^3\Sigma_u^+ \right\rangle, \tag{2-30}$$

and $\alpha'\left(B^3\Sigma_u^-\right)$, $a\left(1^3\Pi_g\right)$ and $b\left(1^3\Pi_g\right)$ are as follows.

$$\alpha'\left(B^3\Sigma_u^-\right) = \frac{\left\langle B^3\Sigma_u^- \middle| H_{SO} \middle| A^3\Sigma_u^+ \right\rangle}{E\left(A^3\Sigma_u^+\right) - E\left(B^3\Sigma_u^-\right)} \tag{2-31}$$

$$a\left(1^3\Pi_g\right) = \frac{\left\langle X^3\Sigma_g^- \middle| H_{SO} \middle| 1^3\Pi_g \right\rangle}{E\left(1^3\Pi_g\right) - E\left(X^3\Sigma_g^-\right)}, \tag{2-32}$$

$$b\left(1^3\Pi_g\right) = -B_v \frac{\left\langle X^3\Sigma_g^- \middle| \mathbf{L}^+ \middle| 1^3\Pi_g \right\rangle}{E\left(1^3\Pi_g\right) - E\left(X^3\Sigma_g^-\right)}, \tag{2-33}$$

This transition model is called Pert(England).

Lastly, a brief comment is given on the vibrational wave functions. To calculate the absorption strengths at the room temperature, the centrifugal distortion effect should be included for each vibrational wave function. The vibrational potential curve including the centrifugal distortion term is as follows.

$$V_{eff}^{(N)}(R) = V(R) + \frac{\hbar^2 N(N+1)}{2\mu R^2} \quad (N = 1,3,5,\cdots), \tag{2-34}$$

$V(R)$ is the adiabatic potential curve as a function of the internuclear distance R and N is the rotational quantum number. The distorted vibrational wave function is calculated with the initial and final electronic potential curves and the centrifugal distortion term corresponding to each transition model.

2.2.3. Absorption Strength

Integrated Rotational Line Cross Section

The author calculates the three parameters in each model, and evaluates the rotational line strength $S_{v'J'vJ}$ derived by Bellary et al.[2.13] To calculate the rotational line strengths, the eigenfunctions of the three rotational term series $F_i(J)(i=1, 2, 3)$ of $A^3\Sigma_u^+$ and $X^3\Sigma_g^-$ are also needed. The mixing coefficients c'_J, s'_J, s_J and s_J were obtained with the Hamiltonian described by Cheung et al. [2.23] and the experimental molecular constants of Jenouvrier et al.[2.7] for the *A* state and those of Amiot et al.[2.24] for the *X* state.

The calculational line strengths $S_{v'J'vJ}$ can be related to the integrated line cross section $\sigma(\upsilon)$ by the following line oscillator strengths in cgs unit. [2.22]

$$f_{v'v} = \frac{m_e c^2}{\pi e^2 N_v} \int_{line} \sigma(\upsilon) d\upsilon = \frac{8\pi^2 m_e c}{3\hbar e^2 g} \left(\frac{\upsilon_{v'J'vJ} S_{v'J'vJ}}{2J+1} \right), \qquad (2\text{-}35)$$

where $g=3$ is the statistical weight of the ground state, m_e and e are the mass and the charge of an electron, υ and $\upsilon_{v'J'vJ}$ are the transition frequencies, $\hbar$ is Planck's constant divided by 2π. N_J is the relative population of the rotational level of the ground electronic and vibrational state, and is calculated by assuming the room temperature (293K).

Vibronic Oscillator Strength

The vibronic integrated line cross sections are evaluated by summing the calculated integrated strengths of all the rotational lines for the 13 branches as follows.

$$f_{v'v} = \frac{m_e c^2}{\pi e^2 N_v} \sum_{a=1}^{13} \sum_{N=1}^{oddN} \sigma(a, N). \qquad (2\text{-}36)$$

Here, N_v is the relative population of the vibrational level of the ground state at the room

temperature (293K), *a* denotes each branch, and *N* is the rotational quantum number.

2.3. Calculation Method

All the *ab initio* calculations were performed by the COLUMBUS program package. [2.25-27] Throughout this chapter, internuclear distance is given in Å, and transition moment in atomic unit. The multi-reference (MR)-CI method was used for the three models. As the one-electron orbitals, the state-averaged SCF molecular orbitals were employed by optimizing for the averaged state of all the configurations derived from $3\sigma_g, 1\pi_{ux}, 1\pi_{uy}, 1\pi_{gx}, 1\pi_{gy}$ and $3\sigma_u$, namely the six orbitals for eight electrons. Here, the six orbitals are the molecular orbitals correlating to 2p atomic orbitals of the oxygen atom. The configuration state functions (CSFs) were generated with the reference of the above complete active space.

In the SOCI model, for evaluating each electronic transition moment parameter, the initial and final state wave functions were calculated with the first-order SOCI method and the cc-pVTZ basis set. [2.28] The parameter $Z_{\mathrm{eff},K}$=5.84 was used in Eq. (2-11), which is appropriate for the SO splitting of the oxygen atom $\left({}^3P_J\right)$. The calculational and experimental (shown in parenthesis) SO splittings were 159.0 (158.5) cm^{-1} between ${}^3P_1$ and ${}^3P_2$, and 78.1 (68.0) cm^{-1} between ${}^3P_0$ and ${}^3P_1$. With these initial and final state wave functions, the *Z*, *X* and *M* electronic transition moment parameters in Eqs. (2-19)-(2-21) were obtained. In the calculation of the *M* parameter, the CSF representation instead of the sum-over-states representation was used, and the parameter was evaluated by solving linear equations employing the iterative algorithm by Pople et al. [2.29] Because these two representations are related by the unitary transformation, the equivalent value should be obtained by the two representations.

As for the Pert(Full) model, first, a spin-free first-order CI calculation was performed to obtain the initial and final state wave functions as the Hund's case(a) eigenfunctions with the cc-pVTZ basis set. Next, *Z*, *X* and *M* were calculated by solving linear equations equivalent to Eqs. (2-22)-(2-24) in the CSF representation. Calculations in the Pert(England) model were carried out in the same way as in the Pert(Full) model except that the $1^3\Pi_g$ and $B^3\Sigma_u^-$ states were employed in the sum-over states representation as in Eqs. (2-28)-(2-30) to obtain *Z*, *X* and *M*.

In the SOCI model, the vibrational wave functions were calculated with the potential curves derived from the contracted SO MR-SDCI(COSOCI) method with the cc-pVQZ basis set [2.28] with $Z_{\mathrm{eff},K}$=5.79, because this high level method was necessary to give the correct dissociation energies and shapes for the ground and excited potential curves. [2.20,30] The calculational SO splittings with these method were 159.0cm^{-1} between $^3P_1$ and $^3P_2$, and 79.4 cm^{-1} between $^3P_0$ and $^3P_1$. In the COSOCI method, first, a spin-free MR-SDCI calculation was performed to obtain the Hund's case (a) eigenvalues and eigenfunctions. Next, a small Hamiltonian matrix of Eq. (2-10), which is composed of the diagonal matrix elements of the Hund's case (a) eigenstates obtained above and the off-diagonal matrix elements of the SO interaction, was diagonalized, and then the eigenvalues and eigenfunctions including the SO interaction were obtained. All the electronic states correlating to the $^3P+^3P$ dissociation limit in the Hund's case (a) base are included. In the Pert(Full) and Pert(England) model, the spin-free MR-SDCI potential curves were used for the calculation of the vibrational wave functions. The vibration wave functions for each potential curve were calculated by the grid method with the *Mathematica* program. [2.31-34]

2.4. Results and Discussion

2.4.1. Comparison of Electronic Transition Moment Parameters in Three Models

Table 2-1 compares the computed electronic transition moment parameters at $R = 1.27$ Å as an example.

Table 2–1 Comparison of the transition moment parameters at *R*=1.27 Å calculated by five models.

	Pert(England)	Pert(3)	Pert(10)	Pert(Full)	SOCI (second–order)[a]
Z_g	0	-2.451×10^{-4}	-1.732×10^{-4}	-1.131×10^{-4}	
Z_u	1.231×10^{-3}	1.149×10^{-3}	1.083×10^{-4}	1.031×10^{-3}	
Z	1.231×10^{-3}	9.039×10^{-4}	9.098×10^{-4}	9.179×10^{-4}	9.079×10^{-4} (9.079×10^{-4})
X_g	2.153×10^{-4}	2.165×10^{-4}	2.331×10^{-4}	2.132×10^{-4}	
X_u	0	1.331×10^{-4}	1.174×10^{-4}	1.255×10^{-4}	
X	2.153×10^{-4}	3.496×10^{-4}	3.505×10^{-4}	3.387×10^{-4}	3.380×10^{-4} (3.380×10^{-4})
M_g	5.276×10^{-6}	5.347×10^{-6}	5.354×10^{-6}	4.584×10^{-6}	5.443×10^{-4}
M_u	0	5.734×10^{-6}	5.974×10^{-6}	5.631×10^{-6}	5.534×10^{-6}
M	5.276×10^{-6}	1.108×10^{-5}	1.132×10^{-5}	1.021×10^{-5}	1.097×10^{-5}

Note. Going from left to right, the calculational level becomes higher. The expression of each transition moment parameter is given in Eqs. (2-19)-(2-21), (2-22)-(2-24) and (2-28)-(2-30). Each value converges to the SOCI value as increasing the calculation level.

[a] The value calculated by the second–order perturbation theory for the SO interaction.

In the third (fourth) column of the table, calculation values obtained with the lower three (ten) intermediate states in the sum-over-states formulae in Eqs. (2-22)-(2-24) were added in order to examine the convergence.

Firstly, the author comments on the *Z* and *X* parameters. The *Z* and *X* parameters converge to the values of the SOCI model as increasing the calculation level. The Pert(England) model does not account for the $X^3\Sigma_g^- - n^3\Sigma_g^+$ and $A^3\Sigma_u^+ - n^3\Pi_u$ couplings, thus the values of Z_g, X_u and M_u were 0. However, in the higher level calculations, the relative magnitudes of these

couplings are not negligible at all in the total value of *Z*, *X* and *M*.

Table 2-2 shows the dominant expansion coefficients, $\alpha(m)$, $\alpha'(n)$, $a(m)$, and $a(n)$ in Eqs. (2-22) and (2-23).

Table 2–2 Dominant expansion coefficients, $\alpha(m)$, $\alpha'(n)$, $a(m)$ and $a'(n)$ calculated from Eqs. (2–22) and (2–23).

$\alpha(m)$ and $a(m)$		$\alpha'(n)$ and $a'(n)$	
$\alpha(1^3\Sigma_g^+)$	-2.287×10^{-5}	$\alpha'(B^3\Sigma_u^-)$	1.051×10^{-3}
$\alpha(2^3\Sigma_g^+)$	-8.290×10^{-5}	$\alpha'(2^3\Sigma_u^-)$	6.431×10^{-5}
$\alpha(3^3\Sigma_g^+)$	-1.415×10^{-4}	$\alpha'(3^3\Sigma_u^-)$	-3.741×10^{-5}
$\alpha(4^3\Sigma_g^+)$	-2.719×10^{-4}	$\alpha'(4^3\Sigma_u^-)$	9.910×10^{-5}
$\alpha(5^3\Sigma_g^+)$	-3.773×10^{-5}	$\alpha'(5^3\Sigma_u^-)$	1.489×10^{-5}
$a(1^3\Pi_g)$	1.429×10^{-3}	$a'(1^3\Pi_u)$	-4.038×10^{-5}
$a(2^3\Pi_g)$	3.935×10^{-4}	$a'(2^3\Pi_u)$	8.796×10^{-4}
$a(3^3\Pi_g)$	-3.594×10^{-4}	$a'(3^3\Pi_u)$	-4.871×10^{-5}
$a(4^3\Pi_g)$	-1.591×10^{-5}	$a'(4^3\Pi_u)$	-3.421×10^{-4}
$a(5^3\Pi_g)$	3.226×10^{-4}	$a'(5^3\Pi_u)$	3.679×10^{-4}

Here, the expansion coefficients of $1^3\Pi_g$ and $B^3\Sigma_u^-$ were by far the most important as supposed by England et al. [2.16] However, it is also found that other coefficients were not necessarily negligible. Especially, the $3^3\Sigma_g^+$, $4^3\Sigma_g^+$, $2^3\Pi_g$ and $3^3\Pi_g$ states have non-negligible expansion coefficient values in the *X* state, and the $2^3\Pi_u$, $4^3\Pi_u$, and $5^3\Pi_u$ states have considerable magnitudes in the *A* state.

Furthermore, Table 2-3 compared the contribution to each transition moment parameter, Z_g, X_g, Z_u and X_u of Eqs. (2-22) and (2-23), from above electronic states. It is also found that the values of $Z_u(B^3\Sigma_u^-)$ and $X_g(1^3\Pi_g)$ were the most important as supposed by England et al. [2.16] However, other values, for example, $Z_g(2^3\Sigma_g^+)$ and $X_u(2^3\Pi_u)$, were not negligible

Table 2–3 Contribution to Z_g, X_g, Z_u and X_u from each electronic state in Table 2-2.

$Z_g(m)$ and $X_g(m)$		$Z_u(n)$ and $X_u(n)$	
$Z_g\left(1^3\Sigma_g^+\right)$	-2.958×10^{-6}	$Z_u\left(B^3\Sigma_u^-\right)$	1.231×10^{-3}
$Z_g\left(2^3\Sigma_g^+\right)$	-1.608×10^{-4}	$Z_u\left(2^3\Sigma_u^-\right)$	9.061×10^{-5}
$Z_g\left(3^3\Sigma_g^+\right)$	-8.130×10^{-5}	$Z_u\left(3^3\Sigma_u^-\right)$	-8.265×10^{-5}
$Z_g\left(4^3\Sigma_g^+\right)$	4.185×10^{-5}	$Z_u\left(4^3\Sigma_u^-\right)$	-5.237×10^{-5}
$Z_g\left(5^3\Sigma_g^+\right)$	-6.301×10^{-14}	$Z_u\left(5^3\Sigma_u^-\right)$	4.043×10^{-5}
$X_g\left(1^3\Pi_g\right)$	2.153×10^{-4}	$X_u\left(1^3\Pi_u\right)$	9.614×10^{-7}
$X_g\left(2^3\Pi_g\right)$	-2.086×10^{-6}	$X_u\left(2^3\Pi_u\right)$	1.135×10^{-4}
$X_g\left(3^3\Pi_g\right)$	3.225×10^{-6}	$X_u\left(3^3\Pi_u\right)$	1.857×10^{-5}
$X_g\left(4^3\Pi_g\right)$	-1.007×10^{-6}	$X_u\left(4^3\Pi_u\right)$	8.169×10^{-6}
$X_g\left(5^3\Pi_g\right)$	1.709×10^{-5}	$X_u\left(5^3\Pi_u\right)$	7.589×10^{-6}

It is emphasized that the SO and RO interactions induce the small but non-negligible configuration interactions with highly excited states, and even these small interactions bring significant influence on the inherently small electronic transition moment parameters.

Although their values almost converged in the Pert(10) model, 40 % difference still persisted in Z_g. It is noticed that the Z_g and Z_u parameters converged smoothly to the Pert(Full) values, but other parameters did not. The X_g and X_u parameters converged to the Pert(Full) values with oscillation. The difference between the parameter values by the Pert(Full) and SOCI models was about 1% or less. One possible cause of this small difference is the omission of the second-order terms such as,

$$\sum_n \sum_m a'(n)a(m)\left\langle m\left|\boldsymbol{\mu}_z\right|n\right\rangle, \qquad (2\text{-}37)$$

in Eq. (2-22). Normalized the initial and final state first-order wave functions, the Z and X parameters were calculated including the above terms. Then, $Z = 9.158\times10^{-4}$ and $X = 3.386\times10^{-4}$ were obtained. Both parameters converged a little to the SOCI values, but

there still remain 0.87% and 0.18% differences in the *Z* and *X* parameter, respectively. Further, the second-order electronic wave functions perturbed by the SO interaction for the *X* and *A* states were calculated. For example, the perturbed wave function up to the second-order for the *X* state is as follows.

$$\left|X^3\Sigma_g^-\right\rangle = \left|X\right\rangle + \sum_{n\neq X}\frac{H'_{nX}}{E(X)-E(n)}\left|n\right\rangle + \sum_{n,m\neq X}\frac{H'_{mn}H'_{nX}}{\left(E(X)-E(m)\right)\left(E(X)-E(n)\right)}\left|m\right\rangle. \qquad (2\text{-}38)$$

Here, *X* is $X^3\Sigma_g^-$ and $H'_{ij} = \left\langle i\left|H_{SO}\right|j\right\rangle$. With the normalized perturbation wave functions, *Z* and *X* parameters were obtained as 9.079×10^{-4} and 3.380×10^{-4} respectively, which are essentially identical to those in the SOCI model. The maximum value of the expansion coefficients in the third terms in Eq. (2-38) was 2.154×10^{-6}. Namely, the expansion coefficients of the first-order wave function have a possible error in the order of 10^{-6}. Therefore, the *Z* parameter of Pert(Full) is in agreement with that of SOCI only up to 10^{-6} and the second-order term is responsible for about 1% difference in the *Z* parameters calculated by the SOCI and Pert(Full) models. Although the first-order perturbation theory seems appropriate to describe the Herzberg I band system, it may cause some errors for other weaker intensity band systems, in which very small higher-order expansion coefficients are not negligible in the relative magnitude, for example, in the Herzberg II and III band systems.

As for the *M* parameter, almost the same discussions hold as for *Z* and *X*. However, there was a significant difference (10%) between the SOCI and Pert(Full) model for the M_g parameter. It is for this reason that M_g calculated by the SOCI model includes the higher-order coupling terms induced by the SO and RO interaction. The dominant component of this higher-order terms for the M_g parameter is as follows.

$$-B_v \frac{\left\langle X\,^3\Sigma_{1g}^- \left| \mathbf{L}^+ \right| X\,^3\Sigma_{0^+g}^- \right\rangle}{E\left(X\,^3\Sigma_{0^+g}^-\right) - E\left(X\,^3\Sigma_{1g}^-\right)} \left\langle X\,^3\Sigma_{0^+g}^- \left| \boldsymbol{\mu}_- \right| A^3\Sigma_{1u}^+ \right\rangle = 8.715\times10^{-7}. \qquad (2\text{-}39)$$

The $X\,^3\Sigma_g^-$ state splits into the $X\,^3\Sigma_{1g}^-$ and $X\,^3\Sigma_{0^+g}^-$ states due to the second-order SO interaction, and these two states, in the Hund's case (c) representation, are able to couple with each other through the RO interaction. Although the matrix element of the RO interaction was very small (2.011×10^{-8} a.u.), since it should vanish in the Hund's case(a) limit, the energy splitting $E\left(X\,^3\Sigma_{0^+g}^-\right) - E\left(X\,^3\Sigma_{1g}^-\right)$ was also small(2.990×10^{-4} a.u.). Thus, the above transition moment parameter makes a meaningful contribution.

Next, the calculated electronic transition moment parameters are compared with the experimental ones obtained by Mérienne et al. [2.8] and other *ab initio* values of Klotz et al. [2.17] in Figs. 2-2, -3.

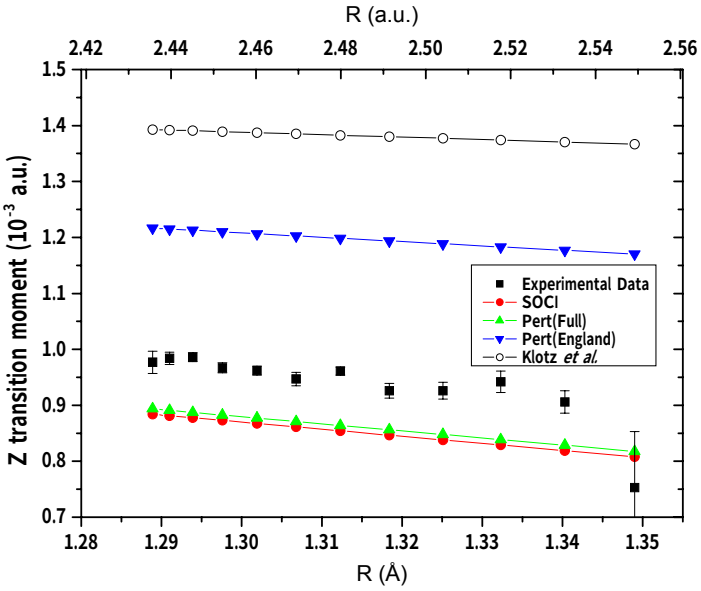

Fig. 2-2 The *Z* parameters calculated by the three models, compared with the values of Mérienne et al.(points) [2.8] and other *ab initio* values of Klotz et al. [2.17] The Pert(England) model gives 20 % larger values compared with the experimental ones. The SOCI and Pert(Full) models give 10 % smaller values.

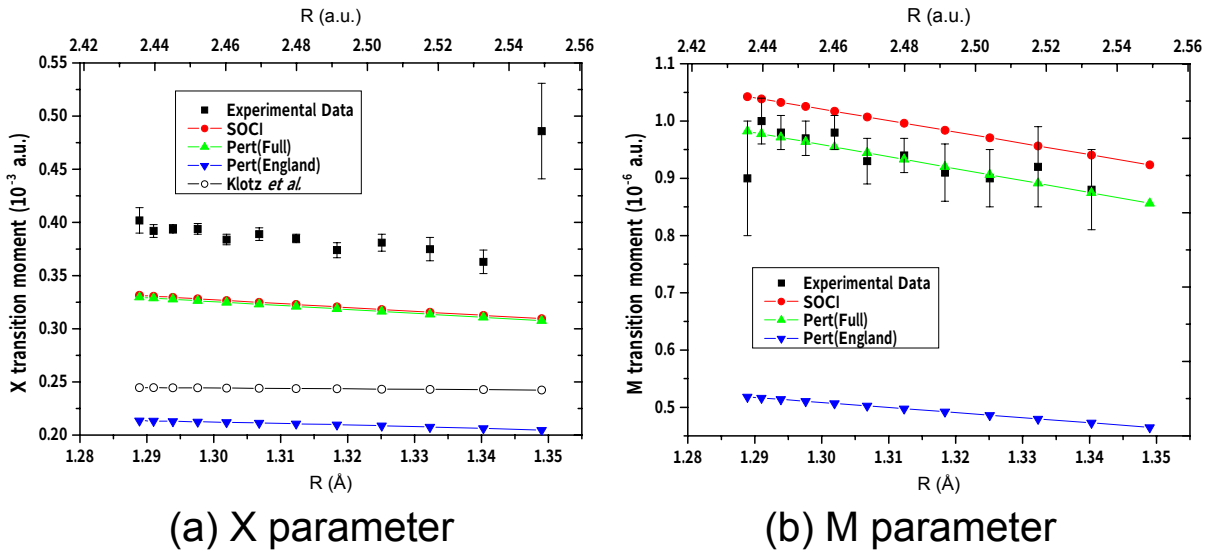

Fig. 2-3 The *X* and *M* parameters calculated by the three models, compared with the values of Mérienne et al.(points) [2.8] and other *ab initio* values of Klotz et al. [2.17]
(a) As for *X*, the Pert(England) model gives 50 % smaller values compared with the experimental ones. The SOCI and Pert(Full) models give 15 % smaller values.
(b) As for *M*, The Pert(England) model gives 50 % smaller values compared with the experimental ones. The SOCI and Pert(Full)models are in good agreement with the experimental ones.

As for the SOCI and Pert(Full) models, though all the three parameters were about 10 % smaller than the experimental estimates, they were still in reasonable agreement. On the other hand, the Pert(England) model did not reproduce the value of Mérienne et al. even qualitatively, namely *Z* was overestimated and *X* and *M* were underestimated.

Klotz et al. calculated *Z* and *X* parameters using a similar model as Pert(England) and their values have a similar tendency as Pert(England). Later, the sensitivities of the rotational and vibronic absorption strengths to these small but meaningful differences in the transition moments will be discussed.

2.4.2. Vibrational Wave Functions

The potential curves of the initial and final states were calculated with the COSOCI method. Table 2-4 lists the calculated and experimental spectroscopic constants R_e, ω_e and D_e for

the *X* and the three Herzberg states [2.35] of the spin-free and COSOCI potential curves.

Table 2–4. Spectroscopic constants for the *X* and the three Herzberg states. The inside in parenthesis is the value from the potential curves including the SO interaction, and the other values are from the Hund's case (a) potential curves.

	R_e (Å)			ω_e (cm^{-1})			D_e (eV)		
	Present	Exp.[a]	Calc.	Present	Exp.[a]	Calc.	Present	Exp.[a]	Calc
$X\,^3\Sigma_g^-$	1.212 (1.212)	1.208	1.213[b]	1554 (1554)	1580	1550[b]	5.263 (5.223)	5.214	5.193[b]
$A^3\Sigma_u^+$	1.522 (1.522)	1.520	1.520[c]	801 (800)	804	802[c]	0.868 (0.849)	0.825	0.830[c]
$c^1\Sigma_u^-$	1.517	1.514	1.518[c]	809	797	790[c]	1.176	1.114	1.112[c]
$A'^3\,\Delta_u$	1.515	1.513	1.513[c]	793	815	819[c]	0.946	0.903	0.906[c]

Note. The inside in parenthesis is the values from the potential curves including the SO interaction, and the other values are from the Hund's case (a) potential curves. ([a] Ref.[2.35], [b] Ref.[2.30], [c] Ref.[2.20])

The values in parenthesis are calculated by the COSOCI method for the $\Omega = 1$ component of the *X* and *A* states. The calculation values are in good agreement with the experimental and other calculational values.

The vibrational wave functions were obtained for the *X* and *A* states with the above potential curves. The results for the *A* state are compared with the experimental values of Jenouvrier et al. [7] and theoretical values of Vroonhovenet al. [20] in Table 2-5.

The present calculation reproduced the experimental values reasonably except for the $v' = 12$ vibrational level. The $v' = 12$ level is the highest level below the dissociation limit, so that a small perturbation gives an enormous change in the vibrational wave function. For instance, the difference between the Hund's case (a) and Hund's case (c) potential curves is rather large in spite of the small SO interaction for the $v' = 12$ level.

Table 2–5. Vibrational energies and rotational constants of the $A^3\Sigma_u^+$ state.

v'	Calc.		Jenouvrier et al.		Vroonhoven et al.	
	T(v')	B(v')	T(v')	B(v')	T(v')	B(v')
0	35078.315 (35059.139)	0.89679 (0.89685)	35008.826	0.90499	———	0.90292
1	35863.750 (35844.646)	0.87196 (0.87206)	35783.323	0.88763	35781.596	0.88492
2	36618.545 (36599.639)	0.84628 (0.84644)	36527.267	0.86923	36523.859	0.86626
3	37340.329 (37321.853)	0.81952 (0.81965)	37238.316	0.84937	37233.201	0.84651
4	38026.405 (38007.903)	0.79133 (0.79128)	37913.628	0.82767	37906.330	0.82479
5	38673.338 (38654.422)	0.76121 (0.76121)	38549.666	0.80359	38539.734	0.80042
6	39276.670 (39258.056)	0.72848 (0.72873)	39141.946	0.77635	39127.706	0.77255
7	39830.955 (39812.808)	0.69219 (0.69230)	39684.676	0.74469	39664.322	0.73985
8	40328.895 (40310.528)	0.65082 (0.65063)	40170.213	0.70661	40141.459	0.70012
9	40760.944 (40741.738)	0.60198 (0.60152)	40588.176	0.65869	40548.585	0.65052
10	41114.441 (41093.869)	0.54178 (0.54072)	40924.334	0.59429	40873.847	0.58578
11	41374.130 (41349.603)	0.46408 (0.45921)	41158.975	0.50470	41105.612	0.50062
12	41529.992 (41489.228)	0.36595 (0.28433)	41265.361	0.16400	41239.710	0.37749

Note. The inside of parenthesis is the value obtained from the potential curves including the SO interaction.

This point was also discussed by Vroonhoven et al. [2.36] Other theoretical values [2.20] were in better agreement with experiment than ours except for the $v'=12$ level. This is because they used larger basis set (aug-cc-pV5Z) and different calculation method. They calculated the potential curves using two methods for different internuclear regions. In the Franck-Condon region, they used the CASSCF+MRCI method, while they constructed the potential curves in an ad-hok manner in the dissociation region. Anyway, both methods reproduced the experimental values reasonably except for $v'=12$ level, therefore the present

potential curves and vibration wave functions were used for the calculation of each absorption strength.

Lastly, the Franck-Condon factor (FCF) between the *X* and *A* states were calculated. Note that in the actual calculation discussed before, the Condon approximation was not used, but the transition moment $M(a,b)$ was directly evaluated with Eq. (2-7). However, it is still interesting to compare the theoretical and experimental FCFs to examine the vibrational wave function with the experiment data.

Table 2–6. Franck–Condon factor (*N*=1) calculated by the SOCI model, compared with experimental data from Ref [2.16].

Band (*v*', *v*)	Calc.	England et al.
0,0	2.086×10^{-4}	
1,0	1.659×10^{-4}	
2,0	6.938×10^{-4}	
3,0	2.027×10^{-4}	
4,0	4.638×10^{-4}	4.309×10^{-4}
5,0	8.845×10^{-4}	8.149×10^{-4}
6,0	1.457×10^{-4}	1.325×10^{-3}
7,0	2.109×10^{-4}	1.889×10^{-3}
8,0	2.706×10^{-4}	2.380×10^{-3}
9,0	3.065×10^{-4}	2.629×10^{-3}
10,0	2.979×10^{-4}	2.449×10^{-3}
11,0	2.258×10^{-4}	
12,0	6.528×10^{-4}	

Note. *v*' and *v* represent the vibrational levels of the $A^3\Sigma_u^+$ and $X^3\Sigma_g^-$ states, respectively.

The difference between the Hund's case (a) and (c) potential curves for the FCF is negligibly small. Then, the rotationless FCF in the SOCI model was compared with the ones of England et al. [2.16] in Table 2-6. The present values were about 10% larger than theirs. Mérienne et al. determined the electronic transition moment parameters using the experimental FCF. If the transition moment $M(a,b)$ is calculated in the SOCI and Pert(Full)

models, as a product of each electronic transition moment parameter and the FCF, the present transition moments are in almost quantitative agreement with the experimental ones because the electronic transition moment parameters and FCF were, respectively 10 % smaller and larger than the experimental ones. However, the Pert(England) model does not reproduce the experimental transition moments, because as described in 2.4.1, the electronic transition moment parameters in that model did not agree with the experimental ones even qualitatively. Direct calculations of the transition moments yielded essentially the same values as the ones using the Condon approximation. Therefore, it is concludes that only the SOCI and Pert(Full) models are able to reproduce the transition moments of Mérienne et al.

2.4.3. Integrated Rotational Line Strength

Table 2–7. Comparison of each calculational intensity and experimental data [2.8] (10^{-26} cm^2 cm^{-1}) of the 13 rotational lines for the N=13 of the (7, 0) band.

Branch	Pert(England)	Pert(Full)	SOCI	Exp.
$^{O}P_{12}$	113.54	30.63	29.28	28.8
$^{O}P_{23}$	79.49	16.89	15.97	14.0
$^{Q}P_{21}$	206.71	159.02	157.32	190
$^{Q}P_{32}$	174.25	150.46	149.27	172
$^{O}Q_{13}$	0.42	0.05	0.08	
$^{Q}Q_{11}$	93.49	228.45	242.85	285
$^{Q}Q_{22}$	19.90	40.27	45.36	42.0
$^{Q}Q_{33}$	6.71	14.41	12.12	27.1
$^{S}Q_{31}$	0.17	1.81	2.00	
$^{Q}R_{12}$	256.33	182.82	180.52	208
$^{Q}R_{23}$	233.13	181.84	179.96	188
$^{S}R_{21}$	77.97	13.99	13.11	12.5
$^{S}R_{32}$	51.13	5.94	5.43	

Note. Going from left to right, the calculational level becomes higher.

With the above electronic transition moment parameters, potential curves, and the formulae

of Bellary et al., the integrated rotational line absorption cross sections of the 13 rotational branches were calculated for each vibrational band. Three calculational results of N=13 in the v'=7 vibrational band were shown in Table 2-7.

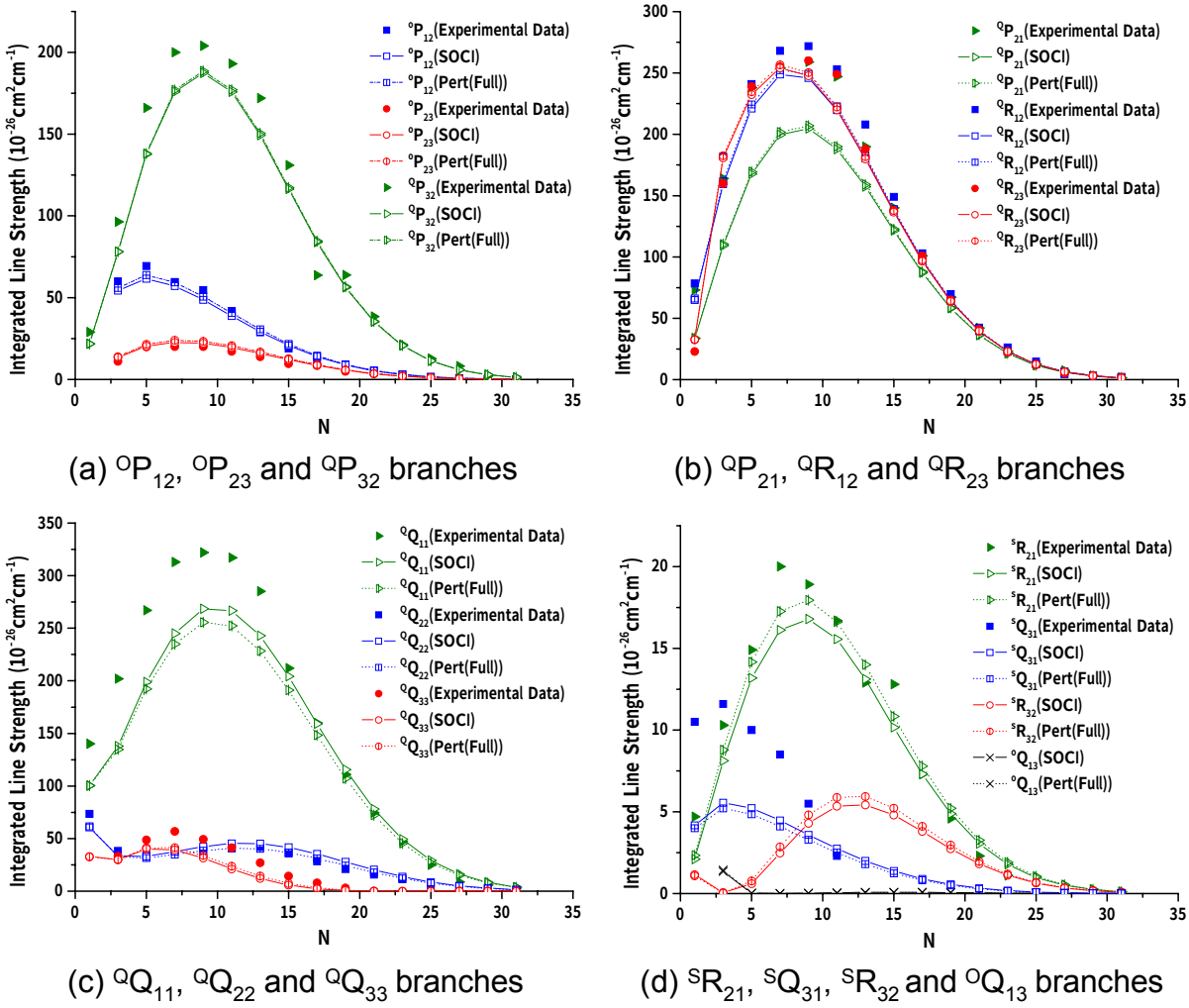

Fig. 2-4 Comparison of the calculated line strengths of the SOCI and Pert(Full) models with the experimental data of Mérienne et al.(points) for the (7,0) band. [2.8] The solid and dash lines represent the calculational values obtained by the SOCI and Pert(Full) model, respectively. (a) $^{O}P_{12}$, $^{O}P_{23}$ and $^{Q}P_{32}$ branches, (b) $^{Q}P_{21}$, $^{Q}R_{12}$ and $^{Q}R_{23}$ branches (c) $^{Q}Q_{11}$, $^{Q}Q_{22}$ and $^{Q}Q_{33}$ branches, (d) $^{S}R_{21}$, $^{S}Q_{31}$, $^{S}R_{32}$ and $^{O}Q_{13}$ branches. For $^{S}R_{32}$ and $^{O}Q_{13}$ branches, only calculated values are showed.

Clearly, the SOCI and Pert(Full) models give better results than the Pert(England) model, for example, for the $^{O}P_{12}$, $^{O}P_{23}$, $^{Q}Q_{11}$, $^{Q}Q_{22}$, $^{Q}Q_{33}$ and $^{S}R_{21}$ branches. The Pert(England) model cannot reproduce the experimental results very well. On the other hand, the SOCI and Pert(Full) models give the almost quantitative results for most branches. The

transition moments of Klotz et al. gave the similar results as Pert(England). Therefore, their transition moments are not appropriate for the calculation of the integrated rotational line strengths.

Next, the calculated and experimental integrated rotational line strengths with various *N* in the SOCI and Pert(Full) models are shown in Fig. 2-4, and those of Pert(England) in Fig. 2-5.

With various *N*, a similar conclusion for the three models can be obtained. That is, only the SOCI and Pert(Full) models are able to reproduce the experimental results quantitatively. In comparison of the SOCI and Pert(Full) models, it is noticed that the SOCI model is slightly better than Pert(Full), for example, for the $^{Q}Q_{11}$, $^{Q}Q_{22}$ and $^{S}R_{21}$ branches. The calculation can give very weak line strengths, for the $^{S}Q_{31}$, $^{O}Q_{13}$ and $^{S}R_{32}$ branches, and these very small values are consistent with the fact that they were not observed experimentally. In this thesis, the author have discussed only the rotational branches of the (7-0) band, however, a similar tendency for other bands was obtained as well.

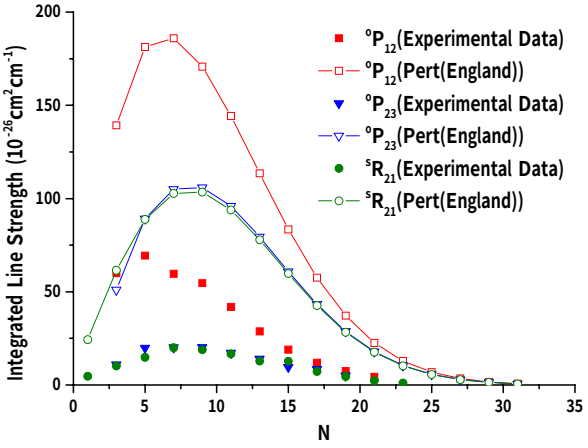

Fig. 2-5 Comparison of the $^{O}P_{12}$, $^{O}P_{23}$ and $^{S}R_{21}$ line strengths calculated by the Pert(England) model with the experimental data of Mérienne et al.(points) for the (7,0) band. [2.8] The solid lines represent the calculational values obtained by the Pert(England).

Table 2–8. Calculational intensity (10^{-26}cm^{2}cm^{-1}) of 13 rotational lines for N=13 of the (7,0) band obtained by two sets of parameters compared with experimental ones. [2.8]

Branch	SOCI	Model 1	Model 2	Exp.
$^{O}P_{12}$	29.28	31.25	29.28	28.8
$^{O}P_{23}$	15.97	16.93	15.97	14.0
$^{Q}P_{21}$	157.32	159.77	157.32	190
$^{Q}P_{32}$	149.27	143.73	149.27	172
$^{O}Q_{13}$	0.08	0.00	5.75	
$^{Q}Q_{11}$	242.85	232.10	169.54	285
$^{Q}Q_{22}$	45.36	40.27	45.36	42.0
$^{Q}Q_{33}$	12.12	13.59	40.30	27.1
$^{S}Q_{31}$	2.00	2.83	3.65	
$^{Q}R_{12}$	180.52	186.22	180.52	208
$^{Q}R_{23}$	179.96	188.21	179.96	188
$^{S}R_{21}$	13.11	12.34	13.11	12.5
$^{S}R_{32}$	5.43	4.46	5.43	

Note. SOCI used the relation as Z,X=Y,M_1=M_2=M_{ef}=M_{fe},N_e=N_f=ζ_0=ζ_1=η_0=η_1=0. Model 1 calculated each rotational line with the 13 independent parameter set Z, X, Y, M_1, M_2, M_{ef}, M_{fe}, N_e, N_f, ζ_0, ζ_1, η_0 and η_1. Model 2 used only Z and X parameters and omitted M in SOCI.

As mentioned before, strictly speaking, the SOCI model needs 13 independent parameters instead of just three. These were termed as Z, X, Y, M_1, M_2, M_{ef}, M_{fe}, N_e, N_f, ζ_0, ζ_1, η_0 and η_1 by Bellary et al. [2.13] For example, X and Y parameters are written as follows.

$$X = \left\langle A^3\Sigma_{1u}^{+} \middle| \mu_{+} \middle| X^3\Sigma_{0^+g}^{-} \right\rangle, \qquad (2\text{-}40)$$

$$Y = \left\langle A^3\Sigma_{0^-u}^{+} \middle| \mu_{+} \middle| X^3\Sigma_{1g}^{-} \right\rangle, \qquad (2\text{-}41)$$

In general, X cannot be equal to Y, with a finite strength of the SO interaction. Treating these 13 parameters independently, the author calculated the integrated rotational line strengths for N=13 of the (7,0) band (Model 1), and compared with the previous SOCI results obtained with the three parameters in Table 2-8. Moreover, to investigate the effect of the RO interaction, the M parameter was omitted in the SOCI model (Model 2).

As for the lines of strong intensity, differences between the Model 1 and SOCI were about

3% or less. Although small differences can be seen in the weak intensity lines of the ${}^{O}Q_{13}$, ${}^{S}Q_{31}$ and ${}^{S}R_{32}$ branches, the overall intensity did not change very much. With altering the rotational and vibrational levels, this tendency did not change.

Therefore, it is concluded that in practice only three electronic parameters are enough to calculate the integrated rotational line strengths in the SOCI model. Of course, this conclusion can apply to the Pert(Full) and Pert(England) model. Next, comparing Model 2 and SOCI, it is found that some Q lines of the ${}^{O}Q_{13}$, ${}^{Q}Q_{11}$, ${}^{Q}Q_{33}$ and ${}^{S}Q_{31}$ branches of Model 2 are different from those of SOCI very much. These results are consistent with the conclusion of Huestis et al. [2.14] Therefore, we cannot neglect the RO interaction at all.

So far, we have seen that the SOCI and Pert(Full) models can reproduce the integrated rotational line strengths. In contrast, the Pert(England) model cannot reproduce them even qualitatively. To refer to Eq. (2-7), we can ascertain that the difference of the calculational results is due to the electronic transition moment parameters, because the calculated FCFs were not sensitive to the theoretical models. In the SOCI and Pert(Full) models, the electronic transition moment parameters were in good agreement with the experimental ones. On the other hand, the Pert(England) model calculated each electronic transition moment parameter only roughly, and it did not yield even the relative ratio of the individual parameters correctly. It has also been showed that the cause of the difference among the three models is the degrees of configuration interactions with the highly excited states induced by the SO and RO interactions. Hence, it is concluded that *each rotational line strength is strongly sensitive to the accuracy of each electronic transition moment parameter, and only the higher level calculational models including the configuration interactions with highly excited states reproduce the absolute values of each parameter.* However, in the next section, it will be shown that the results of vibronic oscillator strengths do not depend on the calculational level

very much.

2.4.4. Vibronic Oscillator Strength

Table 2-9 shows the vibronic oscillator strengths of the ($v' = 0 - 12, \quad v = 0$) bands using the three models.

The SOCI and Pert(Full) models reproduced the experimental values very well, and Pert(England) models also give reasonable results. Why can we calculate each vibrational oscillator strength fairly well with any model ?

Table 2–9. Vibronic oscillator strength from the Pert(England), Pert(Full) and SOCI models compared with the experimental data from Ref [2.8].

Band (v', v)	Pert(England)	Pert(Full)	SOCI	Exp.
0,0	1.144×10^{-14}	8.125×10^{-14}	8.078×10^{-14}	8.36×10^{-14}
1,0	9.416×10^{-13}	6.767×10^{-13}	6.734×10^{-13}	8.02×10^{-13}
2,0	4.063×10^{-12}	2.954×10^{-12}	2.941×10^{-12}	3.73×10^{-12}
3,0	1.222×10^{-11}	8.987×10^{-11}	8.954×10^{-11}	1.11×10^{-11}
4,0	2.874×10^{-11}	2.133×10^{-11}	2.127×10^{-11}	2.51×10^{-11}
5,0	5.618×10^{-11}	4.210×10^{-11}	4.199×10^{-11}	5.09×10^{-11}
6,0	9.470×10^{-11}	7.155×10^{-11}	7.141×10^{-11}	8.36×10^{-11}
7,0	1.399×10^{-10}	1.065×10^{-10}	1.063×10^{-10}	1.22×10^{-10}
8,0	1.828×10^{-10}	1.401×10^{-10}	1.399×10^{-10}	1.57×10^{-10}
9,0	2.103×10^{-10}	1.621×10^{-10}	1.619×10^{-10}	1.79×10^{-10}
10,0	2.070×10^{-10}	1.602×10^{-10}	1.601×10^{-10}	1.64×10^{-10}
11,0	1.583×10^{-10}	1.229×10^{-10}	1.229×10^{-10}	9.15×10^{-11}
12,0	4.599×10^{-11}	3.578×10^{-11}	3.578×10^{-11}	

Note that the three models give similar results unlike the integrated rotational line strengths.

Buijsse et al. expressed the effective electronic transition moment of the vibronic transition for a give J,

$$M_{\text{eff}}^2 = \left(Z^2 + 4X^2 - 4M^2 + 6M^2 J(J+1)\right)/3, \qquad (2\text{-}42)$$

and applied this M_{eff}^2 to the expression of the vibronic oscillator strength,

$$f_{v'v} = \frac{8\pi^2 m_e c}{3he^2} \upsilon_{v'v} M_{\text{eff}}^2 , \qquad (2\text{-}43)$$

Here, $q_{v'v}$ is the FCF. Using this approximate expression, we are able to focus on the only electronic transition moment parameter in analyzing the model independent vibronic oscillator strength, because $\upsilon_{v'v}$ and $q_{v'v}$ did not depend on the three models very much.

M_{eff}^2 was evaluated for J=11 which is appropriate for the room temperature conditions. Fig. 2-6 shows that M_{eff} calculated by Pert(England) is in accidental agreement with the value of Mérienne et al., because in this model, Z was overestimated and X and M were underestimated from their value as explained in Section 2.4.1, showing an error cancellation.

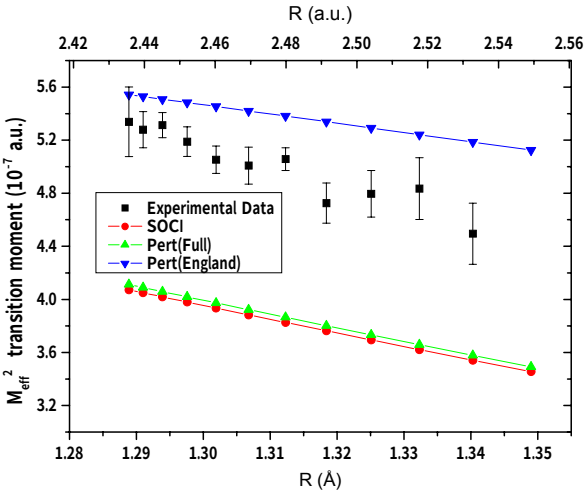

Fig. 2-6 Effective electronic transition moment M_{eff}^2 calculated by the three models, compared with the values of Mérienne et al.[2.8] The Pert(England) model shows accidental agreement.

Therefore, we can obtain the reasonable results only for the vibronic oscillator strengths. On the other hand, the SOCI and Pert(Full) models underestimated the value of Mérienne et al. In view of the fact that our FCF is 10% larger than the experimental one, the above M_{eff} in the SOCI and Pert(Full) models are in quantitative agreement with the experiment. Therefore, all of the three models can reproduce the vibrational oscillator strength reasonably.

2.4.5. Anisotropy Parameter in Photodissociation Processes

Using the new transition moment parameters, an anisotropy parameter β was simply estimated for the photodissociation products from the Herzberg continuum. [2.4,6,9] Considering the experimental conditions, the vibration state of $X^3\Sigma_g^-$ was supposed in the ground state and the rotational motions were neglected. Moreover, in the axial recoil limit, the anisotropy parameter β is simply written as follows. [2.37]

$$\beta = \frac{-4X^2 + 2Z^2}{4X^2 + Z^2}. \qquad (2\text{-}44)$$

β was calculated with the new transition moment parameters and shown in Table 2-10 along with experimental values of Tonokura et al. [2.4], Buijsse et al. [2.6] and Alexander et al. [2.9], as well as another *ab initio* value calculated from the transition moment parameters of Klotz et al. [2.17]

Table 2–10. Anisotropy parameter from the Pert(England), Pert(Full) and SOCI models compared with the *ab initio* value of Klotz *et al.* in Ref [2.17], and the experimental data in Ref [2.4,6,9].

Pert(England)	Pert(Full)	SOCI	Klotz	Tonokura[b]	Buijsse[c]	Alexander[d]
1.672	0.942	0.930 (0.900)[a]	1.711	1.6±0.4	0.612±0.065	0.55±0.10($^3P_{2,1}$)

[a]The value including the contribution from the Herzberg II and III transitions.
[b]Ref [2.4] at 226 nm.
[c]Ref [2.6] at 226nm.
[d]Ref [2.9] at 222nm. The value is obtained from the $^3P_2$ and $^3P_1$ products.

Clearly, Pert(Full) and SOCI results are in good agreement with the recent experimental data of Buijsse et al. and Alexander et al. On the other hand, the values derived with the electronic transition moment parameters by Pert(England) and Klotz et al. are significantly different from the recent experiments, instead they are in agreement with that of Tonokura et al. As was seen before, the Pert(England) model cannot yield the accurate electronic transition

moment parameters, so its β value is not reliable. In this calculation, the dissociation is assumed to take place only from the Herzberg I transition. However, the experiments also contain a small contribution of the photoproducts from the Herzberg II and III transitions whose transition moments are dominated by perpendicular components. [2.6] With the SOCI model, the β value was also calculated, and some improvement was obtained toward the recent experimental values. Therefore, this work supports the anisotropy parameter of Buijsse et al. and Alexander et al. Possible reason for the difference in their experimental results was discussed in Ref [2.6]. In this section, an accuracy of the SOCI and Pert(Full) model is also confirmed by the calculation of the anisotropy parameter.

2.5. Conclusion

The author employed three theoretical models, SOCI, Pert(Full) and Pert(England), to calculate the electric-dipole forbidden transition moment of the Herzberg I band system. Comparing the calculational and experimental transition moments, the author found that SOCI and Pert(Full) are able to calculate them quantitatively, on the other hand, Pert(England) cannot yield them even qualitatively. The difference between the SOCI and Pert(Full) models was small, so that the SO interaction can be essentially represented by the first-order perturbation theory. Although the second-order interactions between the SO and RO couplings were also calculated by the SOCI model, it turned out to be less important. Namely, either the variation or first-order perturbation theory is applicable to the calculation of the electric transition moment, as long as all the configuration interactions with highly-excited stated induced by the SO and RO interactions are included. On the other hand, a limited first-order perturbation theory as Pert(England) in which the initial and final wave

functions are truncated by only one perturbing state as $1^3\Pi_g$ and $B^3\Sigma_u^-$ is not appropriate for the quantitative calculation. Moreover, even if the contributions of other low-lying states was included in the sum-over-states representation as in Pert(3) and Pert(10), they converged to Pert(Full) very slowly in spite of the weak SO perturbations of the oxygen molecule. Therefore, it is concluded that the basis set truncations easily lead to erroneous results for weak forbidden band systems such as the Herzberg I band system.

To confirm an accuracy of the current transition moments, the author calculated the integrated rotational line strengths and vibronic oscillator strengths of the Herzberg I band system with the SOCI, Pert(Full) and Pert(England) models. The SOCI and Pert(Full) models gave reasonable results for both strengths, while the Pert(England) model reproduced only the vibronic oscillator strength due to an error cancellation. Thus, the SOCI and Pert(Full) models which include all the possible configuration interactions with highly excited states through some perturbations are necessary to calculate very weak absorption strengths quantitatively.

The author also calculated the anisotropy parameter in the photodissociation from the Herzberg I band and obtained reasonable agreement with recent experimental data of Buijsse et al. and Alexander et al. in the SOCI and Pert(Full) model.

Configurational analysis shows that the slow convergence in the sum-over-states representations in Tables 2-1, -2, and -3 originates from the fact that the oxygen molecule has some lower-lying unoccupied valence orbitals, π_g and σ_u. For example, the wave function of the ground state is represented using the MR-SDCI(cc-pVQZ) method as follows.

$$\left|X\right\rangle \cong 0.9381\left|\cdots\sigma_g^2\pi_u^4\pi_g^2\right\rangle - 0.1307\left|\cdots\sigma_g^2\pi_u^2\pi_g^4\right\rangle. \qquad (2\text{-}45)$$

The first term cannot couple with highly excited states through the SO or RO interactions which consist of the one-electron operators, because most of the highly excited states are expressed by the configurations in which two or more electrons are excited from the first term

in Eq. (2-45). On the other hand, the second term makes it possible to couple with the highly excited states directly and induces the complicated configuration mixings through even small perturbations. Since the Herzberg I band system is a weak absorption band system, these interactions cannot be neglected by any means.

Reference

[2.1] D.H. Parker, Acc. Chem. Res. 33 (2000) 563.

[2.2] K. Yoshino, J.E. Murray, J.R. Esmond, Y. Sun, W.H. Parkinson, A.P. Thone, R.C.M. Learner, G. Cox, Can. J. Phys. 72 (1994) 1101.

[2.3] K. Yoshino, J.R. Esmond, J.E. Murray, W.H. Parkinson, A.P. Thorne, R.C.M. Learner, G. Cox, J. Chem. Phys. 103 (1995) 1243.

[2.4] K. Tonokura, N. Shafer, Y. Matsumi, M. Kawasaki, J. Chem. Phys. 95 (1991) 3394.

[2.5] D.J. Leahy, D.L. Osborn, D.R. Cyr, D.M. Neumark, J. Chem. Phys. 103 (1995) 2495.

[2.6] B. Buijsse, W.J. van der Zande, A.T.J.B. Eppink, D.H. Parker, B.R. Lewis, S.T. Gibson, J. Chem. Phys. 108 (1998) 7229.

[2.7] A. Jenouvrier, M.-F. Mérienne, B. Coquart, M. Carleer, S. Fally, A.C. Vandaele, C. Hermans, R. Colin, J. Mol. Spectrosc. 198 (1999) 136.

[2.8] M.-F. Mérienne, A. Jenouvrier, B. Coquart, M. Carleer, S. Fally, R. Colin, A.C. Vandaele, C. Hermans, J. Mol. Spectrosc. 202 (2000) 171.

[2.9] A.J. Alexander, Z.H. Kim, R.N. Zare, J. Chem. Phys. 118 (2003) 10566.

[2.10] H. Lefebvre-Brion, R.W. Field, Perturbations in the Spectra of Diatomic Molecules. Academic Press, Orlando. (1986)

[2.11] G. Herzberg, Spectra of Diatomic Molecules. Van Nostrand-Reinhold, Princeton, New Jersey. (1950)

[2.12] B.R. Lewis, S.T. Gibson, Can. J. Phys. 68 (1990) 231.

[2.13] V.P. Bellary, T.K. Balasubramanian, J. Quant. Spectrosc. Radiat. Transfer. 45 (1991) 283.

[2.14] D.L. Huestis, R.A. Copeland, K. Knutsen, T.G. Slanger, R.T. Jongma, M.G.H. Boogaarts, G. Meijer, Can. J. Phys. 72 (1994) 1109.

[2.15] J.B. Tatum, J.K.G. Watson, Can. J. Phys. 49 (1971) 2693.

[2.16] J.P. England, B.R. Lewis, S.T. Gibson, Can. J. Phys. 74 (1996) 185.

[2.17] R. Klotz, S.D. Peyerimhoff, Mol. Phys. 57 (1986) 573.

[2.18] B.F. Minaev, Chem. Phys. 252 (2000) 25.

[2.19] B.F. Minaev, L.G. Telyatnik, Optics and Spectroscopy. 91 (2001) 883.

[2.20] M.C.G.N. van Vroonhoven, G.C. Groenenboom, J. Chem. Phys. 116 (2002) 1954.

[2.21] M.C.G.N. van Vroonhoven, G.C. Groenenboom, J. Chem. Phys. 116 (2002) 1965.

[2.22] E.E. Whiting, R.W. Nicholls, Astropys. J. Suppl. 27 (1974) 1.

[2.23] A.S.-C. Cheung, K. Yoshino, W.H. Parkinson, D.E. Freeman, J. Mol. Spectrosc. 119 (1986) 1.

[2.24] C. Amiot, J. Verges, Can. J. Phys. 59 (1981) 1391.

[2.25] R. Shepard, I. Shavitt, R.M. Pitzer, D.C. Comeau, M. Pepper, H. Lischka, P.G. Szaley, R. Ahlrichs, F.B. Brown, J.-G. Zhao, Int. J. Quan. Chem. Symp. 22 (1988) 149.

[2.26] K. Morokuma, K. Yamashita, S. Yabushita, in: A.Laganà (Ed.), Supercomputer Algorithms for Reactivity, Dynamics and Kinetics of Small Molecules, Kluwer, Dordrecht, (1989) 37.

[2.27] S. Yabushita, Z. Zhang, R.M. Pitzer, J. Phys. Chem. A 103 (1999) 5791.

[2.28] T.H. Dunning, Jr., J. Chem. Phys. 90 (1989) 1007.

[2.29] J.A. Pople, R. Krishnan, H.B. Schlegel, J.S. Binkley, Int. J. Quantum. Chem. Symp. 13 (1979) 225.

[2.30] H. Partridge, C.W. Bauschlicher, Jr., S.R. Langhoff, P.R. Taylor, J. Chem. Phys. 95 (1991) 8292.

[2.31] E.A. McCullough, Jr., R.E. Wyatt, J. Chem. Phys. 54 (1971) 3578.

[2.32] C. Cerjan, K.C. Kulander, Comput. Phys. Commun. 63 (1991) 529.

[2.33] M. Sugawara, M. Kato, Y. Fujimura, Chem. Phys. Lett. 184 (1991) 203.

[2.34] K. Takahashi, M. Sugawara, S. Yabushita, J. Phys. Chem. A. 106 (2002) 2676.

[2.35] T.G. Slanger, P.C. Cosby, J. Phys. Chem. 92 (1988) 267.

[2.36] M.C.G.N. van Vroonhoven, G.C. Groenenboom, J. Chem. Phys. 117 (2002) 5240.

[2.37] R.N. Zare, Mol. Phtochem. 4 (1972)

Chapter 3.

Geometric and

Electronic Structures of $Eu_n(C_8H_8)_n^-$

Abstract

Nakajima and co-workers have measured the photoelectron spectra of the multiple-decker 1:1 sandwich clusters of $Eu_n(COT)_n^-$ (n=1-4; COT=1,3,5,7-cyclooctatetraene), synthesized in the gas-phase. The author studied theoretically the bonding scheme, charge distribution, valence orbital energies and photodetachment energies. He calculated the ground electronic state X^- and the first excited electronic state A^-, both of which have strong ionic bonding and characteristic charge distribution. Moreover, the valence orbital energies of Eu (6s) and COT (L_δ) were found to depend strongly on cluster size and their positions in the clusters. With the calculated vertical detachment energies for these valence orbitals, the peaks in the experimental photoelectron spectra were assigned, and the origin of their interesting behavior was analyzed by employing simple point charge models. From these analyses, it became clear that the characteristic behavior of the spectra is due to the strong ionic bonding and the charge distribution. In addition, using the point charge models, the vertical detachment energies of the one-dimensional polymer $[Eu(COT)]_\infty^-$ were estimated.

3.1. Introduction

The advent of the laser vaporization synthesis method in the 80's [3.1-3] and the successive development of the technique during the last ten years [3.4,5] have enabled us to generate various kinds of novel clusters without environmental factors such as oxidation or reduction of the products. Moreover, considerable experimental and theoretical efforts have recently revealed their characteristic physical and chemical properties, which have been anticipated for the application to new nanostructured materials. In this regard, Nakajima and co-workers have reported the preparation of multiple-decker sandwich clusters, in which metal atoms and organic ligands are alternately stacked one-dimensionally. [3.5] Typical examples for the sandwich clusters are combinations of vanadium (V) atoms and benzene (Bz) molecules and those of lanthanide (Ln) atoms and cyclooctatetraene (COT) molecules.

In the case of the V-Bz sandwich clusters, many experimental and theoretical studies in the last decade have clarified their geometric and electronic structures. [3.6-13] For instance, Yasuike et al. and Miyajima et al. have studied the bonding scheme and ionization energies both experimentally and theoretically, and have made it clear that $V_n(Bz)_{n+1}$ have covalent bonding due to the charge transfer interaction between the benzene LUMOs and the d_δ orbitals of V. This builds up the one-dimensional quasi-band structure. [3.6-8] Following these earlier studies, Pandey and co-workers performed DFT calculations for the neutral and anion V-Bz clusters, and obtained the electron affinities, ionization energies, and ground state spin multiplicities. [3.9,10] Broyer and co-workers determined the permanent dipole moment of $V(Bz)_2$ and V(Bz) using molecular beam deflection experiments in an inhomogeneous electric field and theoretical calculations. [3.11,12] They reported that the $V(Bz)_2$ sandwich cluster has no dipole moment because of its symmetrical structure. They also reported that the one-end open sandwich cluster of V(Bz), somewhat curiously, has negligible dipole moment.

It is reasonable, however, if the dominantly prepared stable structure is weakly bound by a long-range van der Waals force and thus has no charge polarization in the cluster. Recently, Miyajima et al. measured the magnetic moments of $V_n(Bz)_{n+1}$ by a molecular beam magnetic deflection method with a Stern-Gerlach magnet and found a monotonic increase of the magnetic moment with the cluster size. [3.13]

Over the past half a century, a lot of studies have been conducted in the condensed phase organometallic chemistry with rare earth metals, as reviewed, for example, by Schumann et al. [3.14] Particularly, the complex of Ln and COT was firstly isolated by Hayes and Thomas in 1969. [3.15] Since then, there have been many studies of their synthesis, [3.16-19] geometric structure and chemical properties. [3.19-24] Their bonding scheme has been recognized as fairly ionic and their maximum size has been reported as several layers. On the other hand, there have been only a limited number of theoretical works concerning Ln-COT complexes. Dolg and co-workers investigated the geometric and electronic structures of the $Ln(COT)_2$ (Ln=Ce, Nd, Tb, and Yb), which are the smallest unit of $Ln_n(COT)_m$ sandwich clusters. [3.25-28] They reported that $Ln(COT)_2$ have D_{8h} symmetry and, as a first approximation, consist of Ln^{3+} positive central metal ions pinched with two $COT^{1.5-}$ rings.

It is only recently that gas phase experimental works have been performed on Ln-COT complexes with the laser vaporization synthesis method. Kurikawa et al. measured the electron binding energies and the ionization energies of larger $Ln_n(COT)_m$ (Ln=Ce, Nd, Eu, Ho, Er, and Yb) with photoelectron spectroscopy. [3.29,30] Based on the experimental results and the theoretically predicted charge distribution of $Ln(COT)_2$, they suggested that the $Ln_n(COT)_m$ sandwich clusters also have a strong ionic bonding owing to the electron transfer from Ln to COT. Miyajima et al. also discussed the charge distribution of Ln-COT clusters by a chemical probe method with Na atoms as electron donors. [3.31] Recently, Hosoya et al. has

succeeded in synthesizing larger Eu-COT sandwich clusters, named as sandwich nanowires, in the gas phase using a combination of laser vaporization techniques and molecular beam methods. [3.32] In contrast to $V_n(Bz)_m$, which was limited to seven layers, Eu-COT sandwich nanowires were formed with up to one-dimensional 27 layers (about 10 nm overall length) which stimulated theoretical investigation.

In this Chapter, the author reports a theoretical study on the geometric and electronic structures of one-end open 1:1 sandwich clusters of $En_n(COT)_n^-$ (n=1-4), because they are considered to be important intermediates in the sequential formation step of the larger Eu-COT sandwich nanowires and their photoelectron spectra show a characteristic dependence on the cluster size. [3.32] In addition, such a study is essential to understand the properties of the larger cluster and other $Ln_n(COT)_m$ compounds.

In Section 3.2, computational details are given. In Section 3.3, the author first presents the experimental photoelectron spectra which show interesting cluster size dependencies. Next, the author theoretically gives optimized geometries and their charge distribution for two different electronic states, and discusses the characteristic behavior of valence orbital energies of the Eu and COT portions which exhibit strong dependency on the cluster size and the relative positions. The experimental photoelectron spectra are assigned in comparison with the DFT calculations and also with the spectra of barium(Ba)-COT. Furthermore, the physical origin of the characteristic behavior of the valence orbital energies is revealed with simple point charge models. Using the point charge models, the vertical detachment energies (VDE) of the one-dimensional polymer $[Eu(COT)]_\infty^-$ are easily estimated. Finally, one-dimensional potential curves are depicted, based on the linear synchronous transit (LST) paths [3.33] to investigate the energetic relations among the anion and neutral clusters.

3.2. Computational Method

All the DFT calculations were carried out with the B3LYP functionals [3.34] built in the Gaussian 98 program package. [3.35] Throughout this paper, bond lengths are given in angstrom (Å), and energies in eV. A molecular axis (z-axis) is defined as a line passing through Eu and the center of gravity of the COT ligand. The eight π molecular orbitals on a COT ligand are denoted, based on their symmetries, as nondegenerate L_σ, doubly degenerate L_π, L_δ, L_ϕ, and nondegenerate L_γ, therefore the valence electronic configurations of COT^{2-} and COT^- are $L_\sigma^2L_\pi^4L_\delta^4$ and $L_\sigma^2L_\pi^4L_\delta^3$, respectively. The geometric structure of the aromatic ground state COT^{2-} is D_{8h}. For COT^-, several isomeric structures with symmetries of D_{4h} and D_{8h}, have been reported. [3.36,37] Valence electronic configurations of the ground states of Eu^{2+}, Eu^+ and Eu are $4f^7$, $4f^76s^1$, $4f^76s^2$, respectively, in which the 4f electrons always have a half-filled shell structure with a core-like character.

As reported previously, [3.29,30] the charge distribution for the Eu-COT clusters consists of Eu^{2+} cations and COT^{2-} anions. Based on the above mentioned configurations of Eu, which have a core-like character of $4f^7$, and the charge distribution model of $Eu_n(COT)_n$, three different combinations of basis sets and ECPs were applied: 4f CORE-A, 4f CORE-B, and 4f VALENCE. In 4f CORE-A, the 4f core ECP and (7s6p5d)/[5s4p3d] basis set of the Stuttgart/Cologne group [3.38] for Eu and the D95 basis set [3.39] for COT were chosen. In 4f CORE-B, to see the effect of polarization and diffuse functions for COT^{2-}, the D95 basis was replaced by the 6-31+G(d) basis set [3.40]. In 4f VALENCE, the 4f valence ECP and (12s11p10d8f)/[5s5p4d3f] basis set of the Stuttgart/Cologne group were employed for Eu [3.38] and 6-31+G(d) for COT.

3.3. Results and Discussions

3.3.1. Photoelectron Spectra

Hosoya et al. have measured photoelectron spectra of $Eu_n(COT)_n^-$ (n=1-4) to gain detailed information about their electronic structure.

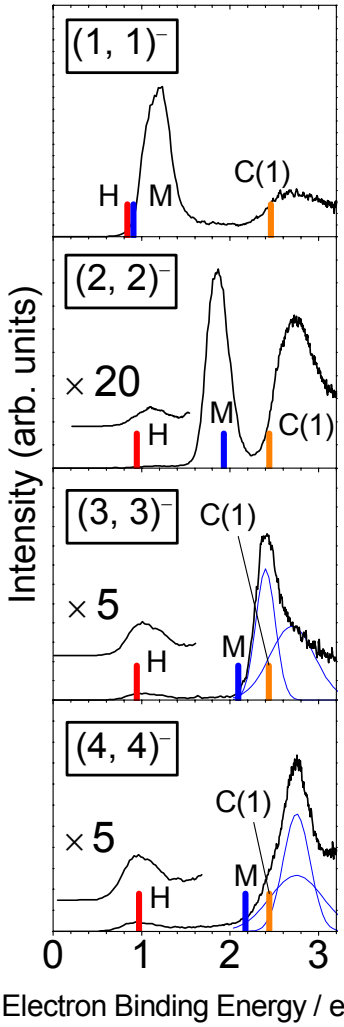

Fig. 3-1 Experimental photoelectron spectra for $(n, n)^-$ (n=1-4) at the photon energy of 355nm (3.49eV) and calculation results with ΔDFT shown by vertical lines. Symbols M and C(1) represent the M and C(1) peaks from the X^- state, and symbol H denotes the H peak from the A^- state as described in section 4.3. The M peak shifts to the higher energy side with the cluster size, and the C(1) and H peaks are almost independent of the cluster size.

Fig. 3-1 and 3-2 show the spectra with the third harmonic (355 nm; 3.49 eV) and the fifth

harmonic (213 nm; 5.83 eV) of a Nd^{3+}: YAG laser, respectively. In the spectra, the horizontal axis corresponds to the electron binding energy, E_b, defined as $E_b = h\nu - E_k$ where E_k is the kinetic energy of the photoelectron.

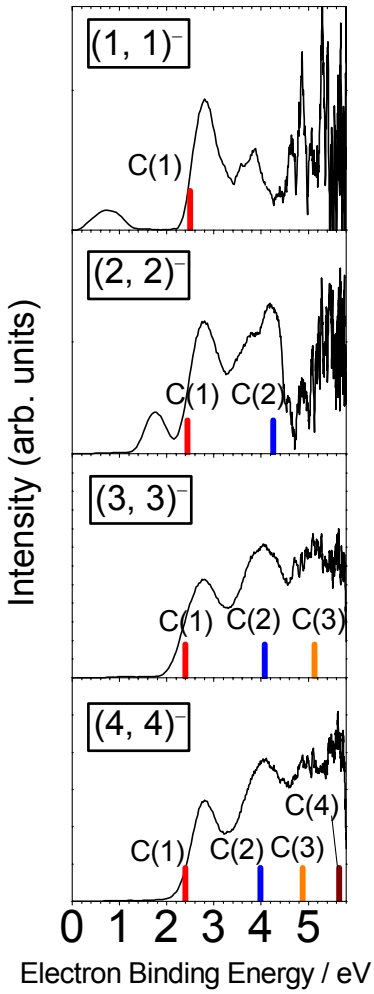

Fig. 3-2 Experimental photoelectron spectra for (n, n)$^-$ (n=1-4) at the photon energy of 213nm (5.83eV) and calculation results with vertical lines, which are obtained by Koopmans' theorem with the UHF orbital energies. Symbol C(i) stands for the detachment from each COT(i) in the X^- state as described in section 4.3. The number of C(i) peaks increases according with the cluster size.

In Fig. 3-1, two significant peaks are found: the first one shifts to the higher energy side with the cluster size (M peak) and the second one is almost independent of the cluster size (C(1) peak). In the spectra of $n \geq 2$, the weak hot band is also observed around the binding energy of 1.0 eV (H peak). In Fig. 3-2, successive peaks are observed where the number of

peaks increases according with the cluster size (C(*i*) peak).

To assign the photoelectron spectra and explain the physical origin of their characteristics, the theoretical studies on geometric and electronic structures of $Eu_n(COT)_n^-$ will be discussed in the following sections.

3.3.2. Optimized Geometry,

Charge Distribution and Localized Molecular Orbitals

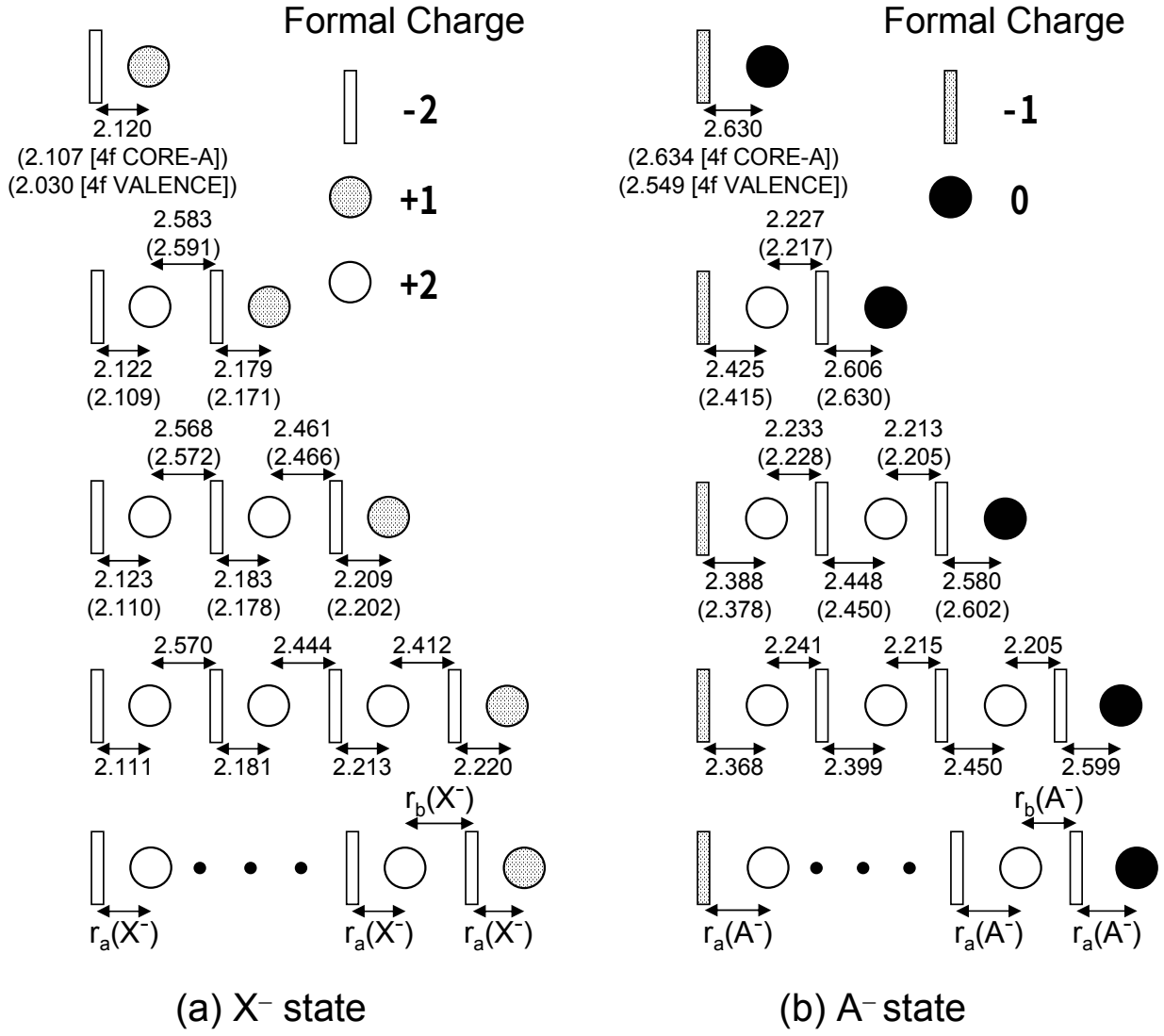

Fig. 3-3 Formal charge distribution and optimized geometry parameters (Å) for the X^- and A^- electronic states of $(n, n)^-$ (n=1-4) calculated by three different treatments. For n=1-3, the optimized parameters of 4*f* CORE-A and -B are shown and inside of parenthesis are the parameters of 4*f* CORE-A. For n=4, optimization was carried out only with the 4*f* CORE-A. For the X^- and A^- states of n=1, optimized parameter calculated by 4*f* VALENCE are also shown. The black, dotted and white circles denote neutral, +1 and +2 charged metals, and dotted and white plates denote −1 and − 2 charged COT ligands, respectively. Assumed geometric structures and their parameters for the X^- and A^- state of $[Eu(COT)]_\infty^-$ are $r_a(X^-)$=2.181, $r_b(X^-)$=2.475, $r_a(A^-)$=2.454, $r_b(A^-)$=2.220.

Fig. 3-3 shows the formal charge distribution, together with the optimized distances

between the metal and the center of gravity of the COT carbon ring. The formal charges are easily determined by counting the number of electrons among the valence orbitals, namely the 6s and L_δ orbitals, since each orbital is well localized on Eu or COT, as discussed later. In this figure, the black, dotted, and white circles denote neutral, +1, and +2 charged metals, and dotted and white plates denote −1 and −2 charged COT ligands, respectively. As lower-lying electronic states, the author found two different doublet states (with 4f core ECP), that the author calls the X^- and A^- states. The A^- state arises by a one-electron transfer from the left end COT^{2-} to the right end Eu^+ ion in Fig. 3-3(a).

Interestingly, computational results showed that exposed metal atom carried a charge of +1 and 0 in the X^- and A^- states respectively, and the COT^- ligand was always the exposed ligand in the A^- state, as shown in Fig. 3-3. Moreover, the A^- state was an excited state, namely higher than the X^- state in energy, in all the cluster sizes studied. Additional details will be discussed in Section 3.3.5.

The optimized distances between Eu and COT in Fig. 3-3 show a very small basis set dependency, namely the maximum deviation between CORE-A and -B was about 0.03 Å for *n*=1-3. The geometry optimization with 4f VALENCE performed only for *n*=1 shows a slightly larger deviation yet less than 0.1 Å in the distance between Eu and COT.

The geometries of the X^- and A^- states are specified with two kinds of distances, r_a and r_b as shown in the lower part of Fig. 3-3. r_a is the bond distance between an Eu^{2+} and the left-hand neighboring COT, and r_b is the one between an Eu^{2+} and the right-hand neighboring COT. It is interesting to point out that in the X^- state, $r_a < r_b$, namely, r_a is about 2.1-2.2 and r_b is about 2.4-2.6, while the opposite is true in the A^- state, where r_a is about 2.4-2.6 and r_b is about 2.2. It is assumed that the polymer $\left[\mathrm{Eu(COT)}\right]_\infty^-$ takes a single set of the parameters in the X^- state, $r_a(X^-)$=2.181 and $r_b(X^-)$=2.475, which are the averaged values of those for *n*=4. For the

A^- state, $r_a(A^-)$=2.454 and $r_b(A^-)$=2.220 were assumed in a similar manner.

Table 3–1. Optimized C–C bond distances (Å) of the COTs in the X^- and A^- states.[a,b]

		X^- state			
		COT(1)	COT(2)	COT(3)	COT(4)
$(n,n)^-$	4f CORE	C-C	C-C	C-C	C-C
$(1,1)^-$	A	1.430	——	——	——
	B	1.420 (1.419)[d]	——	——	——
$(2,2)^-$	A	1.430	1.431	——	——
	B	1.420	1.421	——	——
$(3,3)^-$	A	1.430	1.431	1.431	——
	B	1.420	1.421	1.421	——
$(4,4)^-$	A	1.430	1.431	1.432	1.432
		A^- state [c]			
		COT(1)	COT(2)	COT(3)	COT(4)
$(n,n)^-$	4f CORE	C-C	C-C	C-C	C-C
$(1,1)^-$	A	1.394 (1.454)	——	——	——
	B	1.383 (1.444) 1.383[d] (1.444)[d]	——	——	——
$(2,2)^-$	A	1.397 (1.454)	1.427 (1.433)	——	——
	B	1.386 (1.445)	1.417 (1.423)	——	——
$(3,3)^-$	A	1.397 (1.455)	1.430 (1.433)	1.430 (1.431)	——
	B	1.386 (1.446)	1.419 (1.423)	1.420 (1.421)	——
$(4,4)^-$	A	1.397 (1.455)	1.430 (1.433)	1.432 (1.432)	1.431 (1.431)

[a] For *n*=1-3, the optimized distances are calculated by the 4f CORE-A and -B, and for *n*=4, they are calculated only by the 4f CORE-A.
[b] COT(*i*) denotes *i* th COT counted sequentially from the left in Figure 3-3.
[c] In the A^- state, because of the C_{4v} structure, two kinds of C-C bond lengths are distinctively shown, longer being in parenthesis.
[d] The optimized distances are calculated by the 4f VALENCE.

Table 3-1 summarizes the optimized C-C bond distances of the COT ligands in the X^- and A^- states to focus on the geometry of each COT. Here, COT(*i*) denotes the *i* th COT counted sequentially from the left in Fig. 3-3 and Eu(*i*) denotes also the *i* th Eu from the left. Geometry optimizations for the X^- state with both 4f CORE-A and -B for *n*=1-3 and with 4f CORE-A for *n*=4 yielded C_{8v} structures with all of the C-C distances are about 1.42 Å. For the A^- state, the optimizations led to C_{4v} structures, in which only COT(1), with the formal charge

of −1, has a largely distorted C_{4v} structure due to the Jahn-Teller effect and has the two kinds of C-C distances of about 1.39 and 1.45 Å, whose average value is again 1.42 Å. It is noted that, as the position number i increases, the symmetry of COT(*i*) becomes closer to C_{8v}, reflecting their formal charge of −2. All of the C-H bond distances were 1.09 Å.

The frequency analysis was also carried out for each state of *n*=1-3 with 4f CORE-A. For *n*=1 and 2, the optimized geometries for the X^- and A^- states were both stable structures. For *n*=3, while the X^- state was stable, a doubly degenerate imaginary frequency of 8.89 cm^{-1} was obtained for the A^- state along a lateral motion from the *z*-axis. However, the energy lowering from the C_{4v} structure was only 0.26cm^{-1}, thus the geometries restricted to the C_{4v} structure for the A^- state of *n*=3 were used in the following calculations. For *n*=4, the optimization was performed only with 4f CORE-A, assuming the C_{8v} and C_{4v} structures for the X^- and A^- states, respectively. Based on these results, the optimized structures with 4f CORE-B except for *n*=4, for which those with 4f CORE-A, will be used for the rest of discussion, unless otherwise stated.

To see the charge distribution, the Mulliken charge calculated by 4f CORE-A with the formal charge in Fig. 3-4 are compared. Here, it is found that formal charges of +2, +1, and 0 of Eu correspond approximately to 0.8, 0.2 and −0.4 of the Mulliken charges, respectively. Similarly, formal charges of −2 and −1 of COT correspond to −1.0 and −0.6 of the Mulliken charges, respectively. Moreover, it is noticed that this correspondence always holds irrespective of the cluster size and the electronic state. Although the formal charge in the point charge models, to be discussed later, is different from the Mulliken charge quantitatively, it reflects the qualitative tendency of the charge distribution.

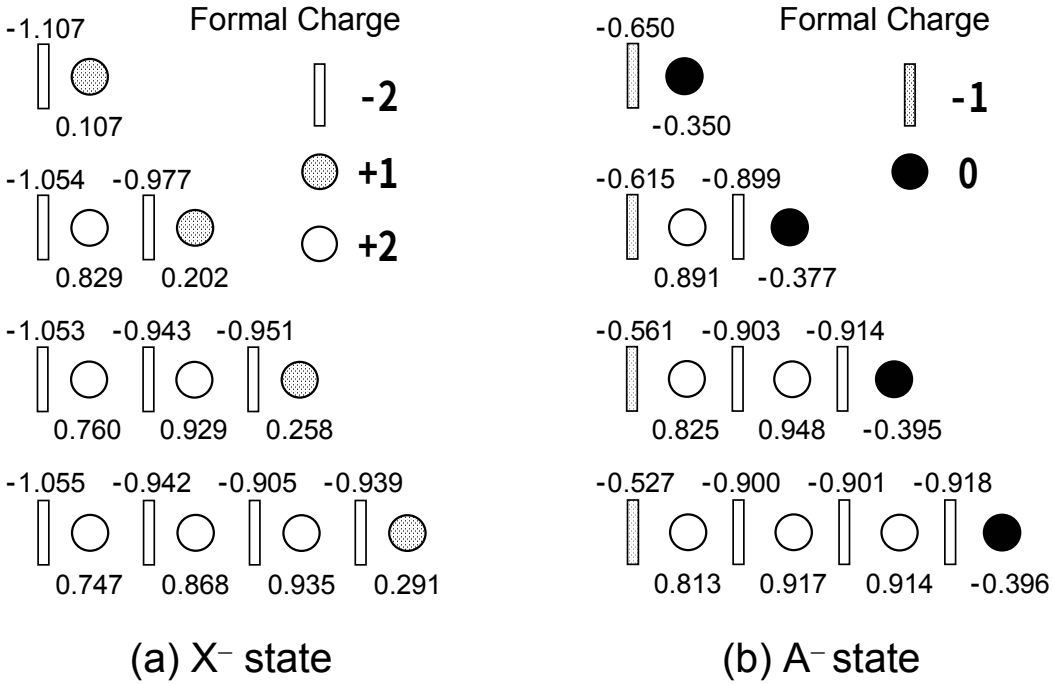

Fig. 3-4 Mulliken population analysis with 4*f* CORE-A and formal charge distribution for (a) X^- and (b) A^- states of $(n, n)^-$ (n=1-4).

Lastly, Fig. 3-5 presents the Kohn-Sham orbitals of the HOMO, the second and the third HOMO of n=2 in the X^- state, plotted using the Molekel program. [3.41]

These orbitals are well localized on each portion, namely the HOMO is on Eu(2) and the second and the third HOMO are on COT(1) and COT(2), respectively. Note that the latter two orbitals have the same δ symmetry. Interestingly, the HOMO is strongly polarized away from the surrounding COT^{2-} due to their repulsive interaction as also observed in the monohalides of alkali-earth and Ln. [3.42] These characteristics were seen for all of the cluster sizes of n=1-4, both for the X^- and A^- states. Based on the orbital localization and ionic charge distribution of $Eu_n(COT)_n^-$, it is concluded that these clusters have a strong ionic bonding.

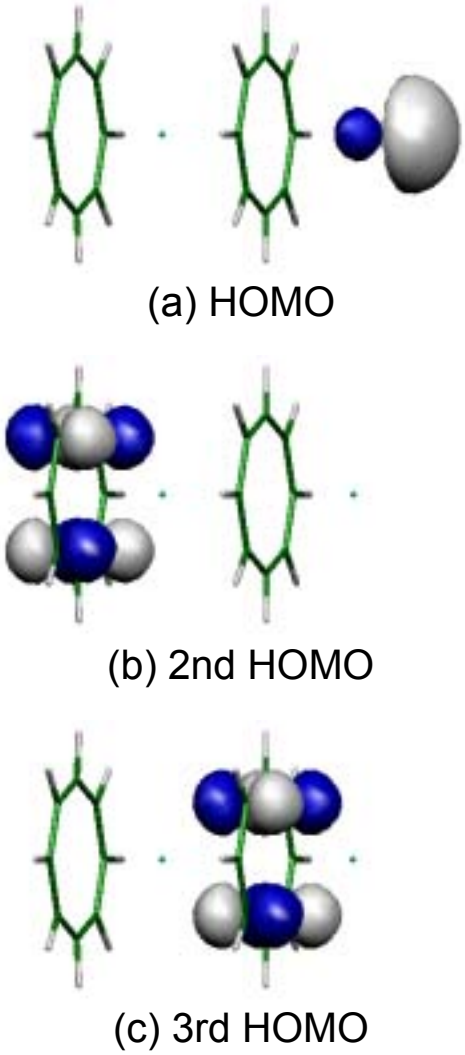

Fig. 3-5 The HOMO (a), second (b) and third HOMO (c) for the X^- state of $(2, 2)^-$. Each MO is essentially localized on the Eu atom and COT ligands, respectively.

3.3.3. Valence Orbital Energy and Detachment Energy.

Hartree-Fock Orbital Energy

Before calculating the theoretical vertical detachment energy (VDE), the valence orbital energies are estimated to consider possible detachment channels. For this purpose, the Hartree-Fock (HF) orbital energies, which are easily related to VDE with Koompans' theorem, are more meaningful than the Kohn-Sham orbital energies. Thus, the UHF orbital energies

with 4f CORE-B are first calculated and their valence orbital energies are summarized in Fig. 3-6. Here, 6s(X^-) and 6s(A^-) denote each 6s orbital of the terminal Eu^+ and Eu in the X^- and A^- states respectively, and L_δ(COT(*i*)) denote the L_δ orbital localized on each COT(*i*) in the X^- state, as shown in Fig. 3-6(b).

It is noticed that the orbital energy of 6s(X^-) decreases with the cluster size, however, that of 6s(A^-) is almost constant. The energy of L_δ(COT(1)) is almost independent of the cluster size. In addition, in a specific cluster size *n*, the orbital energy of each L_δ(COT(i)) shows a critical dependence on its position in the clusters, namely, it becomes lower as going to the right (as the position number *i* increases). In Section 3.3.4, the origin of the characteristics of these valence orbital energies will be revealed.

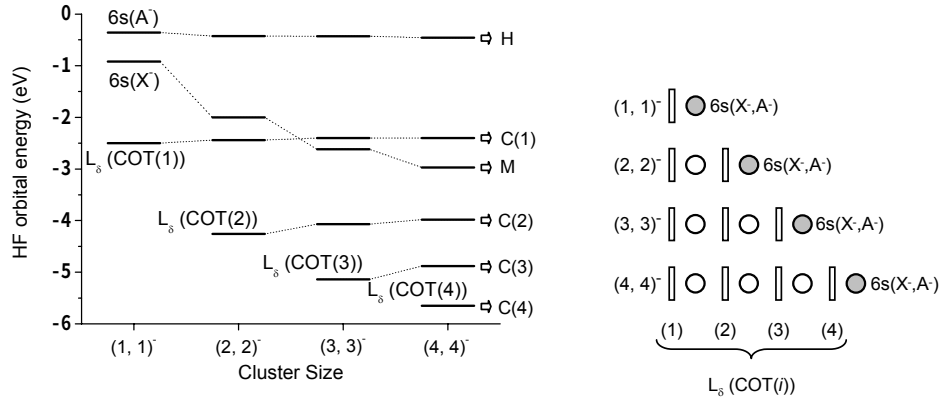

(a) HF orbital energy diagram (b) Label of each orbital

Fig. 3-6 (a) Energy diagram of the valence orbitals (eV) and the corresponding label for detachment peaks. All results are calculated by the UHF method with 4f CORE-B and the optimized distances given in Table 1 and Figure 3. (b) Label of each molecular orbital: 6s(X^-,A^-) denotes the 6s orbital of the terminal Eu in the X^- and A^- states, and L_δ expresses the one of each COT in the X^- state. COT(*i*) denotes *i* th COT counted sequentially from the left in this figure.

Further, to investigate the 4f orbital energy and the dependency on the ECPs, the UHF orbital energies for the X^- state by using 4f VALENCE with the highest spin-multiplicity of 9 and 16 for *n*=1 and 2 were calculated, respectively. Table 3-2 summarizes and compares the 6s, L_δ, L_π, and 4f orbital energies calculated by 4f VALENCE and 4f CORE-B.

In spite of the different ECPs and basis sets for Eu, the 6s, L_δ, and L_π orbital energies calculated with these two methods are in agreement with each other within a maximum deviation of 0.17 eV. The orbital energies of 4f in Table 3-2 are much higher than those of the bare Eu^+ and Eu^{2+} cations due to the strong ligand field by the surrounding COT^{2-}. [3.42,43] Moreover, they split to one $4f_\sigma$ and doubly degenerate $4f_\pi$, $4f_\delta$, and $4f_\phi$ components within 0.25 eV in the C_{8v} structure. The magnitude of the splitting pattern of 4f is significantly different from that of the 5f orbitals of actinocenes. [3.44-46] Since the 5f orbitals are more extensive than the 4f orbitals and their energies are higher than the HOMO (L_δ) of COT, the interactions between the 5f orbitals and COT ligands are much stronger. On the other hand, because the compact 4f orbitals of lanthanide are lower in energy than that of the inner orbitals of COT, the splitting energies are smaller, and the splitting pattern is expected to depend strongly on their local charge.

Although no calculations with other spin-multiplicities were performed, because of the small splitting energies of the 4f orbitals and the reasonable agreement in the other valence orbital energies, it is considered that the 4f shell can be treated as core, unless the photodetachment of a 4f electron is explicitly examined. In that case, as shown later, Koopmans' theorem overestimates the VDE very much, and the DFT method including orbital relaxation effects shows much better performance. An interesting point to be added here is that the orbital energies of 4f and L_π also depend on their positions in the clusters. The reason for this dependence is similar to that of L_δ as discussed in Section 3.3.4

Table 3–2. Comparison of the UHF orbital energies calculated by 4f CORE-B and 4f VALENCE for the X^- state.[a,b]

	$(1, 1)^-$			$(2, 2)^-$	
	4f VALENCE	4f CORE-B		4f VALENCE	4f CORE-B
6s(1)	–0.916	–0.929	6s(2)	–2.072	–2.003
L_δ(COT(1))	–2.371	–2.501	L_δ(COT(1))	–2.387	–2.443
L_π(COT(1))	–7.494	–7.587	L_δ(COT(2))	–4.142	–4.257
$4f_\delta(1)$	–9.516	———	L_π(COT(1))	–7.572	–7.581
$4f_\phi(1)$	–9.620	———	L_π(COT(2))	–9.266	–9.436
$4f_\pi(1)$	–9.643	———	$4f_\delta(1)$	–9.512	———
$4f_\sigma(1)$	–9.753	———	$4f_\phi(1)$	–9.550	———
			$4f_\pi(1)$	–9.689	———
			$4f_\sigma(1)$	–9.709	———
			$4f_\sigma(2)$	–11.089	———
			$4f_\delta(2)$	–11.109	———
			$4f_\phi(2)$	–11.198	———
			$4f_\pi(2)$	–11.218	———

[a] Calculations on the optimized geometry with 4f CORE-B shown in Table 3-1 and Fig. 3-3.
[b] COT(*i*) and 4f(*i*) denote orbitals on the *i* th COT and Eu, respectively, counted sequentially from the left in Fig. 3-3.

Detachment from 6s(X^-,A^-) and L_δ(COT(1))

Having investigated the valence and 4f orbital energies, the author assigned the two detachment channels: firstly, the M peak to a detachment from 6s(X^-), and secondly, the C(1) peak to a detachment from L_δ(COT(1)) as shown in Fig. 3-1 and 3-6.

Then, the VDEs for these two channels were calculated using the more quantitative ΔDFT method, in which the VDEs were evaluated from the difference in the DFT total energies of $Eu_n(COT)_n^-$ and the corresponding one electron detached neutral states at the anion equilibrium geometry. First, the dependency of the calculated VDEs on the three computational methods, 4f CORE-A, -B, and 4f VALENCE were investigated. It is found that

the differences between 4f CORE-A and -B for the M and C(1) peaks of n=1-4 are less than 0.1 eV, and those between 4f CORE-B and 4f VALENCE for the two peaks of n=1 are also less than 0.1 eV. Therefore, in the following discussion, only the calculation results with 4f CORE-B will be used.

In Figs. 3-1 and 3-2, the calculated VDEs with 4f CORE-B are presented as solid sticks along with the experimental spectra. The calculated values for the two peaks M and C(1) in Fig. 3-1 are in a fair agreement with the experiment at 355 nm. Especially, they reproduce the characteristic behavior; the first peak shifts to the higher energy side as the cluster size increases, while the second peak is independent of the cluster size.

As for electron detachment from the excited A^- state, two detachment channels are also expected: firstly, from 6s(A^-) (H peak), and secondly, from the COT^{2-} ligands. For each cluster size, the calculated VDEs are obtained for the H peak near 0.9 eV and for the second peak near 3.0 eV. Because this second peak of the A^- state would overlap with the broad C(1) peak of the X^- state, it is experimentally difficult to identify the second peak distinctly from these two peaks. On the other hand, the H peak can be observed clearly for cluster size $n\geq2$ as in Fig. 3-1. Although the H peak for n=1 might be overlapped with the M peak, the weak peak near 0.9 eV can be assigned to the detachment from 6s(A^-) of the excited A^- state, and its weak intensity reflects an evidence for the minor production of the A^- state. In fact, Hosoya et al. reported that the intensity ratio between the H and M peaks depended on the source conditions such as stagnation pressure for He carrier gas; the lower stagnation pressure gave the H peak intensity stronger relative to that of the M peak. Note that the H peak becomes prominent with cluster size, which seemingly corresponds to the smaller energy difference between the X^- and A^- states in larger clusters. This point will be discussed further in Section 3.3.5

Detachment form each L_δ(COT(i)) orbital

Next, the author considers electron detachment from each L_δ(COT(i)) in the X^- state (C(i) peak). The VDEs were calculated using the UHF orbital energies in Fig. 3-6 and Koopmans' theorem instead of the ΔDFT method, because the latter method cannot yield excited states with the same symmetry as the lowest state due to the convergence problem practically and the Hohenberg-Kohn theorem conceptually, namely, each state obtained by the electron detachment from these L_δ orbitals belongs to the same symmetry. The results are compared with the experimental spectra taken with the photon energy of 213nm (5.83eV) in Fig. 3-2. The calculation also reproduces the characteristic peaks qualitatively. The successive peaks whose number is equal to that of the COTs can be assigned to detachment from each L_δ(COT(i)).

Detachment from 4f orbitals

Let us consider the electron detachment from the 4f orbitals in the X^- state. A peak around 3.7 eV was found in both the spectra of n=1 and 2 of Fig. 3-2. (That for n=2 appears as a shoulder.) Fig. 3-7 shows the photoelectron spectrum for Ba-COT cluster anions of $Ba_2(COT)_2^-$ together with that for $Eu_2(COT)_2^-$ at 213 nm measured by Hosoya et al. Since a Ba atom has an electron configuration of [Xe]$4f^0 6s^2$, it is expected that Ba-COT forms an identical sandwich cluster with Eu-COT without 4f electrons, where a Ba atom takes a Ba^{2+} state in the clusters. In fact, Hosoya et al suggested that the mass distributions of anionic and neutral Ba-COT are very similar to those of Eu-COT; the successive series of (n, n+1), (n, n), and (n, n−1) clusters for Ba-COT appear prominently. [3.47] The abundance of $Ba_1(COT)_1^-$ was too small to measure the photoelectron spectrum. As expected from the identical ionic distribution between Eu-COT and Ba-COT, both give almost the same EA and similar overall

features as shown in Fig. 3-7, while there is apparently an additional photodetachment contribution of 4f orbitals around 3.5-4.0 eV in the spectra of $Eu_2(COT)_2^-$.

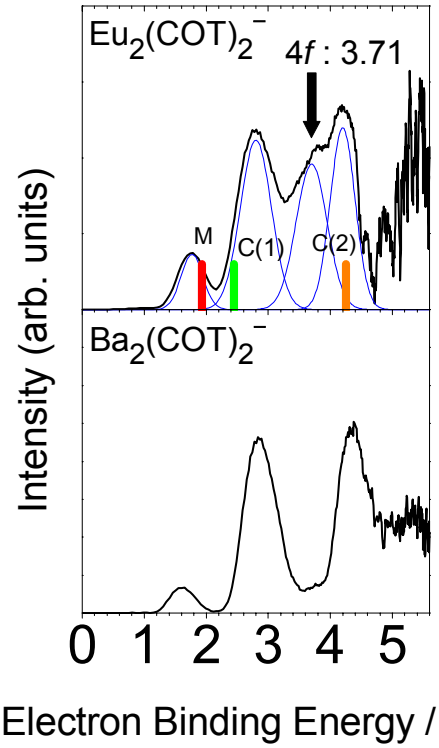

Fig. 3-7 The photoelectron spectrum for $Ba_2(COT)_2^-$ together with that for $Eu_2(COT)_2^-$ at 213 nm. There is apparently an additional photodetachment contribution of 4*f* orbitals around 3.5-4 eV in the spectra of $Eu_2(COT)_2^-$. The spectral envelopes in the 213 nm spectra were deconvoluted into a train of components by gaussian functions. For $Eu_2(COT)_2^-$ at 213 nm, one additional peak appears at 3.71 eV as labeled by a downward arrow.

To assign the position of the electronic transition clearly, the spectral envelopes in the 213 nm spectra were deconvoluted into a set of component Gaussian functions as indicated by the curves in Fig. 3-7. For $Eu_2(COT)_2^-$ at 213 nm, one additional peak appears at 3.71 eV, as labeled by a downward arrow in Fig. 3-7.

With the ΔDFT method, the final neutral states were calculated with one hole in the $4f_\phi(1)$ as the initial guess, VDEs were obtained for *n*=1 and 2 as 4.256 eV and 4.313 eV, respectively. Especially for *n*=2, the converged hole state was not localized in 4f(1), but delocalized in both 4f(1) and 4f(2). Therefore, the experimental peak around 3.7 eV is due to a detachment channel from the delocalized 4f orbitals. Since the 4f orbitals are very compact, the

detachment of a 4f electron causes a very large shrinking of other outer orbitals and stabilizes the final neutral state significantly. By this reason, the VDE calculated for the detachment of 4f electron with ΔDFT becomes much smaller than that predicted with Koopmans' theorem given in Table 3-2. It is noted that this type of large orbital relaxation upon photoionization from a compact sized orbital was observed previously in the $(3d_\sigma)^{-1}$ ionization channel of V_nBz_{n+1}. [3.7] From these results, it seems plausible to assign the peak around 3.7 eV to the $4f^{-1}$ channel, although the photoelectron spectrum for the $Ba_1(COT)_1^-$ cannot be measured.

The source of the difference (about 0.6 eV) between the experimental and calculated VDEs for the $4f^{-1}$ channel is attributable to the ECP or the DFT method, because the ΔDFT method with the 4f VALENCE treatment overestimates the ionization energies for the $4f^{-1}$ channel of the Eu^+ and Eu^{2+} cations by about 1 eV. Therefore, the ΔDFT results for the $4f^{-1}$ channel for n=1 and 2, with an overestimation of about 0.6 eV, are reasonable within this calculation error. For more detailed analyses, it would be necessary to calculate with other theoretical methods. Although this remains as a future study, the detachments from the 6s and COT(i) were not affected very much by the explicit inclusion of 4f orbitals, therefore the characteristic behavior of these detachments will be studied in the next section.

3.3.4. Point Charge Model.

Using the HF orbital energies in Fig 3-6, it is noticed that Koopmans' theorem is able to explain the cluster size dependences of the M, C(i), and H peaks. The variation of the HF orbital energies can be divided into kinetic and potential energy parts. For the relevant valence orbitals, it is observed that the kinetic energies showed very weak cluster size dependences, since each molecular orbital is largely localized and does not change their shape significantly as shown in Fig. 3-8. It is therefore considered that the origin of the variation of the orbital

energy is due to the potential part, especially the intracluster electrostatic potential.

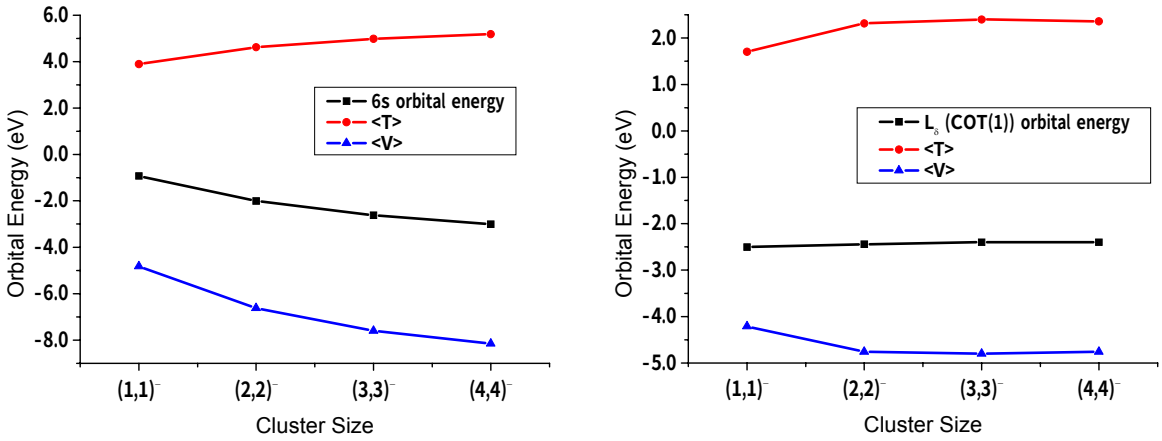

(a) 6s orbital of Eu^+ in the X^- state (b) L_δ orbital of COT(1) in the X^- state

Fig. 3-8 Hartree-Fock orbital energy and its potential part <V> and kinetic energy part <T>. (a) 6s orbital of Eu^+ in the X^- state. (b) L_δ orbital of COT(1) in the X^- state.

Here, two point charge models are developed reflecting the strong ionic bonding of the $Eu_n(COT)_n$ clusters. In a model, only the electrons belonging to a metal atom or COT ligand are explicitly treated, from which photodetachment takes place, and the remaining Eu metals and COT ligands as point charges distributed as in Fig. 3-3. Then, the DFT calculation was performed for one Eu atom or one COT molecule with the surrounding point charges with the CHARGE keyword in the Gaussian program package, and calculated VDEs by the ΔDFT method with thus calculated energies. This method is referred to the "Point Charge+DFT" method.

As another model, using classical electrostatic formula, the electrostatic potentials which are created by the surrounding point charges Q_i at $\mathbf{r}_i$ are evaluated namely,

$$V_{class}^{a}(\mathbf{r}) = \sum_{i=1} \frac{Q_i}{|\mathbf{r} - \mathbf{r}_i|} \qquad (3\text{-}1)$$

Here, $\mathbf{r}$ is a position vector at which the potential is evaluated and is the average position of the electron detaching from the orbital *a*. For $\mathbf{r}_i$, the optimized geometry shown in Fig.

3-3 is applied. The electron binding energy is the work to be done on an electron to detach it to infinity. Therefore the electrostatic potential can be regarded as VDE, and this method is called as the V_{class}^{a} method. In what follows, these two approximate point charge models provide us with a simple and qualitative explanation for the photoelectron spectra and reveal that the characteristic behavior of the M, C(*i*) and H peaks originates from the one-dimensional strong ionic bonding.

M Peak.

The M peak was assigned to electron detachment from the 6s orbital of Eu^+ in the X^- state (6s(X^-)). Therefore, the remaining Eu^{2+} and COT^{2-} ligands were approximated by +2 and −2 point charges, respectively and placed along the *z*-axis using the optimized geometry, as shown in Fig 3-3. Then, the Point Charge+DFT method was employed. As for the $V_{class}^{6s(X^-)}$ method, considering the spatial extent of 6s(X^-) (Fig. 3-5), a position $\mathbf{r}$ of the detaching electron was taken at 1.733Å outside that of Eu^+ for all *n*. This value of 1.733Å comes from the expectation value for the position (orbital centroid) of the 6s(X^-) electron for *n*=1. In the left part of Fig. 3-9 shows the results obtained by the two point charge models in comparison to other calculation results and experiment. Note that the absolute value of $V_{class}^{6s(X^-)}$ is shifted to fit with the ΔDFT calculation value at *n*=1. Clearly, the point charge models reproduce other data qualitatively in spite of their simplicity. Especially, the asymptotic behavior of VDE is well reproduced. Therefore, it is concluded that the characteristic behavior of the M peak results from the variation of the electrostatic potential felt by the detaching electron induced by the surrounding Eu^{2+} and COT^{2-} which can be approximated as point charges.

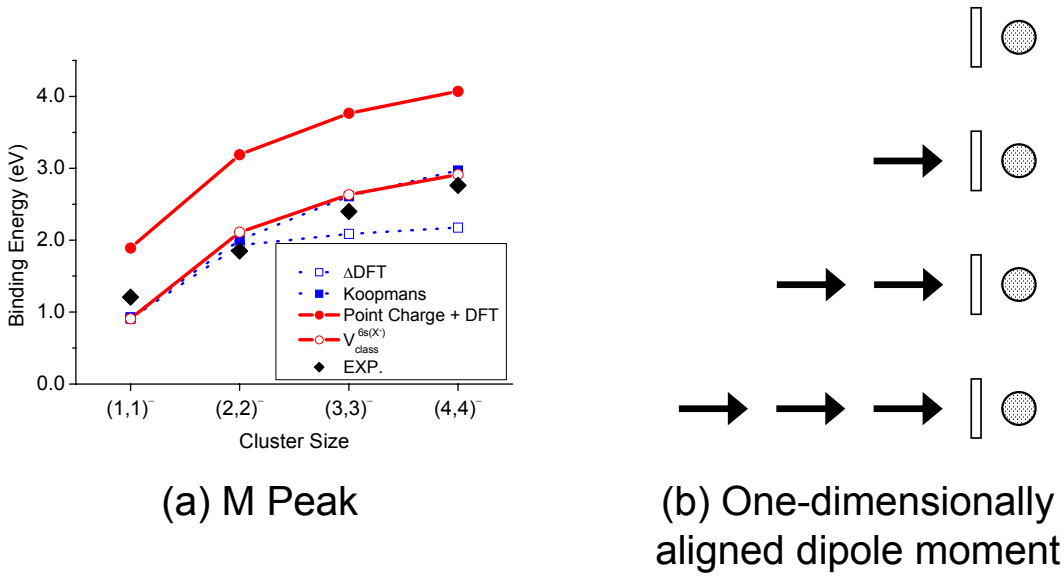

Fig. 3-9 (a) Calculation results of the point charge models for the M peak of $(n, n)^-$ (n=1-4) in comparison with other calculations and experimental data. (b) Schematic diagram for the Coulombic interaction between the detaching electron for the M peak and dipole moments which align one-dimensionally in the same direction.

Now, the relation between the cluster size and the variation of the electrostatic potential is considered. As schematically shown in the right part of Fig. 3-9, viewing from Eu^+, the increase of the cluster size corresponds to the attachment of a pair of +2 and −2 point charges to the left side of the cluster: this pair is regarded as an electric dipole. The Eu-COT cluster has the one-dimensional structure, so that the dipoles align one-dimensionally in the same direction on increasing the cluster size. Therefore, the increase of the cluster size can be regarded as the stacking of dipoles on the left side of the cluster. Each dipole stabilizes the detaching electron in Eu^+ by an energy that is inversely proportional to the square of the distance between the detaching electron and the attached dipole. The sum of such stabilization energies converges asymptotically to a constant value with n. An asymptotic convergence is observed as a characteristic behavior of the M peak and reflects the one-dimensional ionic bonding structure of the $Eu_n(COT)_n^-$ clusters.

C(*i*) and H Peaks.

In a similar manner, the point charge models can be applied to the C(*i*) and H peaks. As mentioned before, the C(1) peak is always assigned to the electron detachment from $COT(1)^{2-}$ in the X^- state ($L_\delta(COT(1))$) and the H peak to the detachment from the neutral Eu(*n*) in the A^- state ($6s(A^-)$). Moreover, both peaks hardly shift on increasing the cluster size. In applying Eq. (3-1) to the C(1) peak, the value was calculated at the center of the COT ring. As for the H peak in the A^- state, a value of 0.844Å was used as the position of $6s(A^-)$ centroid.

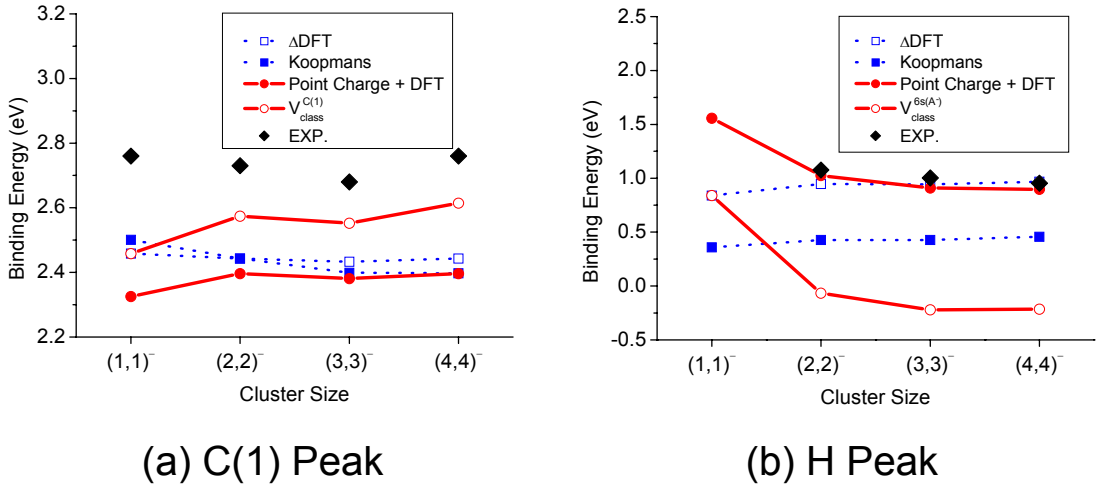

Fig. 3-10 Calculation results of the point charge models for the C(1) (a) and H (b) peaks of $(n, n)^-$ (n=1-4) in comparison with other calculations and experimental data.

Fig. 3-10 shows the calculated results for the C(1) and H peaks in comparison to other data. The two point charge models also give a qualitative explanation for the size independent behavior of the C(1) and H peaks. Namely, the electrostatic potentials at the left end COT(1) in the X^- state and neutral Eu in the A^- state are almost independent of the cluster size.

For the C(1) peak, let us consider the relation between the cluster size and the variation of the electrostatic potential in view of the left end COT(1) in the X^- state with looking at Fig. 3-3. In this case, the increase of the cluster size corresponds to the change of the right end Eu^+ to Eu^{2+} and the addition of a pair of COT^{2-} and Eu^+ ; the attachment of a group of +1, −2, +1 point charges to the right side of the cluster. Since this group is regarded as an electric

quadruple, the stabilization energy is inversely proportional to the third power of the distance between the detaching electron on COT(1) and the quadruple. Namely, the electrostatic potential at the left end COT(1) in the X^- state is almost independent of the cluster size in contrast to that at the right end Eu^+ (M peak).

As for the H peak, a similar explanation can be applied, namely, viewing from the neutral Eu in the A^- state, the increase of the cluster size corresponds to the attachment of a group of −1, +2, −1 point charges, which is approximated as a quadruple, to the left side of the cluster. Therefore, the cluster size dependence of the C(1) and H peaks is much smaller than that of the M peak.

Next, the author gives a simple explanation for the strong position dependence in the orbital energies of COT(*i*) and 4f(*i*) in the X^- state as shown in Fig. 3-6 and Table 3-2. For example, in the $(3, 3)^-$ cluster, the L_δ orbital energy of COT(2) is about 1.7 eV lower than that of COT(1), and that of COT(3) is about 1.1 eV lower than that of COT(2). Looking at Fig. 3-3 and the lower part of Fig. 3-9, it is noticed that COT(3) is stabilized by two dipole moments consisting of the combination of $(COT(1)^{2-}\ Eu(1)^{2+})$ and $(COT(2)^{2-}\ Eu(2)^{2+})$, while COT(2) is stabilized by only one dipole moment of $(COT(1)^{2-}\ Eu(1)^{2+})$. Therefore, the orbital energy becomes lower as going to the right because of more stabilization by dipole moment stackings. A similar explanation is applicable to other cluster sizes, so that this gradient among the orbital energies of COT(*i*) and 4f(*i*) is also regarded as an interesting character in the one-dimensional ionic bonding cluster.

It should be pointed out that, contrary to the X^- state, the L_δ orbital energies of COT(*i*) in the A^- state do not show a clear stairs-like behavior in the cluster. This is possibly because the A^- state does not show a clear dipole chain structure, namely a significant bond alternation, as shown in Fig. 3-3.

Based on the above discussion, each VDE is estimated for the polymer $[Eu(COT)]_\infty^-$ using the assumed geometric parameter $r_a(X^-/A^-)$and $r_b(X^-/A^-)$ for the X^- and A^- state, respectively, in Section 3.3.2 and Fig. 3-3. In the calculation, firstly the variation of each VDE from n=4 to n=∞ is accumulated using Eq. (3-1), and secondly the accumulated variation was added to the experimental data of n=4. In this way, each VDE empirically to n=∞ was extrapolated and values of 2.894, 2.449, and 0.972(eV) for the M, C(1) and H peaks were obtained, respectively. The VDE for the M peak showed a monotonous convergence, and the difference in the VDE between n=30 and n=∞ was 0.096 eV. On the other hand, those for the C(1) and H peaks converged quickly at n=4.

Similar point charge models have been used for the analyses of, for example, chemical shift in core ionization energies, [3.48-50] electron affinities and ionization energies, [3.51,52] solvent effect in condensed phase, [3.53,54] and so on. In these cases, the point charge models have been used mainly for analyzing the substituent effects. In this work, the variation of the intracluster electrostatic potential has been studied by increasing the cluster size, and the characteristic behavior of the photodetachment spectra has been analyzed. Similar phenomena are also expected in other clusters with a strong ionic bonding, to which the point charge models can be conveniently applied.

3.3.5. Relations among the X^-, A^- and X States.

In this last section, the author investigates the relative energies among the X^-, A^- and neutral ground X states to consider the stability of the A^- state. Recently, several groups have suggested that a laser vaporization or pulsed arc method generates clusters in metastable structures. [3.12,55] Therefore, it is very interesting to look at the energy and structure

relations between the X^- and A^- state theoretically. The adiabatic excitation energies from X^- to A^- of *n*=1-4 were calculated as 1.569, 1.413, 1.384 and 1.382 eV, respectively.

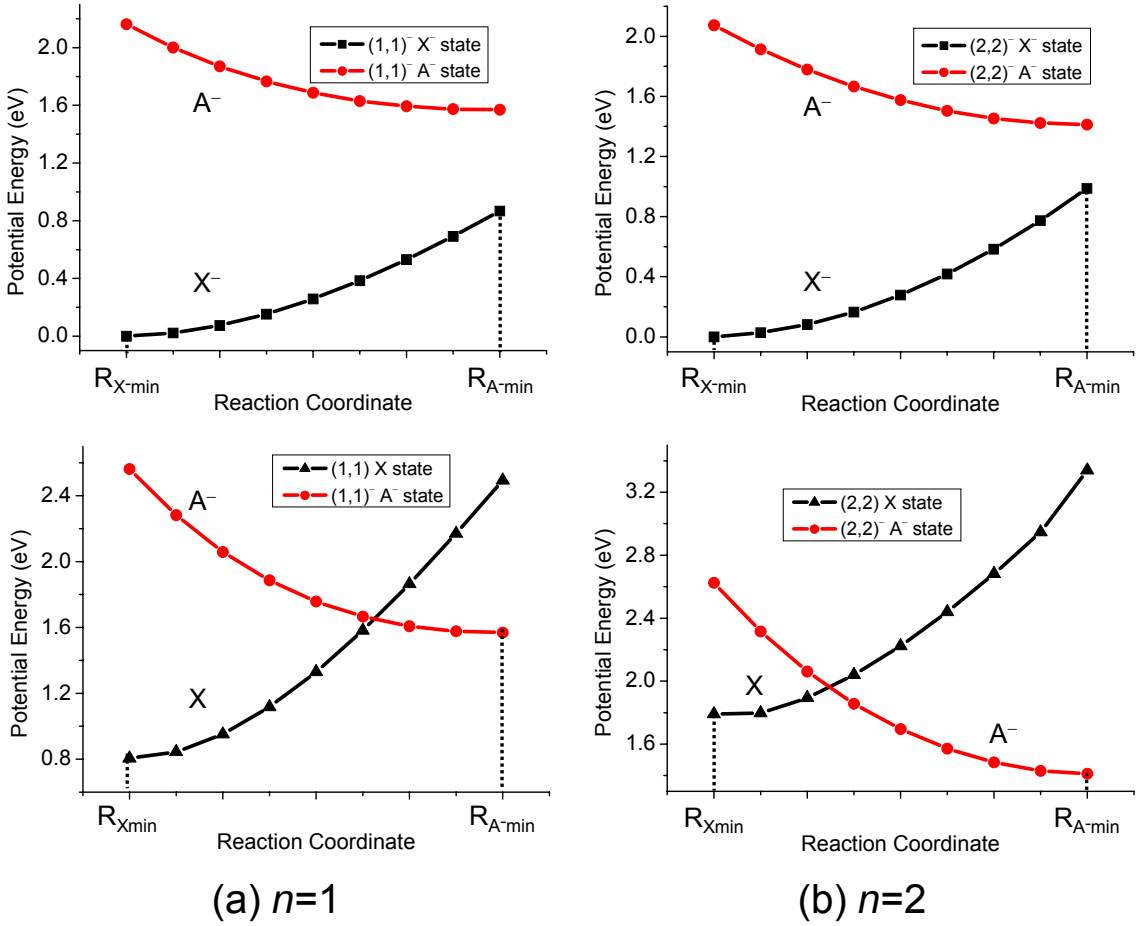

Fig. 3-11 One-dimensional potential curves of the X^- and A^- states alone the linear synchronous transit path connecting the minimum structures of these two states for n=1,2, and those for the X and A^- states, for *n*=1,2.

To investigate possible relaxation mechanisms from the metastable A^- state, one-dimensional potential energy curves were calculated for the X^- and A^- states of *n*=1 and 2, as shown in the upper part of Fig. 3-11. Here the potential energy is relative to the minimum energy of the X^- state. R_{X^-min} and R_{A^-min} represent the optimized nuclear structure for the X^- and A^- state, respectively. The reaction path is an artificial one on which all the structural parameters are assumed to change linearly from R_{X^-min} to R_{A^-min} using the linear synchronous transit path [3.33] in the cartesian coordinates and was calculated with 4f CORE-B. Clearly,

the A^- state is higher in energy than the X^- state at all the coordinates.

The relative energy between the A^- and the neutral X state is also investigated along a similar artificial reaction path between R_{Xmin} and R_{A^-min}, and the potential curves were shown in the lower part of Fig. 3-11. The neutral X state is the final state of the one-electron detachment from the terminal Eu^+ in the X^- state as discussed in Chapter 4. [3.56] As for the A^- and X state potential curves of n=1, the minimum energy of the A^- state is higher than that of the X state and these potential curves show a crossing, therefore there is a low barrier on the reaction path from A^- to X. A magnitude of the barrier is only about 600 cm^{-1}. On the other hand, for n=2, the minimum energy of the A^- state is lower than that of the X state and the reaction barrier from R_{A^-min} to R_{Xmin} is about 1 eV which is much larger than that of n=1.

From these calculation results, two possible relaxation processes can be considered from the A^- state: (i) radiative relaxation to the X^- state with fluorescence, $A^- \rightarrow X^- + h\nu$, (ii) nonradiative autodetachment to the X state, $A^- \rightarrow X + e^-$. In the A^- state, the electronic configurations of the COT^- and neutral Eu metal portions are $L_\sigma^2 L_\pi^4 L_\delta^3$ and $4f^7 6s^2$, respectively and those in the X^- state are $L_\sigma^2 L_\pi^4 L_\delta^4$ and $4f^7 6s^1$, respectively, so that the process (i) is equivalent to the one-electron transition from the 6s to L_δ orbital. Because these orbitals have different symmetries of σ and δ with respect to the molecular axis, this σ to δ transition is forbidden. Therefore, the radiative relaxation process (i) cannot take place effectively. The process (ii) can be considered as a simultaneous process consisting of an electron transfer from 6s to L_δ and an electron detachment from 6s. The theoretical estimate of such an autodetachment lifetime is possible using, for example, the complex coordinate method [3.57], but the efficiency of the process can be simply discussed by comparing the potential curves alone. Note that the autodetachment can take place only in the nuclear configurations where the A^- state is less stable than the X state. Therefore, from the lower part

of Fig. 3-11, the autodetachment probability in n=1 is expected to be larger than that in n=2 because the former has a smaller reaction barrier to arrive at the nuclear configurations where the autodetachment becomes possible. In the spectra of n=1 in Fig. 3-1, the H peak is close to the M peak, so that it would be difficult to verify the preparation of the A^- state unambiguously. On the other hand, the small H peaks can be observed in the spectra for the A^- state of n=2 or larger. This experimental observation is consistent with the theoretical analysis above, since once the A^- state is prepared, it relaxes neither to the X^- nor X state efficiently and it is stable enough to be detected.

3.4. Conclusions

In this chapter, the author has studied the geometric and electronic structures of the $Eu_n(COT)_n^-$ anion clusters based on the photoelectron spectra and the DFT method. The geometry optimization for the anions with 4f core ECP and basis set gave two lower-lying states, the ground state X^- as a dominant product and the excited state A^- as a minor product in the experiment, both of which have a one-dimensional structure and strong ionic bonding. The combined experimental and theoretical study made it clear that in the X^- state, the orbital energies of 6s largely decrease with the cluster size and those of the L_δ orbitals on COTs have a stairs-like behavior in the clusters, in which the highest step has an almost constant energy independent of the cluster size. In the A^- state, the 6s level had a negligible cluster size dependence and the L_δ orbitals on COTs showed no stairs-like behavior, in a sharp contrast with that in the X^- state. All this characteristic behavior was interpreted by the position sensitive intracluster electrostatic potential evaluated by the simple point charge models

To investigate the detachment channels from the 4f orbitals, the author suggested to measure the photoelectron spectra of Ba-COT and performed the DFT calculation with the 4f

valence ECP and basis set. The peaks of n=1 and n=2 around 3.7 eV were assigned to the $4f^{-1}$ channel.

With the point charge models, the VDEs for $[Eu(COT)]_\infty^-$ were estimated as 2.894, 2.449, and 0.972 (eV) for the M, C(1) and H peaks, respectively. Such a polymer is interesting as a one-dimensional conductor, since it would have stairs-like orbital energies, and electrical conductivity may arise due to the positively charged soliton generated by electron detachment from the deeper L_δ orbitals. [3.58] In addition, such polymers may show the characteristic energy transfer behavior due to the dipole chains. [3.59-61]

Lastly, the author summarized the energetic relations among the X^-, A^- and X states using the linear synchronous transit paths, and concluded that the A^- state can be observed experimentally because of inefficient relaxation processes to the ground X^- and X states. In the next Chapter 4, the author will present the ionization energies of the X state which also shows size dependence due to the strong ionic bonding and one-dimensional structure. [3.59]

For the V-Bz cluster, Yasuike et al. have previously found a significant cluster size dependence in the valence orbital energies, and their origin was due to the delocalization of the d_δ orbitals of V through the benzene LUMOs. In this study of Eu-COT, the author has also found a similar size dependence, however, it was proved to be due to the very strong intracluster electrostatic potential caused by the strong ionic bonding. All of the results indicate that the unique electronic structure of $Eu_n(COT)_n^-$ is due to the one-dimensional structure. In other words, the characteristic feature observed experimentally is a clear evidence of the one-dimensional strong ionic bonding of the clusters.

Reference

[3.1] T.G. Dietz, M.A. Duncan, D.E. Powers, R.E. Smalley, J. Chem. Phys. 74, (1981) 6511.

[3.2] V.E. Bondybey, J.H. English, J. Chem. Phys. 74, (1981) 6978.

[3.3] V.E. Bondybey, J.H. English, J. Chem. Phys. 76, (1982) 2165

[3.4] M.E. Geusic, M.D. Morse, S.C. O'Brien, R.E. Smalley, Rev. Sci. Instrum. 56, (1985) 2123.

[3.5] A. Nakajima, K. Kaya, J. Phys. Chem. A. 104, (2000) 176.

[3.6] T. Yasuike, A. Nakajima, S. Yabushita, K. Kaya, J. Phys. Chem. A. 101, (1997) 5360.

[3.7] T. Yasuike, S. Yabushita, J. Phys. Chem. A. 103, (1999) 4533.

[3.8] K. Miyajima, K. Muraoka, M. Hashimoto, T. Yasuike, S. Yabushita, A. Nakajima, K. Kaya, J. Phys. Chem. A. 106, (2002) 10777.

[3.9] R. Pandey, B.K. Rao, P. Jena, M.A. Blanco, J. Am. Chem. Soc. 123, (2001) 3799.

[3.10] A.K. Kandalam, B.K. Rao, P. Jena, R. Pandey, J. Chem. Phys 120, (2004) 10414.

[3.11] D. Rayane, A.R. Allouche, R. Antoine, M. Broyer, the author. Compagnon, Ph. Dugourd, Chem. Phys. Lett. 375, (2003) 506.

[3.12] F. Rabilloud, D. Rayane, A.R. Allouche, R. Antoine, M. Aubert-Frécon, M. Broyer, the author. Compagnon, Ph. Dugourd, J. Phys. Chem. A. 107, (2003) 11347.

[3.13] K. Miyajima, A. Nakajima, S. Yabushita, M.B. Knickelbein, K. Kaya, J. Am. Chem.

Soc. 126, (2004) 13202.

[3.14] H. Shumann, A. Juliane, J.A. Meese-Marktscheffel, L. Esser, Chem. Rev. 95, (1995) 865.

[3.15] R.G. Hayes, J.L. Thomas, J. Am. Chem. Soc. 91, (1969) 6876.

[3.16] F. Mares, K. Hodgson, A. Streitwieser, Jr., J. Organomet. Chem. 24, (1970) C68.

[3.17] S.R. Ely, T.E. Hopkins, C.W. Dekock, J. Am. Chem. Soc. 98, (1976) 1624.

[3.18] A. Greco, S. Cesca, W. Bertolini, J. Organomet. Chem. 113, (1976) 321.

[3.19] A.L. Wayda, the author. Mukerji, J.L. Dye, R.D. Rogers, Organometallics. 6, (1987) 1328.

[3.20] K.O. Hodgson, K.N. Raymond, Inorg. Chem. 11, (1972) 3030.

[3.21] K.O. Hodgson, F. Mares, D.F. Starks, A. Streitwieser, Jr., J. Am. Chem. Soc. 95, (1973) 8650.

[3.22] C.W. Dekock, S.R. Ely, T.E. Hopkins, M.A. Brault, Inorg. Chem. 17, (1978) 625.

[3.23] K.N. Raymond, C.W. Eigenbrot, Jr., Acc. Chem. Res. 13, (1980) 276

[3.24] J. Xia, Z. Jin, W. Chen, J. Chem. Soc., Chem. Commun. (1991) 1214.

[3.25] M. Dolg, P. Fulde, W. Küchle, C.-S. Neumann, H. Stoll, J. Chem. Phys. 94, (1991) 3011.

[3.26] M. Dolg, P. Fulde, H. Stoll, H. Preuss, A. Chang, R.M. Pitzer, Chem. Phys. 195, (1995) 71.

[3.27] W. Liu, M. Dolg, P. Fulde, J. Chem. Phys. 107, (1997) 3584.

[3.28] W. Liu, M. Dolg, P. Fulde, Inorg. Chem. 37, (1998) 1067.

[3.29] T. Kurikawa, Y. Negishi, F. Hayakawa, S. Nagao, K. Miyajima, A. Nakajima, K. Kaya, J. Am. Chem. Soc. 120, (1998) 11766.

[3.30] T. Kurikawa, Y. Negishi, F. Hayakawa, S. Nagao, K. Miyajima, A. Nakajima, K. Kaya, Eur. Phys. J. D. 9, (1999) 283.

[3.31] K. Miyajima, T. Kurikawa, M. Hashimoto, A. Nakajima, K. Kaya, Chem. Phys. Lett. 306, (1999) 256.

[3.32] N. Hosoya, R. Takegami, J. Suzumura, K. Yada, K. Koyasu, K. Miyajima, M. Mitsui, M.B. Knickelbein, S. Yabushita, A. Nakajima, J. Phys. Chem. A. 119, (2005) 9, see also Chapter 1 in this thesis.

[3.33] T.A. Halgren, W.N. Lipscomb, Chem. Phs. Lett. 49, (1977) 225.

[3.34] A.D. Becke, J. Chem. Phys. 98, (1993) 5648.

[3.35] Gaussian 98, Revision A.5, M.J. Frisch, G.W. Trucks, H.B. Schlegel, G.E. Scuseria, M.A. Robb, J.R. Cheeseman, V.G. Zakrzewski, J.A. Montgomery Jr., R.E. Stratmann, J.C. Burant, S.Dapprich, J.M. Millam, A.D. Daniels, K.N. Kudin, M.C. Strain, O. Farkas, J. Tomasi, V. Barone, M. Cossi, R. Cammi, B. Mennucci, C. Pomelli, C. Adamo, S. Clifford, J. Ochterski, G. A. Petersson, P.Y. Ayala, Q. Cui, K. Morokuma, D.K. Malick, A.D. Rabuck, K. Raghavachari, J.B. Foresman, J. Cioslowski, J.V. Ortiz, B.B. Stefanov, G. Liu, A. Liashenko, P. Piskorz, the author. Komaromi, R. Gomperts, R.L. Martin, D.J. Fox, T. Keith, M.A. Al-Laham, C.Y. Peng, A. Nanayakkara, C. Gonzalez, M. Challacombe, P.M.W. Gill, B.

Johnson, W. Chen, M.W. Wong, J.L. Andres, C. Gonzalez, M. Head-Gordon, E.S. Replogle, J.A. Pople, Gaussian, Inc., Pittsburgh PA, 1998.

[3.36] J.H. Hammons, D.A. Hrovat, W.T. Borden, J. Am. Chem. Soc. 113 (1991) 4500.

[3.37] P.G. Wenthold, D.A. Hrovat, W. T. Borden, W. C. Lineberger, Science. 272 (1996) 1456.

[3.38] http://www.theochem.uni-stuttgart.de/pseudopotentiale/

[3.39] T.H. Dunning, Jr., P.J. Hay, In Modern Theoretical Chemistry; H.F. Schaefer, III, Ed.; Plenum: New York, 1976; Vol. 3, p 1.

[3.40] W.J. Hehre, R. Ditchfielf; J.A. Pople, J. Chem. Phys. 56, (1972) 2257.

[3.41] P. Flükiger, H.P. Lüthi, S. Portmann, J. Weber, MOLEKEL, version 4.2; Swiss Center for Scientific Computing: Manno, Switzerland, 2000-2002.

[3.42] I. Gotkis, J. Phys. Chem. 95, (1991) 6086.

[3.43] R.W. Field, Ber. Bunsenges. Phys. Chem. 86, (1982) 771.

[3.44] P.M. Boerrigter, E.J. Baerends, J.G. Snijders, Chem. Phys. 122, (1988) 357.

[3.45] N. Rösch, A. Streitwieser, Jr., J. Am. Chem. Soc. 105, (1983) 7237.

[3.46] M. Pepper, B.E. Bursten, Chem. Rev. 91, (1991) 719.

[3.47] N. Hosoya, J. Suzumura, K. Yada, R. Takegami, S. Yabushita, A. Nakajima, J. Phys. Chem. A. submitted.

[3.48] R. Manne, J. Chem. Phys. 46, (1967) 4645.

[3.49] U. Gelius, P.F. Heden, J. Hedman, B.J. Lindberg, R. Manne, R. Nordberg, C. Nordling, K. Siegbahn, Phys. Scr. 2, (1970) 70.

[3.50] H. Basch, Chem. Phys. Lett. 5, (1970) 337.

[3.51] K. Gregson, G.G. Hall, Molec. Phys. 17, (1969) 49.

[3.52] S. Nagase, K. Kobayashi, Chem. Phys. Lett. 228, (1994) 106.

[3.53] P.N. Day, J.H. Jensen, M.S. Gordon, S.P. Webb, W.J. Stevens, M. Krauss, D. Garmer, H. Basch, D. Cohen, J. Chem. Phys. 105, (1996) 1968.

[3.54] P.N. Day, R. Pachter, M.S. Gordon, G.N. Merrill, J. Chem. Phys. 112, (2000) 2063.

[3.55] L. Kronik, R. Fromherz, E. Ko, G. Ganteför, J.R. Chelikowsky, Nature Mat. 1, (2002) 1.

[3.56] R. Takegami, N. Hosoya, J. Suzumura, K. Yada, A. Nakajima, S. Yabushita, Chem. Phys. Lett. 403, (2005) 169, see also Chapter 4 in this thesis.

[3.57] T. Yasuike, S. Yabushita, Chem. Phys. Lett. 316, (2000) 257.

[3.58] T.A. Skotheim, Ed. Handbook of Conducting Polymers; Marcel Dekker: New York, 1986.

[3.59] S.W. de Leeuw, D. Solvaeson, M.A. Ratner, J. Michl, J. Phys. Chem. B. 102, (1998) 3876.

[3.60] E. Sim, M.A. Ratner, S.W. de Leeuw, J. Phys. Chem. B. 103, (1999) 8663.

[3.61] J.J. de Jonge, M.A. Ratner, S.W. de Leeuw, R.O. Simonis, J. Phys. Chem. B. 108, (2004) 2666.

Chapter 4.

Ionization Energies and

Electron Distribution of $Eu_n(C_8H_8)_n$

Abstract

The ionization energies of $Eu_n(COT)_n$ (n=1-4) were found to decrease asymptotically with the cluster size. The low-spin state X and the high-spin state a were characterized with DFT calculations; their adiabatic energy difference was found to decrease with the cluster size. The calculated ionization energies of the X states reproduced the experimental size dependence. Those of the a states also agreed except for n=1. These features were explained by the significant variation of the electrostatic potential at ionization sites. The state-specific permanent dipole moments were calculated to clarify the difference in the electronic states.

4.1. Introduction

Most lanthanide (Ln) compounds have oxidation state of Ln^{3+} and strong ionic bonding characters, which are responsible for their unique properties. [4.1,2] For example, theoretical studies by Dolg et al. showed that $Ln(COT)_2$ (Ln=Ce, Nd, Tb, and Yb, COT=1,3,5,7-cyclooctatetraene) approximately consist of Ln^{3+} central ions pinched with two $COT^{1.5-}$ rings. [4.3] Kurikawa et al. measured the electron binding energies and the adiabatic ionization energies (E_i's) of larger $Ln_n(COT)_m$ (Ln=Ce, Nd, Eu, Ho, and Yb). [4.4] Particularly, they found that the full sandwich clusters $Ln_n(COT)_{n+1}$ ($n \leq 5$) of Ho and Nd show a strong size dependence of E_i's, while those of Eu and Yb were almost independent of the size, and attributed the different behavior to the difference in the preferable oxidation state, namely that the latter two metals prefer Ln^{2+} in the gas phase ionic clusters.

Recently, Nakajima and co-workers have found the preparation of larger size multiple-decker sandwich clusters of $Eu_n(COT)_m$, and considered that the growth process follows the sequential harpoon mechanism. [4.5] Since the one-end open sandwich clusters, $Eu_n(COT)_n$ hereafter abbreviated as (n, n), are key intermediates in this mechanism, accurate determination of their E_i's and the charge distribution is of crucial importance.

In this chapter, the author discusses the experimental E_i's of (n, n) which show the characteristic decrease with the cluster size and provides a theoretical analysis of its origin with a focus on the charge distribution. Their permanent dipole moments are also discussed in connection with the critical dependence on the geometric structures and charge distributions of these clusters.

4.2. Computational Method

All the DFT calculations were carried out with the B3LYP functionals [4.6] built in the Gaussian 98 program, [4.7] employing two basis sets. In Basis-A, the 4f core ECP and (7s6p5d)/[5s4p3d] basis set of the Stuttgart/Cologne group [4.8] were chosen for Eu and D95 [4.9] for COT. In Basis-B, D95 was replaced by 6-31+G(d) [4.10].

4.3. Results and Discussions

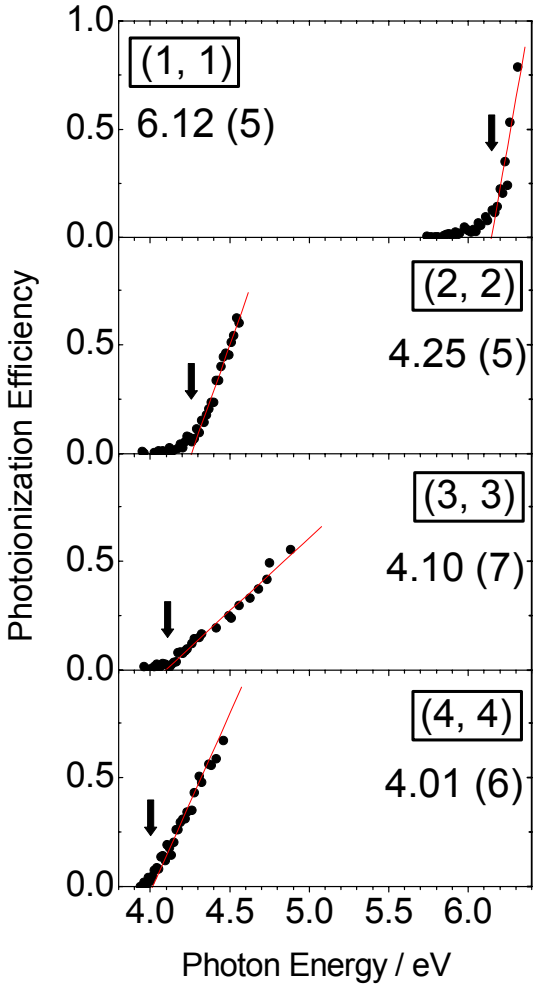

Fig. 4-1 Photoionization efficiency curves for $Eu_n(COT)_n$ (n=1-4). Solid downward arrows show the adiabatic ionization thresholds. Number in parentheses indicate experimental uncertainties; 6.12(5) represents 6.12±0.05.

Fig. 4-1 shows the PIE curves for (*n*, *n*) (*n*=1-4). The experimental E_i's exhibit a characteristic asymptotic decrease with *n*.

4.3.1. Geometric and electronic structures

It is convenient to define a molecular axis (*z*-axis) as a line passing through Eu and the center of gravity of COT. The eight π orbitals on a COT are classified with the symmetry as nondegenerate L_σ, doubly degenerate L_π, L_δ, L_ϕ, and nondegenerate L_γ. The neutral COT has the valence electronic configuration of $L_\sigma^2L_\pi^4L_\delta^2$ with two holes, while the ground state of Eu is $4f^76s^2$ with two weakly bound electrons, therefore the bonding scheme of Eu(COT) is essentially an ionic bond between Eu^{2+} and COT^{2-} with a large permanent dipole moment. This strong polarity of the monomer unit would favor the linear chain structures of the (*n*, *n*) clusters and give rise to a strong electric field in the cluster, as shown in Fig. 4-2.

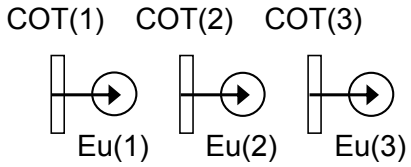

Fig. 4-2 Linear dipole chain structure of $Eu_n(COT)_n$. The white circles and plates denote +2 charged metals and dotted and -2 charged COT ligands, respectively. The arrow denotes a dipole moment composed of COT^{2-} and Eu^{2+}

In this figure, an arrow represents a dipole moment composed of COT^{2-} and Eu^{2+}, and COT(*i*) denote the *i* th COT counted sequentially from the left, and also Eu(*i*) the *i* th Eu from the left. This electric field has a strong influence on the frontier orbitals, among which L_δ on the COT(1) is destabilized most and becomes HOMO, whereas the empty 6s orbital on the opposite terminal Eu is stabilized most and becomes LUMO. As *n* becomes larger, this electric field gets stronger and electric field may eventually exchange these two energy levels and prompt an electron transfer from L_δ on COT(1) to 6s on the opposite side, yielding stable

diradical states with these two open-shell orbitals.

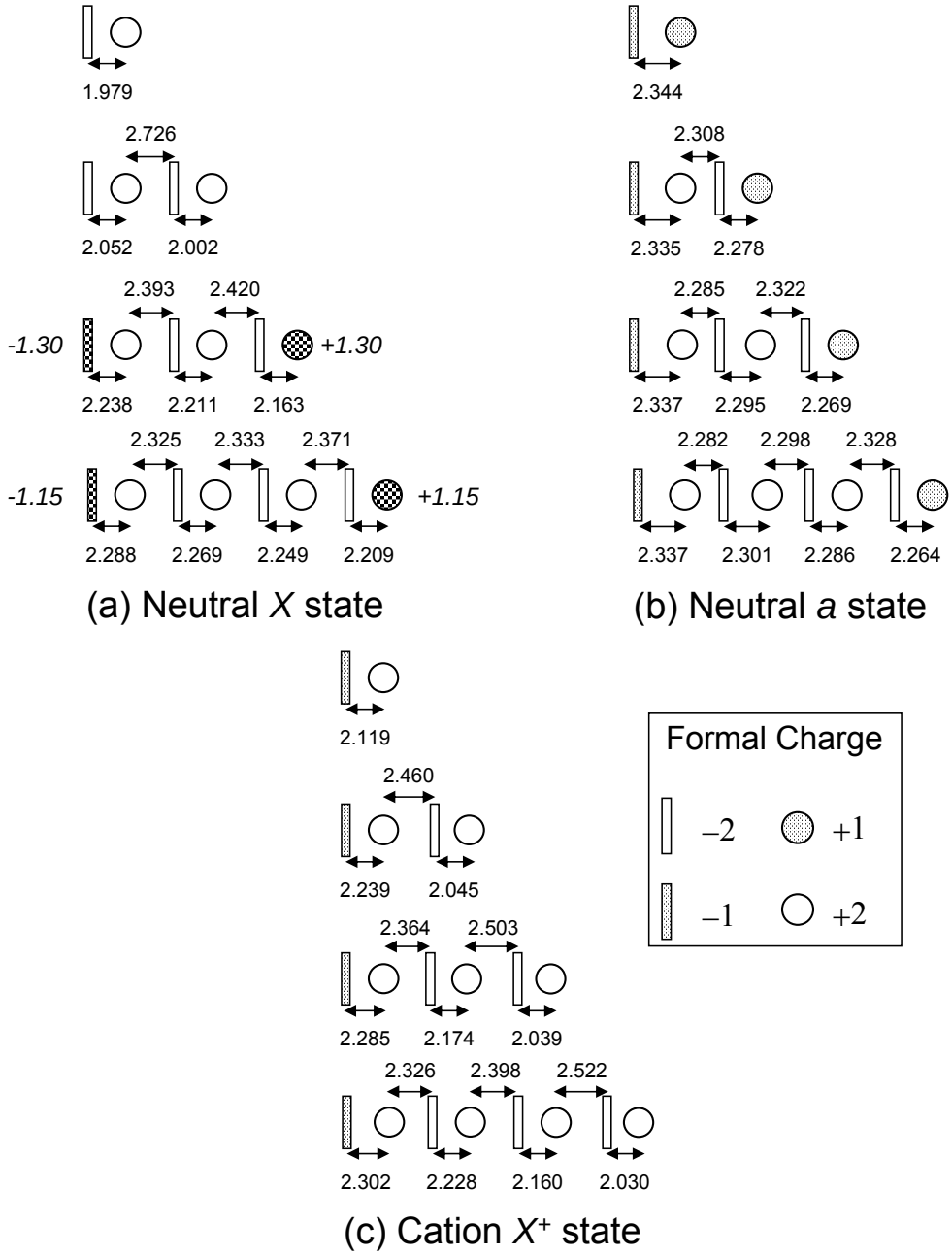

Fig. 4-3 Optimized distances between Eu and the center of gravity of the COT carbon ring along with the formal charge distribution for the neutral and cation clusters calculated with Basis-B for *n*=1-3 and Basis-A for *n*=4. The dotted and white circles denote +1 and +2 charged metals, and dotted and white plates denote -1 and -2 charged COT ligands, respectively. The checked circles and plates reflect the characteristic delocalized molecular orbitals as shown in Fig.4-5, and the charges were determined as +1.30 and -1.30 for *n*=3, and +1.15 and -1.15 for *n*=4, respectively.

The optimized geometries along with the formal charges are shown in Fig. 4-3 (a), (b), and (c) geometry, for the singlet X, triplet a for the neutral, and doublet X^+ state for the cation,

respectively. Note that with the 4f-core ECP, 4f electrons are not explicitly treated and their spins are suppressed. The formal charges are determined from the number of electrons in the 6s and L_δ orbitals, which are well localized except in the cases of n=3 and 4 of the X state.

For n=1-4, the a state is a simple HOMO-LUMO excited triplet diradical state obtained from the closed-shell singlet state, and therefore the 6s orbital on the terminal Eu becomes the HOMO of the a state. The closed-shell singlet state is the ground state X only for n=1 and 2, and the HOMO is L_δ on COT(1). For n=3 and 4, as described above, the electric field is so strong that the closed-shell singlet state becomes unstable and spin- and space-symmetry breakings take place, and the ground electronic state X gains a singlet diradical character.

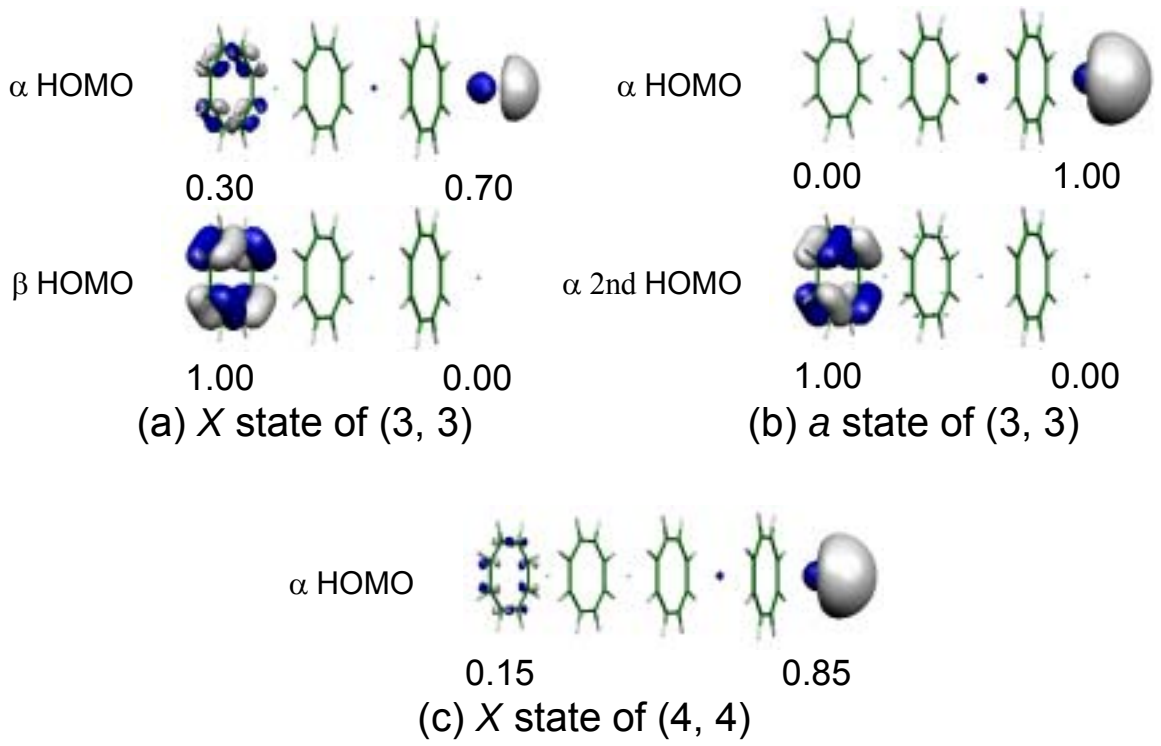

Fig. 4-4 Kohn-Sham orbitals of the *X* and *a* states of n=3 and that of the *X* state of n=4 plotted with the Molekel program [12], and the Mulliken population for the terminal Eu and COT. All the results were calculated by Basis-B.

Fig. 4-4 (a) shows the α and β spin HOMOs of the X state of n=3 are localized in 6s on Eu(3) and L_δ on COT(1), respectively, yet to a lesser extent than the corresponding open-shell orbitals for the a state in Fig. 4-4 (b). In the X state of n=4, the degree of the orbital

localization increases as seen in Fig. 4-4 (c) and also in the increase of the S^2 value, from 0.675 for n=3 to 0.825 for n=4. In addition, the α spin orbitals of n=3 and 4 in the X state show unusual mixings, because of the space-symmetry breaking, between 6s and L_δ of each terminal Eu and COT, respectively. The Mulliken population analysis for these orbitals provides an estimate of the degree of the localization in the terminal Eu and COT as given in Fig. 4-4 and the formal charge distribution for these states in Fig. 4-3.

Table 4-1. Optimized geometry parameters of the C-C bond length of each COT in the X, a and X^+ state.[a,b,c]

			X state		
		COT(1)	COT(2)	COT(3)	COT(4)
(*n*, *n*)	Basis	C-C	C-C	C-C	C-C
(1, 1)	B	1.421	———	———	———
(2, 2)	B	1.421	1.423	———	———
(3, 3)	B	1.396 (1.438)	1.421 (1.423)	1.422 (1.422)	———
(4, 4)	A	1.402 (1.452)	1.431 (1.433)	1.432 (1.433)	1.432 (1.433)
			a state		
		COT(1)	COT(2)	COT(3)	COT(4)
(*n*, *n*)	Basis	C-C	C-C	C-C	C-C
(1, 1)	B	1.385 (1.446)	———	———	———
(2, 2)	B	1.386 (1.447)	1.421 (1.423)	———	———
(3, 3)	B	1.386 (1.447)	1.421 (1.423)	1.422 (1.422)	———
(4, 4)	A	1.396 (1.457)	1.432 (1.434)	1.432 (1.433)	1.432 (1.432)
			X^+ state		
		COT(1)	COT(2)	COT(3)	COT(4)
(*n*, *n*)	Basis	C-C	C-C	C-C	C-C
(1, 1)	B	1.389 (1.449)	———	———	———
(2, 2)	B	1.387 (1.448)	1.424 (1.424)	———	———
(3, 3)	B	1.386 (1.448)	1.422 (1.424)	1.424 (1.424)	———
(4, 4)	A	1.397 (1.457)	1.432 (1.434)	1.433 (1.433)	1.434 (1.435)

[a] For n=1-3, the optimized parameters are calculated by Basis-B, and for n=4, they are calculated by Basis-A.
[b] COT(i) denotes i th COT counted sequentially from the left in Fig. 4-4.
[c] Because of the C_{4v} structure, two kinds of C-C bond lengths are distinctively shown, longer being in parenthesis.

Table 4-1 summarized the optimized C-C bond distances of the COT ligands in the X, a and X^+ states to focus on the geometry of each COT. The symmetry of the X state was C_{8v} for n=1 and 2, consistent with the aromaticity with the formal charge of −2 for all of COTs with the

optimized C-C bond lengths of about 1.42 Å. For the remaining cases, only the COT(1) has the open-shell configuration of $L_\sigma^2 L_\pi^4 L_\delta^3$, which causes a Jahn-Teller distortion to overall C_{4v} symmetry. Their two kinds of C-C distances were about 1.39 and 1.45 Å, however, the remaining COTs had essentially C_{8v} structure. [4.12,13]

Additionally, the frequency analysis was performed for the *n*=1-3 cluster size with Basis-A and the results were summarized in Table 4-2. For the X and a states of *n*=1 and 2 and the X^+ state of *n*=1, the above C_{8v} and C_{4v} structures were local minima. For other states, a non-degenerate imaginary frequency was obtained along a twist motion of COT (TW) and a doubly degenerate imaginary frequency along a lateral motion from the *z*-axis (LAT). However, all the imaginary frequencies are very small. Thus, the geometries were assumed to be restricted to the C_{4v} structures for the latter states.

Table 4-2. Calculation results of the frequency analysis for the X, a and X^+ state with the 4f CORE-A.[a] NONE, TW and LAT represent 'no imaginary frequency' and imaginary frequencies along the twist motion of COT and along the lateral motion from the z-axis, respectively.

(*n*, *n*)	X state	a state	X^+ state
(1, 1)	NONE	NONE	NONE
(2, 2)	NONE	7.73 (TW)	8.82 (TW)
(3, 3)	7.14 (TW) 5.52 (LAT)	7.61 (TW) 5.77 (LAT)	13.53 (TW)

[a]The optimized geometries of 4f CORE-A were used for analysis. The differences of the optimized geometries between 4f CORE-A and -B were 0.02Å or less.

4.3.2. Ionization energies and permanent dipole moments of the X and a states

Fig. 4-5 shows that the ΔDFT methods for the X state reproduce the asymptotic behavior of E_i's quantitatively. The agreement of the results for the a state is also satisfactory except for

n=1. This is accountable because their adiabatic energies become almost degenerate, as n increases, as discussed below, and they have a common final state X^+. These low E_i values are prerequisite for the sequential growth mechanism based on harpooning. In addition, the strong diradical character shown above for the X and a states, with radical centers localized on both ends, is quite reasonable for this mechanism. [4.5]

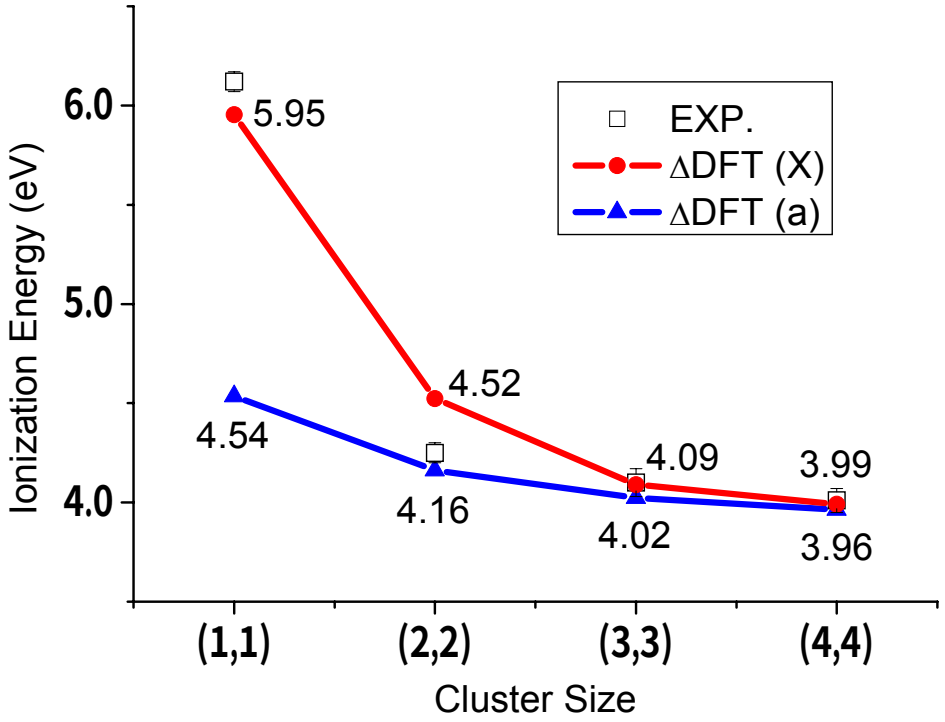

Fig. 4-5 Experimental ionization energies in comparison with calculation results of the *X* and *a* states by DDFT method. The Basis-B was applied with the optimized geometries of Fig. 4-3.

The origin of the size dependence of these E_i's is the significant variation in the electrostatic potential at the ionization sites, as also discussed in Chapter 3. [4.13]

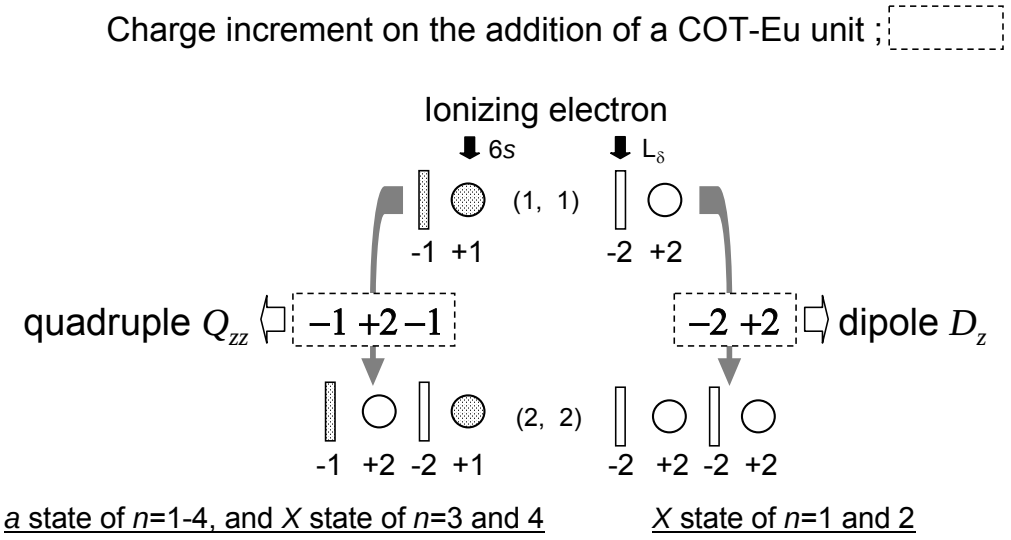

(a) One-end open sandwich : quadruple Q_{zz} or dipole D_z

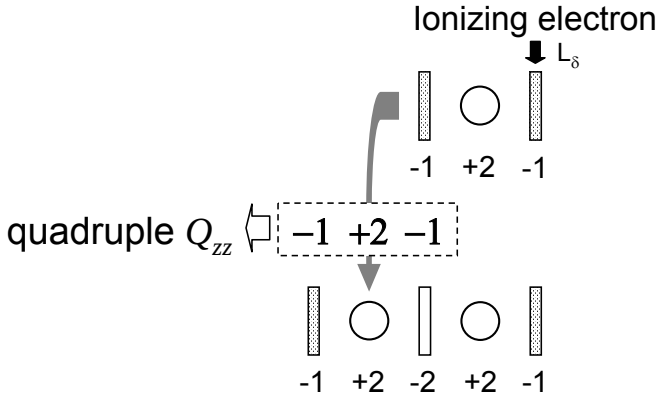

(b) Full sandwich : quadruple Q_{zz}

Fig. 4-6 Schematic explanation for the variation of E_is : (a) one-end open sandwich and (b) full sandwich. Seeing from the ionizing electron, the size increase of the one-end open sandwich corresponds to the attachment of a quadruple or dipole moment, while that of the full sandwich is represented by the attachment of a quadruple moment

Let us first consider the small size dependence of E_i of the a state using the formal charge distribution of Fig. 4-6(a). In view of the right end Eu, where the HOMO of 6s resides, the increase in n can be regarded as the attachment of a group of −1, +2, −1 point charges, an approximate quadruple moment, to the left side of the cluster, which weakly destabilizes the ionizing electron and results in an asymptotic decrease.

Next, let us consider the large decrease in E_i from n=1 to n=2 in the X state, whose HOMO is L_δ on COT(1). Viewing from this orbital, the increase in the size corresponds to the attachment of a pair of −2 and +2 point charges, namely a dipole moment, to the right end of the cluster, which significantly destabilizes the ionizing electron in COT(1).

As for the small size dependence of E_i from n=3 to n=4, the electronic structure of the X state is the singlet diradical state, so that their E_i shows an asymptotic decrease as in the case of the a state.

A similar explanation can also be made on the size independent E_i of the full sandwich $Eu_n(COT)_{n+1}$. [4,14] A preliminary calculation results show that the lowest ionization occurs from the terminal COT with a formal charge of −1. The increase in n corresponds to the attachment of a quadruple moment to the opposite terminal side as shown in Fig. 4-6 (b); therefore the E_i shows no significant size dependence. These size dependencies can provide clear evidence for Eu to take the oxidation state of Ln^{2+} in these clusters.

Table 4-3. Adiabatic excitation energy (ADE) ofbetween the X and a state with respect to the X state and and z component of their dipole moment calculated by Basis-A and -B. The inside of parenthesis is the results of Basis-A.

(n, n)	ADE (eV)	Dipole moment (D)	
		X	A
(1, 1)	1.419 (1.415)	8.482 (8.436)	0.259 (0.655)
(2, 2)	0.362 (0.331)	21.825 (21.692)	0.167 (-0.146)
(3, 3)	0.066 (0.062)	11.321 / 18.938[a] (9.936 / 17.324[a])	0.095 (-0.269)
(4, 4)	0.031 (0.027)	9.246 / 17.477[a] (8.029 / 15.536[a])	-0.124 (-0.292)

[a] Calculation results with the a state spin contamination projected out.

Table 4-3 shows that the energy difference between the X and a states decreases asymptotically with n owing to the diradical character. Therefore, both states may coexist as intermediates and their distinction by the E_i's alone seems to be difficult. To see these states

from another standpoint, their dipole moments were compared in Table 4-3. The theoretical results predict that the dipole moments of the X and a states are very large and small, respectively, reflecting the difference in their charge distribution and the optimized geometries. For example, as seen from Fig. 4-3 the charge distribution of the X state for n=2 represents two parallel dipoles ($COT(1)^{2-}$ $Eu(1)^{2+}$) and ($COT(2)^{2-}$ $Eu(2)^{2+}$), whereas that of the a state consists of two anti-parallel dipoles ($COT(1)^{-}$ $Eu(2)^{+}$) and ($Eu(1)^{2+}COT(2)^{2-}$). For n=3 and 4, their dipole moments are still significantly different. The primary reason for this difference is that they have differently delocalized HOMOs, as shown in Fig. 4-4, which have a large influence due to the one-dimensional structure. The difference in the geometries of the X and a states, namely large and small bond alternation displayed in Figs. 4-3 (a) and (b) respectively, is also attributable to this difference. The author hopes that experimental measurement of the permanent dipole moments can clarify the electronic states of the prepared clusters.

Reference

[4.1] R.W. Field, Ber. Bunsenges. Phys. Chem. 86, (1982) 771.

[4.2] I. Gotkis, J. Phys. Chem. 95, (1991) 6086.

[4.3] W. Liu, M. Dolg, P. Fulde, J. Chem. Phys. 107, (1997) 3584.

[4.4] T. Kurikawa, Y. Negishi, F. Hayakawa, S. Nagao, K. Miyajima, A. Nakajima, K. Kaya, J. Am. Chem. Soc. 120, (1998) 11766.

[4.5] N. Hosoya, R. Takegami, J. Suzumura, K. Yada, K. Koyasu, K. Miyajima, M. Mitsui, M. B. Knickelbein, S. Yabushita, A. Nakajima, J. Phys. Chem. A. 119 (2005) 9, see also Chapter 1 in this thesis.

[4.6] A.D. Becke, J. Chem. Phys. 98, (1993) 5648.

[4.7] M.J. Frisch et al., Gaussian 98, Revision A. 5, Gaussian Inc., Pittsburgh, PA, 1998.

[4.8] http://www.theochem.uni-stuttgart.de/pseudopotentiale/

[4.9] T.H. Dunning, Jr., P.J. Hay, in Modern Theoretical Chemistry, Ed. H.F. Schaefer, III (Plenum, New York, 1976), Vol. 3, 1.

[4.10] W.J. Hehre, R. Ditchfielf, J.A. Pople, J. Chem. Phys. 56, (1972) 2257.

[4.11] MOLEKEL 4.2, P. Flükiger, H.P. Lühti, S. Portmann, J. Weber, Swiss Center for Scientific Computing, Manno (Switzerland), 2000-2002.

[4.12] P.G. Wenthold, W.C. Lineberger, Acc. Chem. Res. 32, (1999) 597.

[4.13] R. Takegami, N. Hosoya, J. Suzumura, A. Nakajima, S. Yabushita, J. Phys. Chem. A.

in press, see also Chapter 3 in this thesis.

Chapter 5.

General Conclusion

In this thesis, the author has discussed theoretical analysis and modeling on the molecular spectroscopy of oxygen molecule and one-dimensional lanthanide-cyclooctatetraene clusters.

As for oxygen molecule, the electric-dipole forbidden transition $A^3\Sigma_u^+ \leftarrow X^3\Sigma_g^-$ in the Herzberg I band system was treated. To evaluate the electric transition moment, three theoretical intensity borrowing models, SOCI, Pert(Full) and Pert(England), were employed in which the spin-orbit coupling (SO) and L-uncoupling (RO) are considered as perturbations.

In the SOCI model, the author firstly calculated SO interaction variationally, which plays the primary contribution to the electric transition moment, and secondly treated RO interaction using the first-order perturbation theory with the SO wave functions (Hund's case (c) basis function) as the zero-th order basis functions. As for the Pert(Full) and Pert(England), both SO and RO interactions were evaluated using the first-order perturbation theory with the spin-free wave functions (Hund's case (a) basis function) as the zero-th order basis. The difference between Pert(England) and Pert(Full) model is that the former model includes only one dominant perturbing state as $1^3\Pi_g$ and $B^3\Sigma_u^-$ among all complete basis functions.

In comparison of each calculated electric transition moment, it was found that the SOCI and Pert(Full) model give almost same electric transition moment, on the other hand, the

Pert(England) model presents largely different values from the above electric transition moments. Namely, the contribution of excited states other than $1^3\Pi_g$ and $B^3\Sigma_u^-$ cannot be neglected.

To confirm an accuracy of each transition moments, the integrated rotational line strength and vibrational oscillator strength with the three models were calculated, and compared with the experiment. It is found that SOCI and Pert(Full) are able to calculate them quantitatively, on the other hand, Pert(England) cannot yield them even qualitatively, because Pert(England) cannot represent the complicated configuration interactions with highly excited states induced by the perturbations. Therefore, it was conclude that the interactions with highly excited states, which have been believed as small in the past because of the large energy separation, cannot be neglected at all in the case of very weak absorption band system.

From the detailed analysis for the Herzberg I band system as mentioned before, the author has made clear some characteristics of theoretical methods to treat an electric-dipole forbidden transition. These characteristics can also be generalized to other molecules, because initial and final states of various forbidden transitions have open-shell electric structures which result in complicated configuration interactions through small perturbations as mentioned above. In the case of light molecules, weak perturbations can be taken into account using models like SOCI or Pert(Full). On the other hand, in the case of heavy molecules in which the SO interaction becomes much stronger, a variational or higher-order perturbation theory should be applied, because non-negligible differences between the SOCI and Pert(Full) models were observed even in the oxygen molecule and such a difference becomes more significant as increasing the SO interaction. For the future studies, we should investigate other electric-forbidden bands keeping the above characteristics in mind.

As for the one-dimensional lanthanide-cyclooctatetraene clusters (Ln-COT), the author

focused on the $Eu_n(COT)_n$ sandwich clusters. The geometric and electronic structures of the anions and neutral clusters show that they have the fairly ionic bonding which consists chiefly of Eu^{2+} and COT^{2-} components, and their valence orbital energies depend strongly on the electronic state, the cluster size, and their positions in the clusters.

As for the anion clusters in the ground state, the orbital energies of 6s largely decrease with the cluster size and those of the L_δ orbitals on COTs have a stairs-like behavior in the clusters, in which the highest step has an almost constant energy with the cluster size. For the first excited state, the 6s level had a negligible cluster size dependence and the L_δ orbitals on COTs showed no stairs-like behavior.

As for the neutral clusters in the triplet ground state, the 6s orbital energies (HOMO) of the terminal Eu are independent of the cluster size. For the singlet ground state of n=1 and 2, the HOMO is the L_δ orbitals of the terminal COT, whose energies increase significantly. For that of n=3 and 4, the HOMO changes to the 6s orbitals of the terminal Eu and their energies are almost constant with the cluster size. Although these two spin states show different electronic structures, their adiabatic excitation energies decrease asymptotically with the cluster size.

Comparing with the experimental photoelectron spectra, the author had obtained good agreement and confirmed the above characteristics.

To investigate the characteristic orbital energies of each valence orbital, the author has developed the simple point charge models, and revealed that the reason of all characteristic behaviors is due to the anisotropic intracluster electrostatic field by the one-dimensional structure and the strong ionic bonding.

Although the point charge model easily estimated the cluster size dependency of the orbital energies, there are two important reminders for the application of the point charge model to other molecules: (i) This model is only applicable to molecules with localized orbitals, for

example, due to strong ionic bondings. (ii) Their calculation results are strongly affected by the magnitude and place of point charges. Therefore, before the application of this model to other molecules, we should investigate their geometric and electronic structures carefully by theoretical and experimental method.

Finally, the author describes the issues which remain unsettled. In this thesis, the properties of the 'full' ($Eu_n(COT)_{n+1}$) and 'inverse' ($Eu_{n+1}(COT)_n$) sandwich clusters are not discussed in detail. However, Nakajima and co-workers measured very interesting photoelectron spectra, and ionization energies of these clusters. For the ionization energies, author's preliminary calculation results showed the good agreement with the experiment, however, for the photoelectron spectra of their anions, the agreement becomes worse.

In doing so, we should firstly study their geometric structures in detail. For the 'full' and 'inverse' anion clusters, two types of geometries, symmetric structure (D_{8h} or D_{4h}) and anti-symmetric structure (C_{8v} or C_{4v}) can be considered. Preliminary calculations showed that DFT method gave symmetric structures, on the contrary, CASSCF method presented anti-symmetric structures for both 'full' and 'inverse' anion clusters. In the future studies, large size CASSCF or CI calculation should be performed to solve these discrepancies, because in these two clusters both dynamical and nondynamical electron correlations would be very important.

Secondly, we should investigate the geometric and electronic properties of other Ln-COT clusters, especially, Ln=Nd, Tb, Ho which take a +3 oxidation state in the cluster by using the photoelectron spectroscopy and theoretical calculation. The Ln(III)-COT sandwich clusters will show very different electronic properties from the Ln(II)-COT in spite of the similar geometric structures as discussed in the earlier works by Kurikawa et al.

The most difficult problem for calculating the Ln(III)-COT clusters is that they have open

shell 4f electrons. Therefore, if possible, we would like to perform large size active space CASSCF+CI calculations for the larger size clusters as in the earlier calculations by Dolg and co-workers.

Because of the very different mass spectra between Ln(II) and Ln(III)-COT clusters, the author thinks that the growth mechanism of Ln(III)-COT clusters is different form that of Ln(II)-COT. For the Ln(II)-COT, each harpooning reaction rate as discussed in this thesis would be almost the same, because their mass spectra show almost the same compositions of (n-1, n), (n, n), (n, n+1). However, for Ln(III)-COT, their mass spectra indicate only one strong compositions of (n, n+1). One possibility for the difference is that each reaction rate is very different in the sequential harpoon mechanism of Ln(III)-COT. Another reaction mechanism may dominate the growth process of Ln(III)-COT.

The author hopes that this thesis helps further research on the Ln-COT clusters to clarify the above problems in the future.